Heat Transfer and Film Thickness Characteristics of Spray Cooling with Phase Change

by

Adam G. Pautsch

A thesis submitted in partial fulfillment of
the requirements for the degree of

MASTERS OF SCIENCE
(Mechanical Engineering)

UNIVERSITY OF WISCONSIN-MADISON
2004

Heat Transfer and Film Thickness Characteristics of Spray Cooling with Phase Change

Adam G. Pautsch, M.S.
Department of Mechanical Engineering
University of Wisconsin-Madison, 2004
Professor Timothy A. Shedd, Advisor

Two test facilities were used to study the characteristics and method of spray cooling. Spray cooling is a process that delivers liquid droplets from an atomizer to a surface that is hotter than the saturation temperature of the fluid. The droplets impact the surface and spread, causing a thin liquid film to form. This liquid film is capable of removing large heat loads from the surface. Ten nozzle designs were tested, including arrays of between 1 and 16 nozzles. Each nozzle design was tested at a minimum of 4 flow rates. The emphasis of this study is to investigate the behavior of the film on the die surface to determine ways to improve on spray cooling designs for future designs.

The first test facility used to investigate the limits and abilities of the nozzles was a heat transfer stand. Measurements of the applied heat load of each die and the junction temperatures at 8 locations per die were taken. Measurements were also recorded for the conditions of the fluid being delivered to the die. From these, values of critical heat fluxes, heat transfer coefficients, and surface temperature distributions were obtained. The measured critical heat fluxes of the nozzle designs that were tested ranged from 8.5 to 75.7 W/cm^2. Local heat transfer coefficients ranged from 0.1 to 1.4 $W/cm^2 - K$.

Another heat transfer related property that was investigated was the efficiency of the design. The efficiency was defined as the critical heat flux divided by the sum of the available latent and sensible heat capacities of the fluid. Experimental results showed that nozzle designs with lower efficiencies could reach higher levels of critical heat flux and had more desirable heat transfer coefficients. Efficiencies at critical heat flux were calculated to be between 0.17 and 0.35. Lower values of efficiency mean that the system is less reliant on the two-phase component of heat transfer. Designs that are capable of removing heat with-out surface nucleate boiling were found to perform better.

A visualization test stand was also designed and constructed for the visualization portion of the study. A 2000 Å thick coating of indium tin oxide (ITO) on a glass die created a transparent, resistive heating element. Measurements of the film thickness under adiabatic conditions were taken using an optical technique based on the angle of total internal reflection. Experimental film thicknesses were measured to be 42 - 918 μm. A numerical model was developed to predict the film thicknesses; values predicted were 79 - 280 μm. The results of these two tests were correlated to understand how the spray distribution and patternization effects the heat transfer characteristics.

Acknowledgments

I would first like to thank my two advisors, Tim Shedd and Greg Nellis, for the support that they have shown through-out this project. We have had many long meetings and discussions, but they have always been willing to take the time to help me to understand this project. Tim especially has spent many hours in the lab and in the office both researching and motivating the project. Greg has been a monumental help in the modeling work done.

I would also like to thank my family for their support through my college career: My parents, Greg and Pam, and my sisters, Brea and Jamie. Also, my girlfriend Becky for putting up with me working late on many occasions and always listening to my problems with the project, even though she had no idea what I was talking about. She has always been enthusiastic and supportive of my work. All of them have helped me to get where I am today.

During this project, two undergraduate students have helped me by working on this project. Natalie Meagher ran many of the heat transfer experiments and helped to develop and manufacture parts for the flow visualization stand. Nicole Weimer also helped construct the flow visualization stand and the film thickness measurement technique.

Part of this project was funded through a fellowship from Robert Bolz. I would like to thank him for his financial support. I would also like to thank several corporations that made donations of test equipment used for the project. These companies include Cray Inc, Parker Hannifin Corp, and 3M.

Finally, I would like to thank all of my friends and colleges in the Solar Energy Lab, especially those in 1335 ERB: Daniel, Patty, Thomas, Diego, Frank, Charlie, and soon to be Holly. We've had many entertaining conversations, but also some intelligent ones. That was a big part of what kept me excited about working though.

Table of Contents

List of Tables

List of Figures

Nomenclature

Symbol		Description	Units
A	=	area of test die	$[cm^2]$
c_p	=	specific heat of liquid	$[J/kg-K]$
C_g	=	dissolved gas concentration	$[mol/mol]$
d	=	droplet diameter	$[\mu m]$
CHF	=	critical heat flux	$[W/cm^2]$
δ	=	film thickness	$[\mu m]$
ΔP_{cap}	=	Pressure differential across the spray cap	$[psid]$
Δp_d	=	dynamic pressure	$[Pa]$
ΔT	=	$T_i - T_{in}$	$[K]$
ΔT_{die}	=	$T_{max} - T_{min}$	$[K]$
ΔT_{sat}	=	$T_{sat} - T_{in}$	$[K]$
ε	=	cooling effectiveness	$[J/ml]$
η	=	efficiency	
$\eta_{1\phi}$	=	η at which subcooling is overtaken	
η_{max}	=	η at critical heat flux	
Fr	=	Froude number	
g	=	gravitational constant	$[m/s^2]$
H	=	Henry's constant	$[mol/mol-kPa]$
h_i	=	local heat transfer coefficient	$[W/cm^2-K]$
K_1	=	momentum conversion factor	
h_{fg}	=	heat of vaporization	$[J/kg]$
k_f	=	thermal conductivity of fluid	$[W/m-K]$
HTC	=	heat transfer coefficient	$[W/cm^2-K]$
$\dot{m}$	=	mass flow rate of fluid	$[kg/s]$
$\dot{m}''$	=	mass flow flux of fluid	$[kg/m^2-s]$
μ	=	liquid dynamic viscosity	$[kg/m-s]$
n	=	index of refraction	
P_{cap}	=	pressure of the cap	$[psia]$
P_g	=	partial pressure of the gas	$[psia]$
P_{res}	=	pressure of the reservoir	$[psia]$
P_{sat}	=	saturation pressure	$[psia]$

P_{tot}	=	total pressure	$[psia]$
ϕ	=	slope angle of the liquid-vapor interface	$[deg]$
q	=	power	$[W]$
q''	=	heat flux	$[W/cm^2]$
q''_{max}	=	maximum sustained heat flux (CHF)	$[W/cm^2]$
Q	=	volumetric flow rate of fluid	$[L/min]$
Q''	=	volumetric flow flux of nozzle	$[mL/cm^2 - s]$
r	=	light ring radius	$[\mu m]$
R	=	reflectivity	
$R_{\|\|}$	=	reflectivity of parallel polarization of light	
$R_{\perp}$	=	reflectivity of perpendicular polarization of light	
rad	=	radial distance	$[pixels]$
ρ_f	=	density of liquid	$[kg/m^3]$
Re	=	Reynolds number	
σ	=	surface tension	$[N/m]$
t	=	thickness	$[\mu m]$
θ_c	=	critical angle	$[deg]$
θ_i	=	angle of incidence	$[deg]$
θ_r	=	angle of reflection	$[deg]$
θ_t	=	angle of transition	$[deg]$
τ	=	wall shear	$[Pa]$
T_{ave}	=	average temperature of test die	$[K]$
T_i	=	local surface temperature	$[K]$
T_{in}	=	fluid inlet temperature	$[K]$
T_{max}	=	maximum temperature of test die	$[K]$
T_{min}	=	minimum temperature of test die	$[K]$
T_{out}	=	fluid outlet temperature	$[K]$
T_{res}	=	temperature of the reservoir	$[K]$
T_{sat}	=	saturation temperature	$[K]$
u	=	x-velocity component of the film	$[m/s]$
v	=	y-velocity component of the film	$[m/s]$
$v_{d,z}$	=	z-velocity component of the droplet	$[m/s]$
We	=	Weber number	

Chapter 1

Introduction

In an article written for *Electronics* in April of 1965, an engineer named Dr. Gordon Moore made the observation that the number of components per unit area of electronic devices was growing nearly exponentially and predicted that this trend would continue [1]. This prediction has come to be known as Moore's Law, and although his original predictions are not accurate today, the growth trend amazingly still holds true almost 40 years later due to numerous advances in the electronics industry. A primary consequence of Moore's Law that even Moore himself did not anticipate is that the heat flux that must be removed grows proportionally to the component density. For example, in the integrated circuit, where manufacturing technology has allowed for a continual increase in the density and operating frequency of MOSFET devices, the power dissipation levels have increased substantially. Also, demand for higher efficiency AC motors and powerful DC stepper motors has led to the development of large, densely packaged power electronic modules that are approaching their thermal limits. Tremendous advances in solid-state optics have allowed for the development of small yet powerful lasers that reject large amounts of heat from a small area, creating a similar high heat flux thermal management problem.

The most common solution for removing higher heat loads in the past has been to attach a larger heat sink to the die and cool it by blowing air across it with a fan. This design has been acceptable for many years, but it is rapidly approaching its practical limits of heat flux removal. Reliability issues require that electronic devices remain below a certain temperature threshold [2,3]; with the power levels of many next-generation electronics, the amount of air

required will make it impossible for fans to maintain the dies' temperature at an acceptable level. Also, extended surfaces do not allow for dies to be mounted close to each other. If dies can be mounted near one another, less time is required for signals to travel between the two, there-by increasing the system's speed. New methods of cooling must be developed that are capable of handling these heat loads and allow for devices to be mounted near one another in order to prevent a stand-still in electronics development.

The ideal thermal management system should provide high heat removal rates uniformly over a large area. Spray cooling is a very promising candidate to address the thermal concerns of systems requiring high heat flux removal in a compact volume. This is demonstrated by its successful commercial application in the Cray X1 vector supercomputers [4] and the numerous patents that have been granted for various spray cooling applications [5–13]. Application to future generations of high heat flux devices, however, will require more uniform surface coverage and higher peak heat fluxes. The critical heat flux (CHF) of spray cooling with the use of fluorocarbon liquids is 60 to 150 W/cm^2 at this time; this value depends on test conditions [14]. The CHF sets the limits of the peak performance of spray cooling. In order to raise this limit, a better understanding of the physics associated with the spray cooling process must be gained. Possibly the most important and least studied parameter of spray cooling is the thickness of the liquid film layer that forms on the heated surface.

It is generally agreed that spray cooling involves the deposition of a large number of liquid droplets onto a surface with a temperature that is greater than the saturation temperature of the fluid carried by the droplets. As the droplets contact the heated surface they spread out over the surface which becomes fully wetted by a thin liquid film [15]. Heat is added to this film as it is pushed along the surface by the momentum added by incoming droplets. These new droplets arrive at a temperature that is lower than the film near the surface, even if the droplets are not subcooled. The droplets that impact the surface of the film become part of the film and their kinetic energy is converted into a velocity. The impacts

also serve to mix the thin film and possibly entrain vapor bubbles. These bubbles enhance the mixing of the film, which is now two-phase. At the interface between the die and the film, nucleate bubbles will form. The turbulence of the film will not allow these bubbles to attach or remain on the surface; they will separate before they are fully grown as defined by the balance of forces. After bubbles separate from the surface they are carried away by the film and enhance the mixing.

Spray cooling has often been misrepresented by the term spray evaporative cooling (SEC). This term is misleading because some spray cooling system designs rely very little on the evaporation of fluid to remove heat. In fact, this thesis will later suggest that spray cooling designs with higher values of CHF have less evaporation than designs with lower values of CHF. In order to de-emphasis the significance of the evaporative component of spray cooling, the term spray cooling with phase change (SCPC) is proposed. A possible distinction between SEC and SCPC could be the portion of the heat load that is removed due to latent heat. SEC systems would include spray cooling designs that use latent heat to remove 50% or more of the heat load. SCPC systems would include spray cooling designs that use that use latent heat to remove less than 50% of the heat load.

This thesis describes two experiments. One measured the heat transfer characteristics of 10 spray nozzle designs with a thermal test die. The other experiment used an optical technique to measure the thickness of the multi-phase film through which heat is removed in spray cooling. This thesis links together experimental data from the two experiments to better understand the heat transfer mechanisms associated with spray cooling and therefore what must be done to progress the technology to handle even higher heat loads.

This thesis includes a review of previous spray cooling research. Since spray cooling is a relatively new field, there is not an extensive amount of work that has been done. Experiments that are closely related to some components of spray cooling, such as pool boiling and liquid film boiling, were also researched in order to gain insight into how spray

cooling works. A complete description of the two experimental test stands (the thermal test stand and the visual test stand) is given. Also, a detailed experimental method is provided. Results from the two experiments are separately analyzed. Finally, conclusions are drawn using the results from the two experiments together in order to understand the mechanisms of heat transfer that are at work in spray cooling.

Chapter 2

Background

2.1 Spray Cooling

2.1.1 Spray Cooling with Phase Change

Spray cooling is often generalized by the term spray evaporative cooling (SEC). This common phrase is often misleading in spray cooling cases because the significance of the evaporative component of the process can be small compared to other mechanisms of heat transfer. The thin film that is formed during spray cooling will become a true two-phase layer if sufficient heat is added. Technically, it will be a two-phase layer even under adiabatic conditions due to mechanical entrainment of the vapor [16]. It appears that the importance of the bubbles that are present in the film is not due so much to their latent heat removal as to the turbulent mixing that they promote as they move through the liquid portion of the film. Because the term SEC implies a heavy reliance on latent heat removal due to evaporation, the term spray cooling with phase change (SCPC) is proposed. SEC almost implies a drop-wise evaporation process, which would necessarily lead to a superheated surface unless the droplets were delivered at precisely the right rate so that the previous droplet has completely evaporated and the heat has spread locally to the area where the next droplet should hit. If the droplet arrived too late then the temperature of the surface would pass the Leidenfrost point, leading to a state where the droplet is unable to reach the surface. The Leidenfrost point is a condition where the superheated surface will evaporate the bottom side of a droplet

as it approaches [17]. The vapor formed by this process is trapped between the droplet and the surface. Since the vapor has a low thermal conductivity, the droplet is insulated from the surface heat and it will hover over the surface. This can be demonstrated with a hot pan on a stove by flicking water onto it with your fingers; the drops seem to float over the pan's surface and linger for a long time. At the Leidenfrost point, which is also known as the minimum film boiling (MFB) point, there is a large temperature gradient required to remove heat from the surface. The increase in temperature required to drive the heat from the surface would be damaging to computer dies. The Leidenfrost point is past the critical heat flux (CHF) and therefore should never be achieved in spray cooling. Figure 2.1 illustrates the Leidenfrost effect for a droplet.

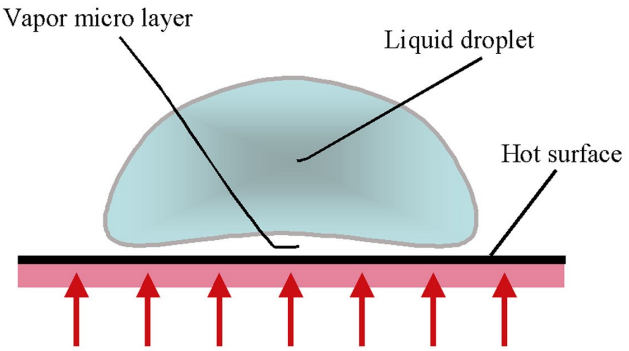

Figure 2.1: The Leidenfrost effect illustrated by a droplet insulated from a hot surface by its vapor [17]

2.1.2 Surface Temperature

Spray cooling has been identified as having several characteristics that make it an appealing choice for a cooling system. One of these characteristics is that temperature gradients observed across the heated surface are often assumed to be small [18]. However, experimental results presented here as well as numerical modeling have shown that this is generally not true [19, 20]. A possible reason for the discrepancy is that many previous spray cooling

experiments have used a single atomizing nozzle with a spray coverage that is larger than the test die. This ensures that the entire test surface experiences a uniform droplet distribution with respect to droplet flux and size. However, this method uses more fluid than is necessary and therefore would not be an economical choice for use in a marketable system. Also, previous studies have provided very limited data for the spatial temperature distribution over the die surface and therefore while it has often been assumed that the temperature distribution is uniform, in fact for many spray systems it is most likely not.

Another common spray cooling assumption is that all droplets that are directed at the spray surface are completely evaporated. Since the saturation temperature of the fluid is the same on all surfaces of the die, this should lead to a uniform temperature distribution. However, drop-wise evaporation is not what is happening in SCPC. Even if the fluid is coming in at saturation temperature, the frequency of the droplets is far too large for all of the fluid to evaporate before another droplet takes its place. Therefore some residual liquid remains and a layer of fluid (referred to as a film) eventually forms. The equation for the spray cooling efficiency (η), defined as the actual energy removal rate to the maximum amount of energy that can be removed by a given flow rate of fluid assuming complete evaporation, is given by Eqn. 2.1, where q'' is the heat flux, A is the die surface area, and Q is the volumetric flow rate of the nozzle cooling the die. For complete vaporization, the efficiency would be 1, but experimental results in Chapter 4 show it to typically be in the range of $0.10 - 0.50$.

$$\eta = \frac{q''\ A}{Q\ \rho_f\ (c_p\ \Delta T_{sat} + h_{fg})} \tag{2.1}$$

2.1.3 Spray Orientation

Another often cited benefit of spray cooling is that it is gravity independent [18]. This, like the idea of uniform surface temperature, is only theoretically true if all of the liquid that

is sprayed onto the surface is evaporated. In this limit, the vapor would have no trouble escaping through the spaces between the droplets in the spray. This would cause a significant portion of the droplets to evaporate before reaching the surface, wasting fluid. This should not typically be the desired mode of cooling as there is an extremely high risk of reaching critical heat flux with any fluctuations in flow rate or heat flux. This mode requires a perfect and therefore unachievable spray distribution with respect to droplet size, frequency, and spacing. In a system where only vapor exits the die would indeed be gravity independent because the vapor can be drawn away from the heated surface in any number of directions. However, in the more realistic case where some liquid remains in the vicinity of the die, gravity does have an effect. Improper positioning of the drain areas will cause flooding around the die that will reduce the system's performance. Many early researchers did not experience this problem because experiments were run with a single simulated die mounted in the center of a large collection tank such as that shown in Figure 2.2 so that excess liquid was free to fall from the sides of the test section. From a systems design stand-point this is not an acceptable geometry, and it has been found that with multi-chip modules (MCMs) used in high-power computing applications the orientation of the system has a strong effect on the critical heat flux [21], possibly due to fluid draining.

2.2 Previous Work

Spray cooling is a relatively new cooling process compared to other heat removal methods. It has been studied in different forms for several decades. As early as 1972, Toda studied the phenomena of mist cooling in heat treating and quenching steel plates [15, 23]. Toda recognized that liquid droplets impacting a surface hotter than the saturation temperature of the fluid resulted in a two-phase heat transfer problem that starts as nucleate boiling and progresses to liquid film boiling at higher surface temperatures. Toda used high speed

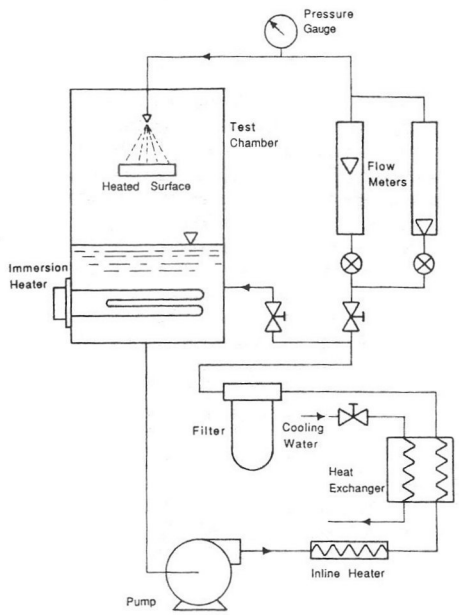

Figure 2.2: Typical set-up of several previous spray cooling experiments allowing excess liquid to escape off the side of the die [22]

photography to study the formation of the thin liquid film and developed a model of the temperature gradient in the film. From his experimental results, Toda generated a boiling curve that is similar to the commonly presented pool boiling curves. Toda's spray cooling curve is shown in Figure 2.3. Many researchers since Toda have studied different aspects of spray cooling and there is some disagreement as to the physical phenomena that are actually taking place.

In previous spray cooling experiments, water has been historically chosen as the primary test fluid [15, 24–26]. Other fluids used for testing include butyl alcohol, n-heptane [24], and FC-72 [27,28]. The heat load is delivered to the fluid through a copper block with embedded heaters [15, 24, 28], a platinum wire [27], or another device that allows accurate measurement of heat flux. The heat flux through the copper blocks in typically calculated using a series of embedded thermocouples by assuming a uniform temperature gradient through the copper.

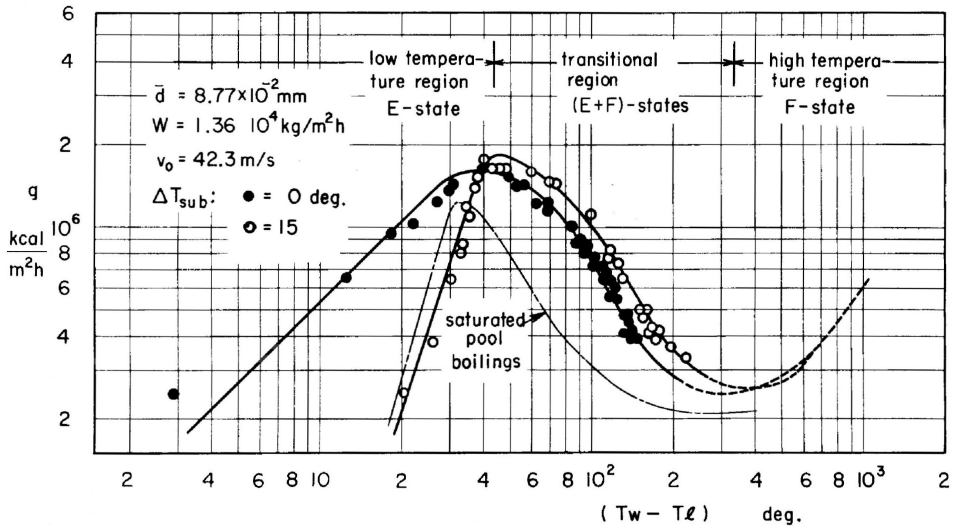

Figure 2.3: Boiling curve for spray cooling [15]

2.2.1 Pool and Flow Boiling

Although spray cooling is an area of heat transfer that is still in large part not understood, many of its basic concepts have been studied in different contexts. Research performed on pool boiling [24–27] and flow boiling [28] systems can be used as a basis for spray cooling models. In pool boiling, the behavior of the fluid at the surface is complicated by fluid motion, heat, surface effects, and phase change, making it difficult to accurately model. The convective heat transfer is driven by two forces, a buoyancy force due to the difference in density between the two phases and a liquid stirring effect that the bubbles provide as they rise (or slide) through the film [26]. This effective stirring length can also be correlated to the lifetime of bubbles as they rise through the film [25].

Higher levels of subcooling have been experimentally shown to decrease the rise time of nucleate bubbles in a film. As the nucleate bubble rises from the hot surface through a temperature gradient to the cooler fluid above, heat is transferred into the bubble through its fluid-vapor boundary. When the bubble's internal vapor pressure becomes too small to overcome the surface tension and fluid pressure forces, it will collapses due to instabilities.

The main parameter that governs this stability is how quickly energy is lost from the vapor bubble to the surrounding fluid, which depends on the amount of liquid subcooling present. As the bubbles move through film, they acts as mixers by pushing cooler fluid toward the surface.

In the studies done, the effective mixing length was measured vertically as the bubbles rose due to buoyancy away from the surface. The length was measured to be on the order of a centimeter. In spray cooling, the film is as much as 200 times thinner than this. However, the film has a high velocity parallel to the surface and therefore instead of measuring the effective stirring length in a vertical direction, for spray cooling it could be assumed that the bubbles will be carried horizontally through the film acting as mixers. The lifetime of the bubbles that are formed will likely be longer than the time it will take for them to be swept off of the die surface.

Many studies have been done related to the effects of surface enhancements on the rate of convective heat transfer. It has been found experimentally that in pool boiling more surface nucleate bubbles will cause the convective heat transfer rate to rise through both agitation and latent heat. Data show that as much as 70% of the heat is removed due to latent heat [27]. In addition, it was concluded that the increase in heat transfer observed with a microporous surface was due to the increase in active nucleation sites, not the additional surface area. With a rougher surface, there are more active nucleation sites available with a smaller average nucleate bubble diameter. At high heat fluxes, this reduces the superheated liquid layer, inhibiting latent and enabling more convective heat transfer [27]. This will lead to a rise in the CHF as long as the superheated liquid layer remains below the homogenous boiling point of the fluid. The primary role of nucleate bubbles in pool boiling heat transfer is to mix the liquid. If another mixing mechanism were present, less surface boiling would be required to achieve the same degree of fluid mixing, raising the critical heat flux.

2.2.2 Suppression of Nucleate Boiling

Experiments in thin liquid film boiling have studied the suppression of nucleate boiling and how it relates to liquid film thickness and critical heat flux. As heat flux is increased past the point where a multi-phase film occurs, a condition arises where nucleation is suppressed. Theories have stated that this happens when the film thickness, due to vaporization, thins down until it is approximately equal to the critical radius of the nucleate bubble; this has subsequently been shown to be false [24]. Experiments with pressure held constant indicated that the thickness at which nucleation is suppressed decreases as the heat flux increases, down to 60 - 300 μm for a variety of fluids under liquid film boiling conditions [24]. It is likely that the suppression of nucleate boiling leads to critical heat flux due to a lack of agitation by nucleate bubbles and not due to less latent heat flow. The unmixed fluid reaches the homogeneous nucleation point, causing an insulating vapor layer to form at the hot surface, preventing the liquid from coming into contact with it. The lower thermal conductivity of the vapor requires a higher temperature gradient to drive the same heat flux from the surface.

In a spray cooling system, it may be desirable to suppress nucleate bubbles from forming at the surface. If the bubbles were to grow to their full potential, their diameter would quickly become larger than the thickness of the film. This would lead to an area of the die underneath the bubble that will not be in contact with the fluid, which would lead to critical heat flux. If there were no nucleate bubbles forming at the surface, critical heat flux will be delayed. The high frequency of droplet impacts will likely lead to a large number of entrained vapor bubbles, as will be discussed in Section 2.3.1. These droplet impacts, along with the movement of the entrained bubbles through the film, will serve to mix the fluid. With this mixing occurring, the primary function of the nucleate bubbles, which have now been suppressed, is still present.

2.3 Nucleate Bubbles

Spray cooling involves components of both single- and multi-phase heat transfer. The effect of each of these components varies from one system to the next. There has been much previous research done on thin single-phase films and their heat transfer characteristics. The multi-phase heat transfer component is less understood. There are three possible sources for the secondary gas phase. The first and primary source is preferred site nucleate boiling, as seen commonly in pool boiling. This is illustrated in Figure 2.4. This is well studied and won't be discussed in this thesis. A good reference for this is Rini's thesis [16]. A secondary source of gas is through entrainment. The third possible source of gas in the film is due to out-gassing of noncondensables from the test fluid.

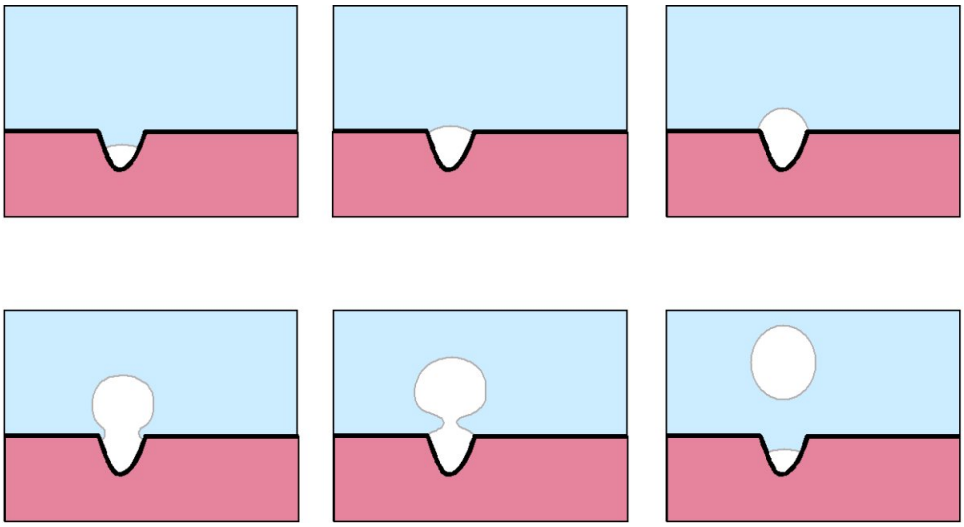

Figure 2.4: Nucleate bubble growth from a surface feature [17]

2.3.1 Secondary Entrainment

Rini performed research at the University of Central Florida pertaining to the nucleation site density at the surface during spray cooling [16]. A diamond substrate heater with a Ni-Cr wire was used as a semi-transparent powered test die. This allowed a high speed CCD

camera to capture images of the die's surface during spray cooling. Data was collected on the size, growth, and lifetime of the nucleate bubbles. It was found that the fixed nucleation site density and the secondary nucleation coefficient (entrained bubbles and bubbles forming as primary bubbles burst) could not be exactly determined, even with the use of a high-speed camera. The size of the nucleate bubbles reported by Rini range from $174 - 282$ μm in diameter with nucleation site densities from $1000 - 4044$ $sites/cm^2$. Based on his measurements of bubble size and density, Rini estimated that between 38 and 49% of the heat flux was due to nucleate boiling. The fluid was not subcooled, and no explanation was given as to how the remaining percentage of the heat flux was removed. Other researchers have claimed that 100% of the heat is removed through phase change [29, 30]. Rini also accounts for entrained bubbles as a possible mechanism for heat transfer in spray cooling. The conclusion of his study was that the primary reason that spray cooling works better than pool boiling is that the much sorter lifetime of the nucleate bubbles, due to the high film velocity, prevents the conditions that lead to CHF.

Tan [31] performed research at the University of Central Florida to further model and understand Rini's findings of fixed nucleation sites and entrained nucleation sites. To determine the theoretical influence of these two types of nucleation processes, a computer model was developed to predict the behavior of the nucleate bubbles and the effects that they have on heat removal. The model predicts bubble sizes from $121 - 177$ μm and nucleation site densities from $0 - 500$ $sites/cm^2$. In the test case where no bubbles form at the surface and a droplet flux of $2,000,000$ $droplets/cm^2 - s$ was assumed, the model predicts a heat flux of 11.8 W/cm^2 , due primarily to the effects of phase change. Since the fixed nucleation site density was set to 0 $sites/cm^2$, it implies that this heat flux can be attributed to the entrained bubbles. When the nucleation site density was increased to 500 $sites/cm^2$ there was a less than 3% increase in the heat flux due to phase change. Based on this model, the phase change that occurs at the die surface has a minimal effect on the heat levels removed.

This does not match the experimental results obtained by Rini where it was determined that the number of active nucleation sites on the die surface was directly related to the total heat flux. Nucleate bubbles were measured to be smaller, in the range of $102 - 113\ \mu m$.

Bergman and Mesler state that nucleate boiling relies on bubbles to augment heat transfer, and that bubbles bursting in a thin film form other tiny bubbles that serve as additional nucleation sites [32]. Nucleate bubbles also cause mixing in the film, leading to higher heat transfer coefficients. It has been proposed that secondary nucleation is a key factor in spray cooling for removing high heat loads [16]. If bubbles are entrained in the flow instead of forming at the heated surface, fewer surface bubbles are required to remove the heat load. With less surface nucleation, the vapor layer that leads to CHF will be suppressed. Entrainment of bubbles by droplet impacts has been studied extensively. Carroll and Mesler [33] found that as droplets impact a surface, bubbles on the order of 50 μm form following the entrainment and collapse of a vortex ring. The vortex ring forms as the impact waves on the surface of the film and on the surface of the droplet impact each other, trapping vapor. The vapor is pushed into the film by the collapsing of the surface waves. It is an unstable structure and breaks up into numerous smaller bubbles. This type of entrainment typically occurs at low droplet velocity. The bubbles were carried $1 - 2\ cm$ beneath the surface, implying that testing was done with a much thicker film than is present in spray cooling.

Pumphrey and Elmore [34] also studied bubble entrainment from impacting droplets. They found three regimes of bubble entrainment. The type of entrainment that was described by Bergman and Mesler has come to be known as Mesler entrainment. This type of entrainment mostly occurs with very small impact velocities. The number of bubbles entrained is highly unpredictable, even with careful control of the droplet size and velocity. The other two types of entrainment studied by Pumphrey and Elmore are referred to as regular and irregular, or Franz, entrainment. These occur under different fluid conditions. Regular entrainment is very repeatable and predictable. Figure 2.5 shows Pumphrey and Elmore's

dimensionless analysis of regular entrainment for water. The figure is given in terms of two commonly used dimensionless parameters in sprays, the Weber (We) and Froude (Fr) numbers, which are defined in Eqn. 2.2 and 2.3. In the equations, v_{d-z} is the axial velocity of the droplet, ρ_f is the fluid density, σ is the fluid surface tension, d is the droplet diameter, and g is the acceleration due to gravity. The two lines are the limits at which entrainment was observed. Nozzle 0A is also plotted on the figure at different test conditions. According to Pumphrey and Elmore's model, there should be regular entrainment with this nozzle design. Irregular entrainment is not predictable, but since the liquid droplets are hitting the film surface at a very high frequency, it is likely that vapor will be irregularly entrained through collapsing of waves or droplet impacts.

$$We = \frac{\rho_f \ v_{d,z} \ d}{\sigma} \tag{2.2}$$

$$Fr = \frac{v_{d,z}^2}{d \ g} \tag{2.3}$$

2.3.2 Noncondensable Gasses

The third possible mode of entry for nucleate bubbles in the film is through changes in the gas solubility of the test fluid. The Henry's constant (H) of perfluorohexane has been measured to be approximately $5.4 \times 10^{-5} \ mol/mol - kPa$. The concentration of the gas dissolved in the liquid (C_g) is found using Eqn. 2.4 where P_g is found using Eqn. 2.5. Henry's constant and the saturation pressure are both functions of temperature. As the temperature of the fluid increases, the amount of gas that can be dissolved in it decreases. If the fluid has been saturated by a gas, as the fluid temperature rises, some of this gas will evaporate, forming bubbles in the film and enhancing fluid mixing.

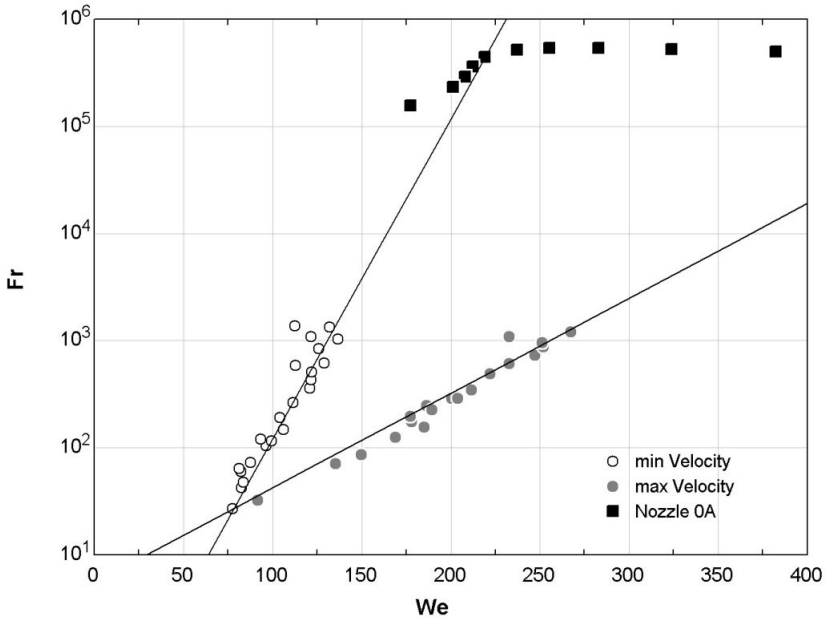

Figure 2.5: Dimensionless model of regular entrainment of bubbles [34]

$$C_g = H(T)\ P_g \tag{2.4}$$

$$P_g = P_{tot} - P_{sat}(T_{sat}) \tag{2.5}$$

Recent research done by Horacek et al. studied the effects that gasses saturated in the fluid have on the CHF and wall temperatures during spray cooling [35]. In this study, the saturation level of the fluid and the temperature of the fluid entering the cap was controlled using a vacuum pump and an in-line chiller. Two types of subcooling were defined, "gas subcooled" and "thermally subcooled." Thermal subcooling is achieved using a chiller to lower the temperature of the fluid after the system reservoir but before atomization. Gas subcooling is achieved by altering the system pressure by adding an noncondensable gas.

The pressure of the system reservoir will be approximately equal to the pressure of the spray chamber. Increasing the pressure in the reservoir by the addition of gas (such as nitrogen) allows for control of the saturation temperature of the fluid while maintaining the bulk of the fluid near room temperature. Horacek et al. found that gas subcooling led to higher CHF values than thermally subcooling, but at the cost of increased surface temperature elevation. Only limited testing was performed using thermal subcooling, but it was found that it lead to a higher CHF than no subcooling and did not cause a significant increase in surface temperature. Although the effects of outgassing in the film was not considered by Horacek et al., this may explain the difference between gas and thermal subcooling. Gas subcooling would be preferred in most systems because it doesn't require additional equipment, such as a chiller, and gives higher performance characteristics, possibly due to the additional mixing of the film due to gas de-saturation.

In a study of pool boiling done by Kubo et al., the effects of dissolving a gas in perfluorohexane with respect to heat transfer performance were measured [36]. It was discovered that tests run with pure (degassed) perfluorohexane , the boiling incipience was found between $8 < \Delta T_{sat} < 20K$ with a noticeable temperature overshoot. When air was dissolved in the perfluorohexane, boiling incipience was seen at $\Delta T_{sat} \approx -10K$ with a very small temperature overshoot. When the fluid was degassed and thermally subcooled, the point of boiling incipience was reduced but the temperature overshoot remained. Kubo stated that the performance of gas-dissolved perfluorohexane was better than with the fluid degassed. A similar study with similar findings was also run by Rainey et al. [37].

Despite the significant amount of research done on spray cooling using single nozzles, very little research has been done with multi-nozzle arrays [19]. Using multiple nozzles allows for much larger area to be covered and can allow for higher levels of heat removal. However, the characteristics of the cooling capacity of a multi-nozzle arrays is not the same as a single nozzle array [19]. Multiple nozzle arrays have been studied and reported by

Cray Inc. [4], the University of Wisconsin-Madison [19], the Pontificia Universidade Católica do Rio de Janeiro in Brazil [38] and the Air Force Research Laboratory. Research done at the Air Force Research Laboratory by Lin and Ponnappan compares different flow rates and working fluids [39, 40], but the results were not compared to a single nozzle. Heat transfer coefficients with perfluorohexane as the working fluid were calculated to be $1.7 - 2.2$ $W/cm^2 - K$ for the flow rates and nozzle array tested. Lin and Ponnappan also studied the effects of noncondensable gases dissolved in the working fluid. They found that the addition of air to perfluorohexane caused the CHF to increase but also caused the temperature of the wall to increase.

2.4 Film Thickness

Previous experiments have attempted to measure the thickness of the thin film in spray cooling. The experiments were run using water as the test fluid with an air-atomizing nozzle [41]. An average value of the maximum thickness of the film was measured using Fresnel diffraction and the variation of the film thickness was measured using a holographic method. It was found that with a constant air pressure, increasing the flow rate of the water led to an increase of the film thickness. The thickness of the film was found to be between 85 and 235 μm , depending on the flow rate of the water. Using the holographic method, these researchers concluded that in the area of the film that was studied, the variation in the thickness of the film was less than 1 μm .

An earlier estimate of film thickness was made by Tilton by measuring the film thickness after the hydraulic jump of a single nozzle with a needle mounted on a traversing measuring scope [42]. Based on continuity requirements for a single-phase film, the film thickness was estimated before the hydraulic jump, in the area under the spray. Uncertainties of approximately 200 μm in the measurements of the film thickness after the hydraulic jump

led to an estimated uncertainty of 10 percent in the values for the film thickness under the spray. It was assumed that the film had a uniform thickness under the spray. Film thickness values were reported at $120 - 350\ \mu m$. These measurements were taken adiabatically.

A variation of the method presented in this paper was used to determine the instantaneous thickness of a film resulting from the impingement of fuel spray on a flat, horizontal surface [43]. These researchers measured film thicknesses of 20 to 50 microns for films of iso-octane resulting from 110 to 350 micron droplets impinging at velocities of 10 to 21 m/s. Other numerical models have been developed to predict the film thickness in non-adiabatic conditions [44]. Assuming a constant volumetric flow rate, film thickness values between 1.0 and 1.8 μm were predicted for heat fluxes of 28.4 to 12.2 W/cm^2 , respectively.

Chapter 3

Experimental Description

3.1 List of Equipment

3.1.1 Heat Transfer Stand

The heat transfer testing apparatus was donated to the University by Cray Inc. The test stand consisted of two parts: the fluid delivery system and the instrumentation system. The fluid used for testing was the fluorocarbon perfluorohexane. It is a dielectric fluid often used in electronics cooling applications. It was commonly known as the 3M specialty fluid FC-72 and has the properties listed in Table 3.1 [45]. The fluid delivery system was comprised of a fluid reservoir, pump, various filters, flow meter, system manifold, spray cap, spray plate, and heat exchanger. A schematic of this facility is shown in Figure 3.1, and a photograph is shown in Figure 3.2. The pump was a custom designed gear pump manufactured by MicroPump. Considerations in material selections for pump parts were made based on the properties and solubility of the test fluid being used. There are complications with using perfluorohexane with teflon because the teflon will absorb it and swell. This will cause moving parts to bind and may cause seals to leak, so Viton was used instead. Oil could not be used in any of the bearings because it would contaminate the system. The pump was magnetically coupled to a Leeson 1/2 horsepower AC motor model number PR000108. The fluid was run through a 5 μm particulate filter to remove any particles suspended in the fluid.

Property	*Perfluorohexane*	*Water*
Appearance	Clear, colorless	Clear, colorless
Chemical formula	C_6F_{14}	H_2O
Average molecular weight	388	18.02
Boiling point $[^o\ C]$	56	100
Pour point $[^o\ C]$	-90	0
Latent heat of vaporization $[J/g]$	88	2258
Liquid density $[kg/m^3]$	1680	997
Liquid thermal conductivity $[W/m-C]$	0.057	0.595
Liquid specific heat $[J/kg-C]$	1100	4183
Surface tension $[N/m]$	0.01	0.072
Dynamic viscosity $[kg/m-s]$	6.4×10^{-4}	1.03×10^{-3}
Liquid electrical resistivity $[ohm-cm]$	1.0×10^{15}	5×10^4
Liquid gas solubility $[mol/mol-kPa]$	5.4×10^{-5}	

Table 3.1: Properties of perfluorohexane compared to water properties at standard temperature and pressure

After the particulate filter, a portion of the fluid was directed through a fluid conditioning by-pass loop. This loop consisted of two filters. One filter is a perfluoroisobutylene (PFIB) filter. PFIB is a harmful chemical byproduct formed when perfluorohexane degrades at high temperatures. It was highly unlikely that a sufficiently high temperature would occur in the test stand, but the filter was included as a safety precaution. The other filter in the by-pass

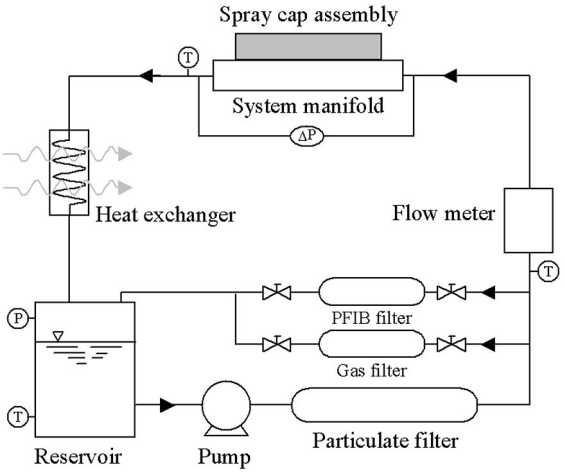

Figure 3.1: Thermal test stand schematic

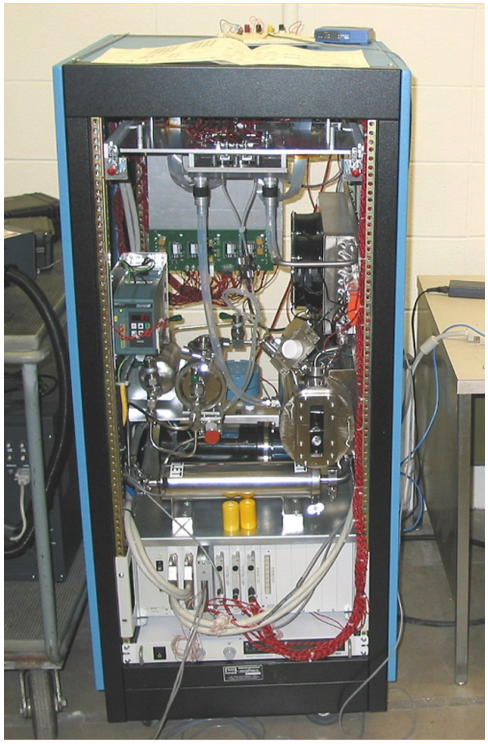

Figure 3.2: Picture of the thermal test stand

loop was an Aeronex Gate Keeper model SS-500KF-I-4R inert gas purifier. It contained activated aluminum oxide, which will absorb many impurities in the fluid, such as dissolved oxygen and water vapor. This fluid was returned to the reservoir after filtration. The fluid that did not pass through the filter by-pass loop passed through a flow meter. The flow meter was a Model F025 MicroMotion BASIS coriolis flow meter which measured the volumetric flow rate (Q) and temperature (T_{in}). The device measured the temperature of the fluid to $\pm 1^o\ C$ and the volumetric flow rate to 0.30% of the full-scale flow rate, or approximately $\pm 3\ mL/min$.

The fluid was then delivered to the system manifold through a quick-disconnect fitting and channelled into the spray cap. The spray cap can be seen in Figure 3.3. The spray cap was mounted to the multi-chip module (MCM) with eight compression springs, as seen in Figure 3.4. There was a viton O-ring to form a face seal between the cap and the MCM.

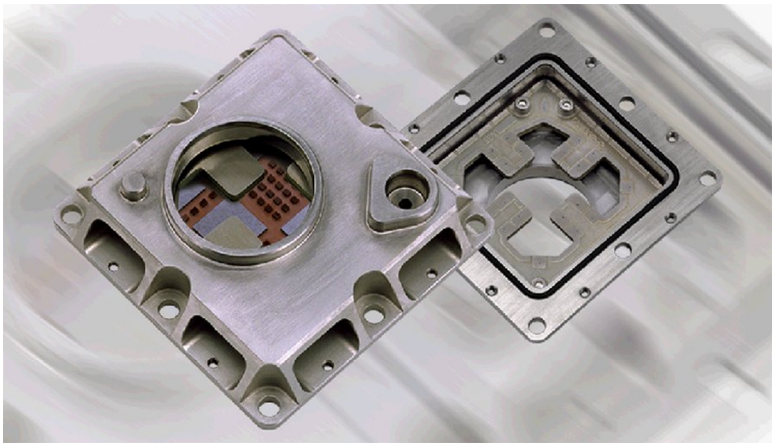

Figure 3.3: Picture of the spray cap with the MCM and spray plate

Inside the spray cap, a spray plate was mounted. The spray plate was located to a 0.05 mm tolerance directly over the center of the test dies. A viton O-ring made a face seal between the spray plate and the spray cap. The spray plate was orientated to deliver the fluid in an upwards direction such that the draining would be gravity assisted, as shown in Figure 3.5. Fluid leaving the spray cap passed through the system manifold and another quick-disconnect fitting into the heat exchanger unit. The quick-disconnect fittings were custom

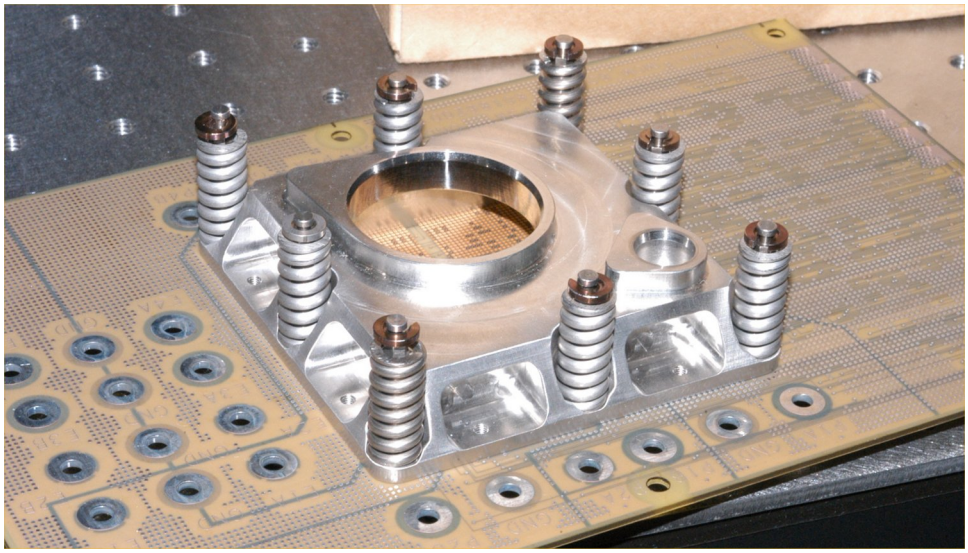

Figure 3.4: PCB board and spray cap picture

designed by Parker Hannifin Corp. for high flow rates with perfluorohexane compatibility. The fittings allowed for removal of the test node from the rest of the system without opening the system to the environment, which would allow oxygen and water vapor in. The heat exchanger was a fin and tube liquid to air heat exchanger with copper fins and stainless steel tubes. Two 112 cfm fans were used to drive air through the heat exchanger. The fan speeds were varied to match the heat load being added by the test dies in order to hold the temperature of the fluid in the reservoir constant. Fluid leaving the heat exchanger unit was delivered to the reservoir. The reservoir tank was a 5-liter stainless steel vessel. The entire fluid delivery system was manufactured from stainless steel except for the filter materials, the quick-disconnect fittings, O-ring seals, and short lengths of flexible tubing. Before initial testing, the entire fluid delivery system was evacuated to 28 inHg vac with a vacuum pump. Fluid which had been pre-conditioned was pumped into the evacuated system. The pre-conditioning was done with a Cray Inc. Fluid Conditioning Unit (FCU) at Cray before the fluid was delivered to UW-Madison. Conditioning involves a thorough boiling and recondensing process to remove dissolved gasses followed by filtration with a 5 μm filter.

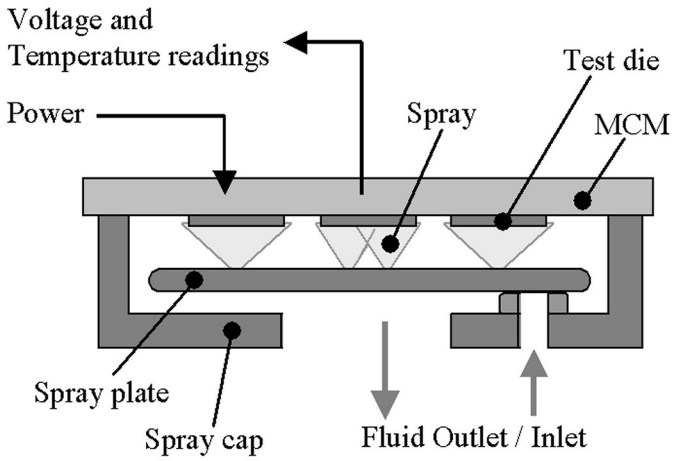

Figure 3.5: Spray cap assembly

Tests were performed with five different spray plates. Each spray plate had two designs of nozzle arrays, each design was duplicated 4 times per plate for a total of eight nozzle arrays per spray plate. A nozzle array is defined as a nozzle or set of nozzles designated to cool one die. The geometric and flow characteristics of the nozzle array designs is given in Table 3.2. The nozzles were designed and manufactured by Parker Hannifin Corp. Each nozzle was a pressure-swirl atomizer consisting of a swirl chamber, two inlet slots, and a center jet to form a full spray cone as seen in Figure 3.6. The orifices of the nozzles were 0.358 mm in nozzle array 0B and 0.327 mm in nozzle array 0A, the two designs for which the most research was centered on. The centers of the nozzle arrays were located 6.8 mm directly below the centers of the test dies and the spray was directed upwards. Design 0B's nozzles were arranged in a square pattern with 7mm spacing between nozzles, as shown in Figure 3.7. The relative locations of the test dies on the MCM are shown in Figure 3.8.

The instrumentation system included all of the necessary electronic equipment to drive the fluid delivery system, to power the eight test dies, and to acquire any necessary measurements. The data acquisition system was a National Instruments SCXI-1001 chassis. Six modules were used. Three modules were 1102 32-channel analog input boards. One of these had a 1303 terminal block with a thermistor as a cold junction for thermocouple temperature measurements. These were used to take temperature measurements from the test dies, voltage and current measurements, pressure readings, flow rate readings, and thermocouple

Spray Plate Design Number	*Nozzle Array A*			*Nozzle Array B*		
	No.	Pattern	Flow Rate [mL/s]	No.	Pattern	Flow Rate [mL/min]
0	1		0.85	4		3.61
1	1		0.38	4		2.16
10	5		0.44	5		2.06
11	2		0.12	9		1.09
13	3		0.39	16		2.32

Table 3.2: Characteristics of the nozzle arrays tested at a test pressure of 25 psi. Flow rates are per die

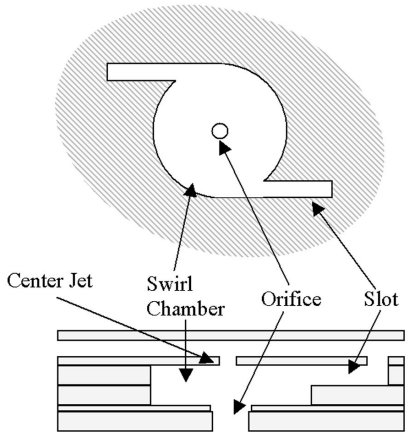

Figure 3.6: Cross sectional diagram of a typical pressure-swirl atomizer

temperature measurements of the fluid and air. Two modules were 1124 6-channel analog output boards. These were used with the Vicor power converters in the active power control circuits described below. The final module was an 1163 32-channel digital input/output board. This was used to send enable signals to the main power supply, heat exchanger fans, pump, and Vicor power converters.

The pump's control circuitry included a solid-state relay for switching on and off and a pump controller for motor speed adjustments. The pump controller was a Reliance Electronics SP 200. Two additional solid state relays were used to control the heat exchanger fans. These were Continental Industries Inc. S505. Two pressure transducers were used in

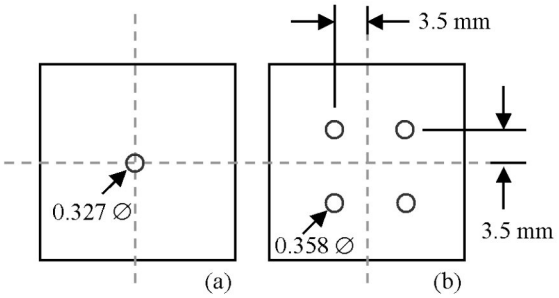

Figure 3.7: Locations of nozzles relative to dies for designs (a) 0A and (b) 0B

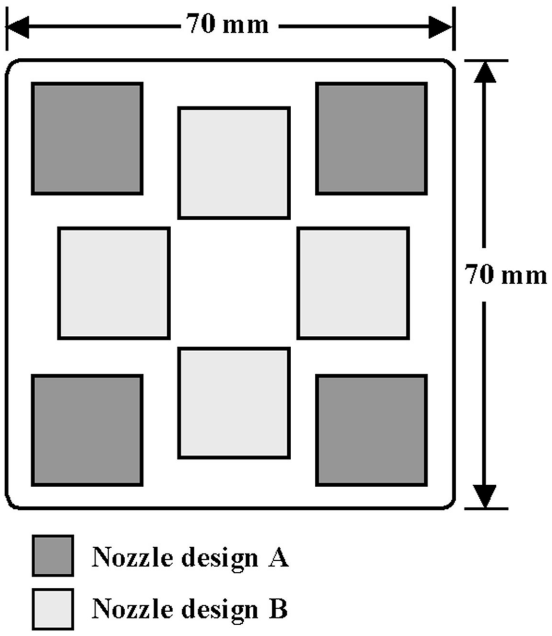

Figure 3.8: Locations of die on MCM

the system. Both were custom designed by Sensotec. One transducer was 0-25 psia model 060-G09391. It was used to measure the system absolute pressure in the fluid reservoir (P_{res}). The other was model 060-F89602. It was a 0-50 psid pressure transducer used to measure the pressure drop across the spray plate(ΔP_{cap}). Both transducers output 0-5 volts DC. An additional pressure transducer was used to measure the cap pressure (P_{cap}) but its output was unreliable and was not used for testing.

The main power supply was a Xantrex XFR 60-20. It was used to deliver 48 Volts DC to the Vicor power converter boards. There were four Vicor boards, which were custom designed by Cray Inc. to power the test dies. Each Vicor board received 48 volts from the main power supply and a control voltage of 0 - 5 Volts DC from that data acquisition system. It would then output 0 - 12 Volts DC to the test dies. Each of the four Vicor boards had two channels for a total of eight individually controllable power sources. Each Vicor channel had a current measurement, which was output to the data acquisition system. The voltage of

each channel was measured on the MCM to eliminate losses in the line and the connections. The measured voltage and current were multiplied together in the control program to obtain a power reading. The control program adjusted the control voltage to each of the Vicor power supplies, allowing active control of the power level of each die.

The Vicor power supplies are supported by two signal conditioning boards. These boards were also custom-designed and consisted of high-precision resistors that act as voltage dividers to allow the data acquisition system, having channels with limited range, to measure voltages that exceeded this range. The boards also serve as adapters for the flexible cables that carry the signals off the PCB board that houses the MCM. All of the enable and control signals pass through one of the two signal conditioning boards, as well as many of the measurements of voltage, current, and temperature from the power supplies and from the MCM.

The test dies were integrated circuits developed and built by IBM Corp. Eight test dies were contained on one MCM, each measuring 15 mm on a side and being square in shape. The MCM itself was 70 mm long by 70 mm wide by 5.25 mm thick. The dies each contained four resistive heating elements that were uniformly powered during testing. The Vicor variable DC power supplies powered the heating elements. Each test die was built with nine temperature sensors (silicon diodes) integrated in the silicon. One sensor on each die was designed to be connected to a mechanical safety device to cut off power in the event of a failure of the software-based control system. This sensor could not be monitored by the data acquisition system. Of the eight sensors that were monitored, three were located in the corners of the die, four were located in the center of each of the four quadrants, and one was at the center of the die as shown in Figure 3.9. A 1.00 mA current was passed in series through the temperature sensors and the voltage difference was measured across each one. Calibration of the temperature sensors was performed in a test oven. The temperature of the oven was set to $25^o\ C$ and held for 30 minutes. Measurements of the voltage difference

across each temperature sensor were then made. This process was repeated for temperatures of 40, 60, and 80^o C. A curve fit to the data was performed, showing that a linear relation between voltage and temperature was sufficient, exhibiting a correlation constant of 0.99 or greater. Based on the resolution of the data acquisition system, the accuracy of these diodes was calculated to be no worse than $\pm 0.2^o$ C. These devices measure the junction temperature of the die directly, which is the parameter of primary concern for electronic dies' failure and reliability [2,3]. The surface temperature can be assumed to be close to the junction temperature due to the fact that the layers of silicon and silicon-oxide on surface between the junction plane and the free surface are conductive and extremely thin, on the order of microns.

The MCM has 3,600 gold contact pads on its back surface for signal and power input and output. An electrical connection was made between the MCM and the test PCB board

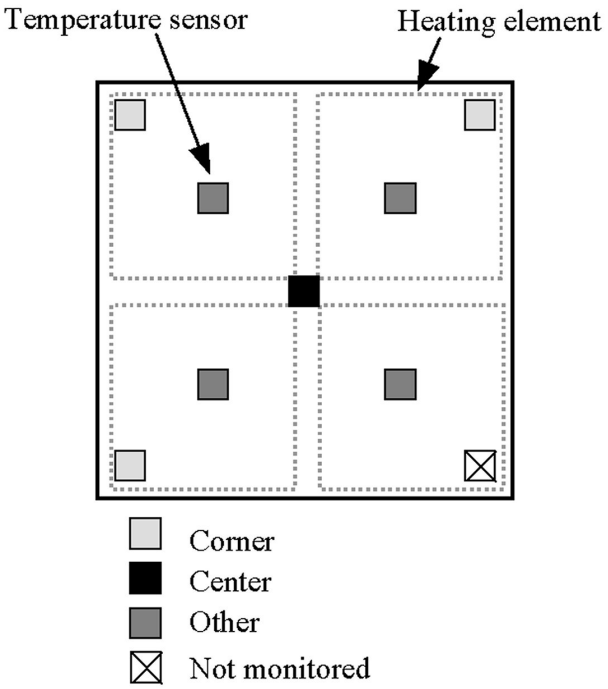

Figure 3.9: Location of heating elements and temperature diodes on die

through interconnects manufactured by InterCon. The interconnects consist of an array of tiny gold springs. When a great enough force is applied to the springs, a low-resistance electrical connection is made. The PCB board was custom designed by Cray and manufactured by Honeywell, and is shown in Figure 3.4. Edge connecters carried signals from the board to the signal conditioning board. Power busses connected the Vicor power supplied to the heating elements of the dies.

The test stand was controlled by a LabView program that was written specifically for this purpose. The program would output the die temperature distribution, the die power levels, and the state of the fluid delivery system, including the fluid flow rate, pressure, and temperature at several locations. The program also allowed for control of the power level of all of the test dies, the pump, and the fans. It could record data sets either as individual points or at a defined time interval and output them to a file specially formatted to be imported to the software used to analyze the data.

3.1.2 Spray Visualization Stand

With the spray continually hitting the surface, it is difficult to make a measurement of the film thickness in a closed system. The non-intrusive optical technique used in this research involves the total internal reflection of light at an interface between materials with two different indices of refraction (n_1 and n_2) [46]. The theory of this method can be derived from Snells's Law, Eqn. 3.1, and the Fresnel relations, Eqns. 3.2, 3.3 [47]. As illustrated in Figure 3.10, when n_1 is greater than n_2, an incident angle θ_i can be determined that will lead to the transmission angle θ_t being 90^o. At this point, none of the light is transmitted and all that is not absorbed is reflected back at a reflectance angle $\theta_r = \theta_i$. The angle at which this occurs is the angle of total internal reflection, also called the critical angle, θ_c. Figure 3.11 shows reflectance versus incident angle for a glass-air interface calculated from the Fresnel

relations. The figure plots the two polarizations of light and an average of the two assuming equal parts of both polarizations. The figure shows that at small angles, approximately 4% of the light is reflected. All of the light is reflected when the incident beam is at the critical angle. In the case plotted in Figure 3.11, the critical angle is approximately 42^o.

$$n_1 \sin(\theta_1) = n_2 \sin(\theta_2) \tag{3.1}$$

$$R_\perp = \left[\frac{n_1 \cos(\theta_i) - n_2 \cos(\theta_t)}{n_1 \cos(\theta_i) + n_2 \cos(\theta_t)}\right]^2 \tag{3.2}$$

$$R_{||} = \left[\frac{n_2 \cos(\theta_i) - n_1 \cos(\theta_t)}{n_2 \cos(\theta_i) + n_1 \cos(\theta_t)}\right]^2 \tag{3.3}$$

When measuring the film thickness using the total internal reflection method, light must be scattered from a light source in all directions. This is accomplished using a light diffuser. An ideal light diffuser is made up of a large number of perfectly reflective spheres; light from a coherent, collimated light source, such as a laser, enters the diffuser and is reflected

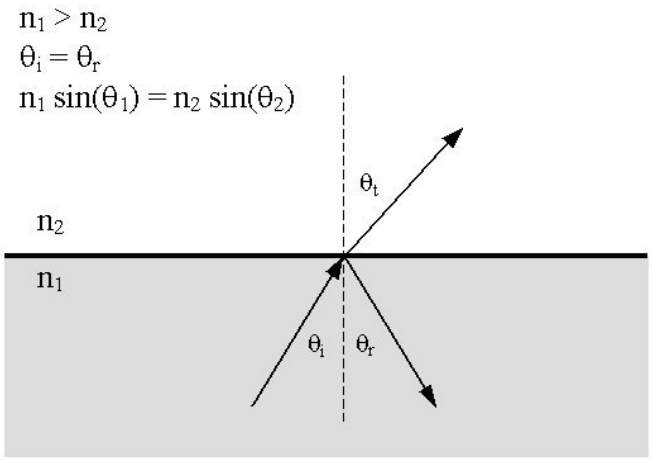

Figure 3.10: Graphical representation of Snell's Law

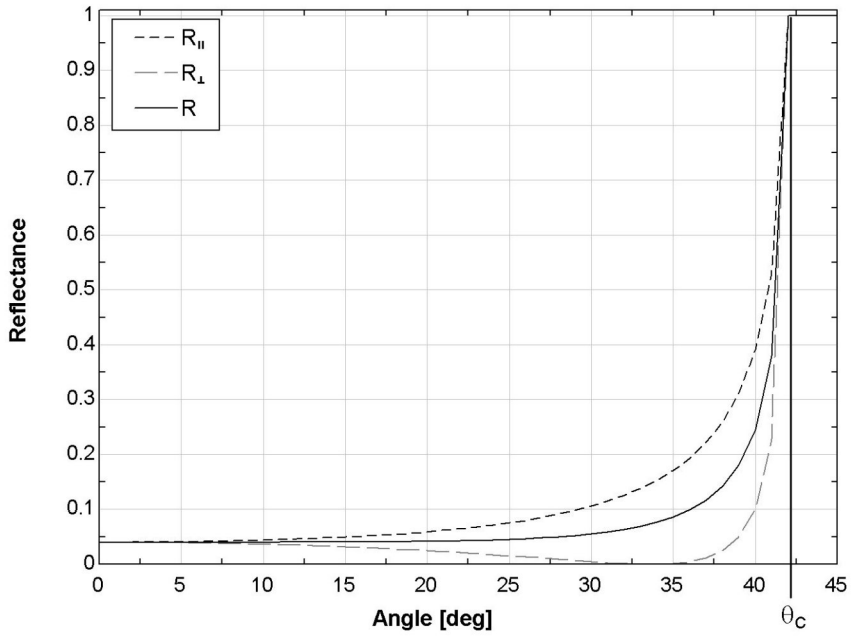

Figure 3.11: Typical reflection versus incident angle showing the critical angle

in random directions by the diffuser. When the scattered light hits an interface at incident angles less than the critical angle, most of the light intensity is transmitted and a small part is reflected. At the critical angle, all of the light is reflected. This light bounces back to the outer wall surface and hits the diffusing material, where it is again scattered, as seen in Figures 3.12, 3.13 and 3.14. More light is reflected at θ_c and a light ring forms. A camera captures this scattered light, and the diameter of the resulting light ring is measured. If the indices of refraction of the materials are known, then the thickness of the film can be calculated from the radius of the light ring (r) [46, 48].

The equations used to calculate the film thickness become more complicated when the interface between the two fluids is not parallel to the die surface, as illustrated in Figure 3.13. This is true when measuring a spatially varying film thickness. The angle of the interface, ϕ, is typically assumed to be 0^o. The critical angle is measured from an axis perpendicular

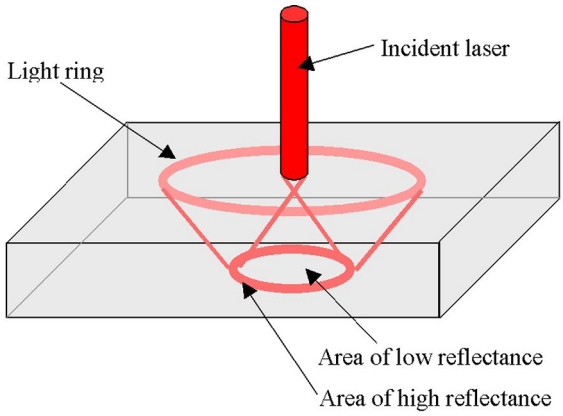

Figure 3.12: Three dimensional representation of the formation of the light ring

to the film surface, so the greater ϕ is, the more the radius r deviates from the flat surface model. A numerical model was developed for this experiment to find the film thickness for a sloping interface with the fluid slope angle as an input and is included in the appendix. This model showed that the small angle approximation can be used to correct for this effect for angles less than 5^o. Films that slope at an angle greater than this must be analyzed more carefully, taking into consideration the magnitude and direction of the slope.

If a radius can be measured on two sides, then both the slope of the film and the film thickness can be measured simultaneously. Figure 3.14 shows an expanded sloping film model with two radii measured. The following equations can be used to calculate the film

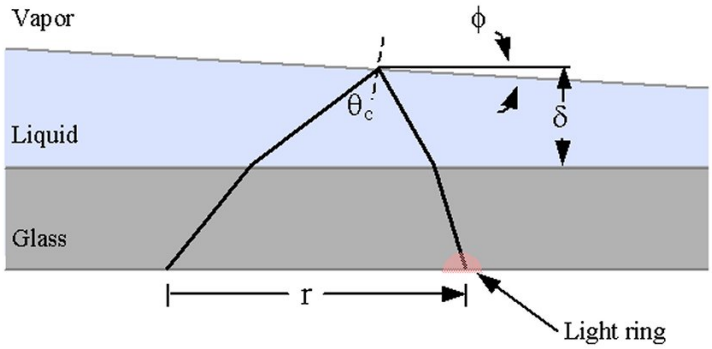

Figure 3.13: Sloping film model

characteristics. Equation 3.4 shows the calculation of the critical angle of the film to air interface. The required angles of incidence between the glass and the film ($\theta_{i,1}$ and $\theta_{i,2}$) are calculated with Eqns. 3.5 and 3.6, which are derived from Snell's Law. The radii $r_{1,a}$, $r_{1,b}$, ... are found with basic geometry. Finally, the film thickness and the slope can be found by simultaneously solving Eqns. 3.7 and 3.8.

$$\theta_c = sin^{-1}\left(\frac{n_3}{n_2}\right) \tag{3.4}$$

$$n_1\ sin(\theta_{i,1}) = n_2\ sin(\theta_{i,2} + \phi) \tag{3.5}$$

$$n_1\ sin(\theta_{i,1}) = n_2\ sin(\theta_{i,2} - \phi) \tag{3.6}$$

$$tan(\phi) = \frac{t_{2,2} - t_{2,1}}{r_{1,a} + r_{1,b} + r_{2,a} + r_{2,b}} \tag{3.7}$$

$$tan(\phi) = \frac{t_{2,2} - t_2}{r_{1,a} + r_{1,b}} \tag{3.8}$$

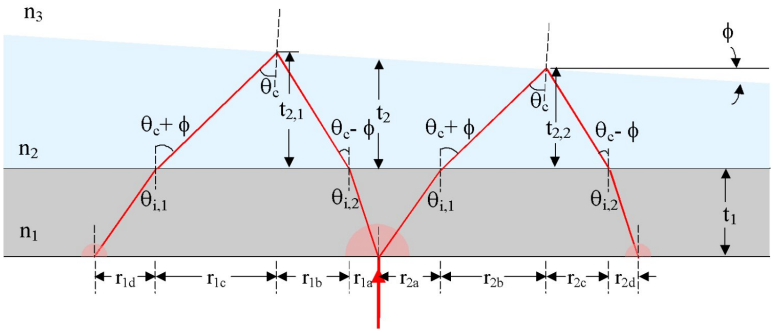

Figure 3.14: Dual ring sloping film model

In order to fully visualize the entire spray-affected surface, a transparent test die was developed for this experiment. Similar dies have been used in previous flow boiling experiments [49]. The dies had a 2000 Å coating of indium tin oxide (ITO) on one side of a 17 mm x 17 mm x 0.5 mm piece of Corning 1737 aluminosilicate glass. These glass slides were purchased as a custom order from Delta Technologies, Limited, part number CB−50in17x17/0.5. The nominal resistance of the ITO-coated sides of the dies was 10 Ω. Positive and negative lead wires were attached to the die using a silver-composite epoxy to create a transparent resistive heating element, as pictured in Figure 3.15. The epoxy was a conductive thermoplastic silver composition from DuPont, part number 4922N, which is acrylic-based and has a high viscosity. As shown in Figure 3.16, the wire leads were fed through holes in the backside of the mounting plate and sealed with an epoxy to prevent leaks.

To make film thickness measurements, the side of the die that did not have the ITO coating was made into a diffuse surface by applying a thin layer of acrylic paint with an artist's airbrush. The airbrush used was an Aztec A4709. The nozzle used to apply the paint was a 0.30 mm general purpose acrylic paint nozzle. Different painting nozzle designs were tested, but the 0.30 mm nozzle was found to create the most uniform, dispersed, non-

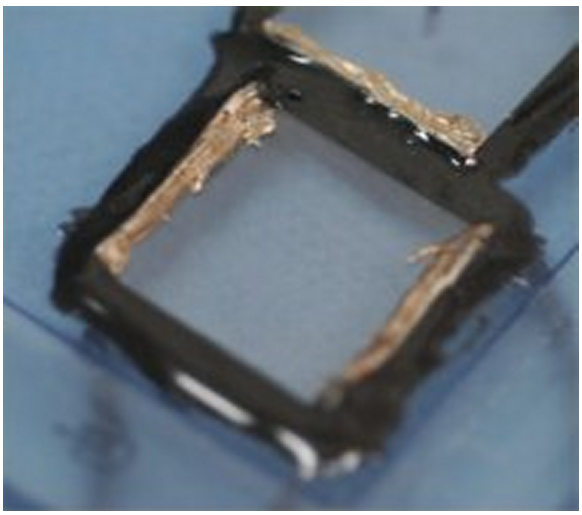

Figure 3.15: Picture of a transparent die with lead wires attached

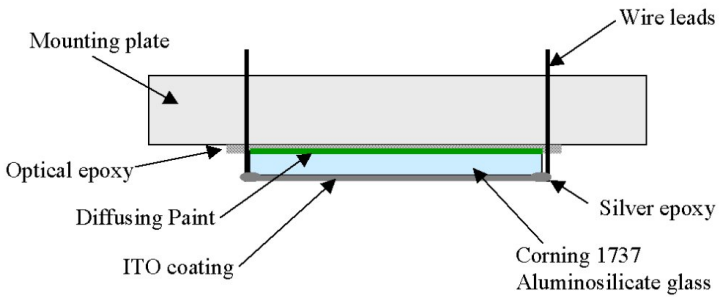

Figure 3.16: Die mounting set-up for visualization stand

granular layer which was required to achieve a uniform scattering of light [50]. The paint used was Liquitex concentrated acrylic paint, medium viscosity. The color of the paint was Titanium White. The paint was diluted by mixing 1 : 1 with filtered water. When applying the paint, the line pressure was set to 30 psig. The regulator on the airbrush was adjusted so that paint would come out of the nozzle when the trigger was pressed fully down in the full forward position. For application of paint on the dies, the trigger was pressed half way down at two-thirds of the forward position. Experimentation is required in order to obtain an adequate diffusing surface. Glass microscope slides were used as practice to find the right settings of the airbrush.

The dies were secured to a mounting surface using a UV-curing optical epoxy. The UV epoxy was a one-part composition, so no mixing was required. This reduced the number of microscopic bubbles in the mixture and improved the optical quality. The epoxy is also nearly completely optically transparent. Nothing is completely transparent due to absorption at certain wavelengths and reflectance at interfaces. This epoxy is chosen in bonding lenses and mirrors because of its superior optical clarity, but to say that it is completely transparent would be inaccurate. This process does not depend of the intensity of the light relative to the intensity emitted by the laser or to any reference intensity, so a small amount of light reflected or absorbed is not of consequence; there is no error in measurement associated with it.

The epoxy also creates a seal so that fluid cannot seep under the dies and distort the image. The epoxy, Norland Optical Adhesive 68, was chosen for its ability to bond well to both glass and plastics such as acrylic and polycarbonate. Also, this epoxy has a viscosity $\mu = 0.5\,[kg/m - s]$, which was higher than many of the alternative choices of epoxies. The higher viscosity epoxy was found to work better for attaching the dies to the plastic mounting plate without trapping air. To secure the dies to the backing plate, 25 small drops of the epoxy were distributed in the area that the die was to be mounted, as shown in Figure 3.17. This distribution of epoxy was found to minimize the amount of air that was trapped under the die. After the epoxy was applied to the backer plate, the die was placed painted side down and pressed into place with a hand-held vacuum tool that allowed for handling of the die with-out touching the die with the hands or fingers. A small amount of force was required to overcome the viscous force of the epoxy as it spreads beneath the die. If any air became trapped under the die, the vacuum tool was used to force it out by applying force near the bubble, pushing it outward.

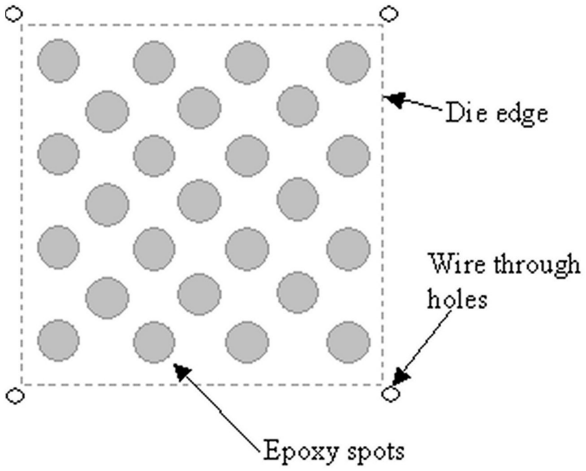

Figure 3.17: Location of epoxy spots

The epoxy was set using a UV curing lamp from ThorLabs Inc. The lamp was a model UV 75 light with an intensity of 40 mW/cm^2 over the wavelength range of $300 - 425$ nm. To cure the epoxy, the fiber-optic tip of the lamp was held 1 cm from the die surface and slowly moved over the surface for 60 seconds. After 60 seconds, the die was checked to see if it had set. If not, the process was repeated until the die was secured in place. The die was determined to be secure if it would not move when a lateral force was applied with a pair of tweezers. After the epoxy was cured, it was allowed to set for a week before it was used in testing. The UV light was applied to the die through the glass die, as opposed to through the polycarbonate mounting plate. This option was found to require less time to cure because the polycarbonate has a high absorbtion of UV light. The diffusing layer of paint on the glass reflects approximately half of the UV energy but this is still far less energy than the polycarbonate would absorb. A picture of a die painted and mounted is shown in Figure 3.18.

The complete test section consisted of 4 transparent die assemblies on a 4 mm (5/32") thick polycarbonate mounting plate. The dies were cooled by spray nozzles that atomized the fluid and projected the spray upward (against gravity) onto the die surface. The spray

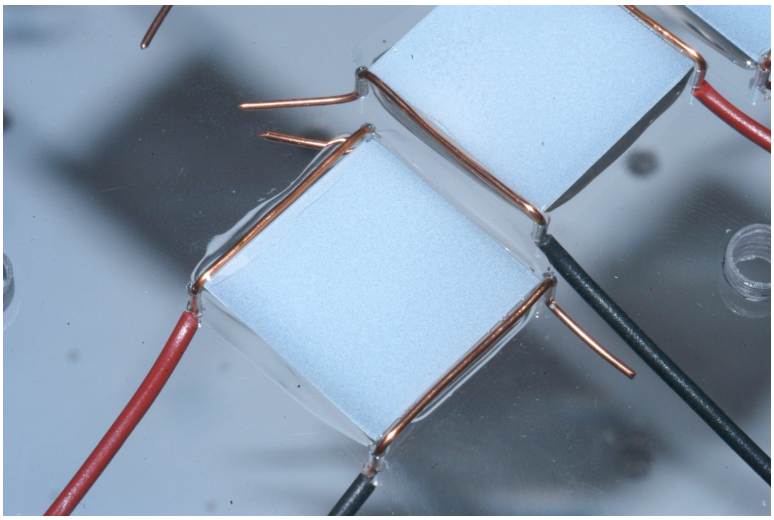

Figure 3.18: ITO test die for film thickness measurements

nozzles were housed in a stainless steel spray plate that was mounted inside of a stainless steel spray cap, as described in the Section 3.1.1. The spray cap was sealed to the test section with a Viton O-ring. Figure 3.19 shows the spray cap and spray plate with and with-out the visual test section. Each spray plate contained two different sets of spray nozzles. The atomizers used to produce the spray were pressure swirl atomizers with two inlet slots per nozzle orifice. Center jets were present to produce a full cone spray. The nozzles are further described in Section 3.1.1. Two sets of spray plates were used with different atomizer designs, designated Design 0 and Design 10. Design 0 had a nominal total flow rate of 0.583 ml/s (four type-A and four type-B nozzle arrays) at a pressure differential of 25 psid. The exit orifice was 292 μm in diameter. The nominal half cone angle was 42.5^o. Design 10 had a nominal flow rate of 0.507 ml/s and an exit orifice of 173 μm . Both designs had typical droplet diameters of 45-75 μm and velocities of up to 10 m/s, according to the manufacturer's specifications.

A schematic of the test set-up in shown in Figure 3.20. The working fluid was pumped from a reservoir by a peristaltic pump through a pulse dampener and a filter. The pump was a Cole-Parmer Masterflex with a variable speed DC motor. The pump head was a

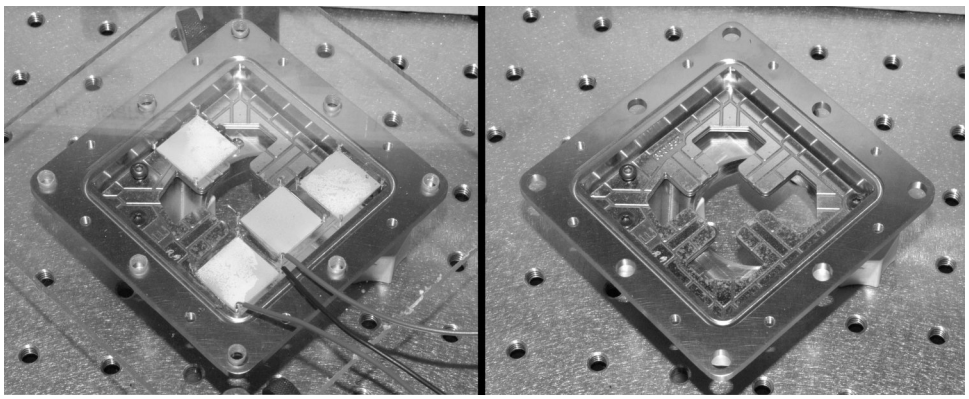

Figure 3.19: Spray cap and plate with and with-out visualization test section

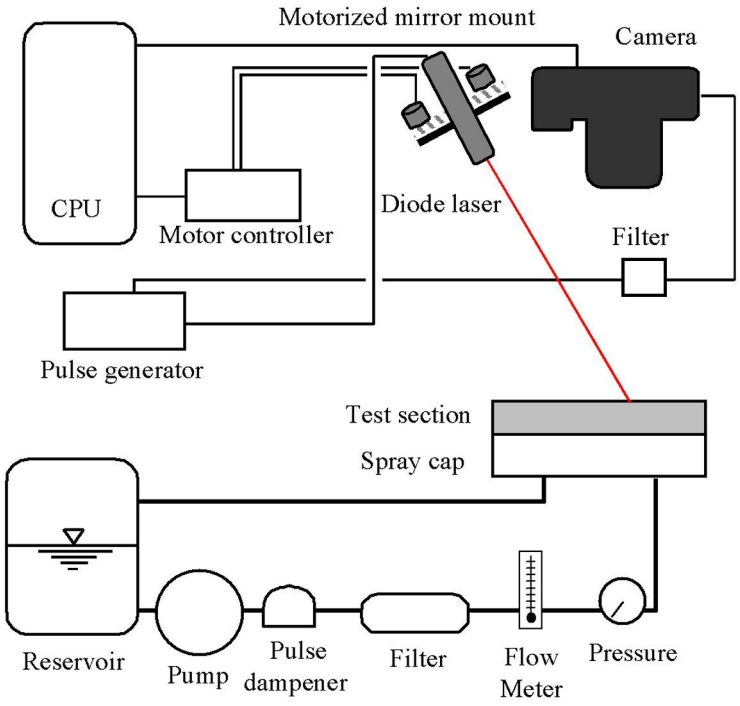

Figure 3.20: Schematic of the visualization test stand

Masterflex Easyload II. The filter served to remove particles as well as to further dampen the flow fluctuations from the pump. The test stand had a flow meter and a pressure gauge to measure the volumetric flow rate and pressure of the fluid. The flow rate was measured with a Cole-Parmer 200-3000 CCM flow meter with a flow adjustment knob. Pressure was measured with a Wika 0-30 psi pressure gauge. The fluid was fed into the spray cap and through the nozzles where it was atomized and sprayed onto the test section. To help prevent flooding of the spray cap, which hampers the cooling capability of SCPC, the nozzles were orientated so that the droplets were projected upwards and draining was gravity-assisted. The fluid drained from the cap back into the reservoir. The tests reported in this study were run adiabatically.

For this work, pure ethyl alcohol (200 proof) was chosen as the working fluid. The reason that FC-72 was not chosen as the test fluid is that it requires a complicated containment

stand that was not available at the time of testing. Since the test loop was open, the FC-72 would absorb a large amount of gas and would evaporate over-night. Ethyl alcohol also will evaporate, but at a much slower rate. It also has no gas solubility, is inexpensive, has better material compatibility and is easily available. Its surface tension and viscosity are similar to FC-72, so the spray that will be produced will be similar. Ethyl alcohol also has well-known physical properties. The presence of hydrogen in the test fluid was not of concern for this test because the spray was not interacting with a computer die. The glass dies are not susceptible to hydrogen penetration. The thermal test dies were susceptible to hydrogen penetration, so ethyl alcohol could not be used for the heat transfer tests. The differential test pressures across the nozzles were set at 15 or 25 psid. The low-pressure side was maintained at atmospheric pressure.

The laser used as the source of light was a Lasiris 635 nm 3.5 mW diode laser with focusing optics chosen to obtain a small point of light on the test surface. A smaller light source gives a higher contrast in the light ring, making it easier to find the diameter or the ring related to the total internal reflectance. The laser could be pulsed at a rate of up to 10 kHz using an externally supplied pulse signal. The laser pulse length is more controllable than the camera's manual shutter so a single pulse of light was used to control the exposure. It has been observed experimentally that the optical disturbance related to the droplet impacts are not significant when using the Fresnel Diffraction technique [41]. With a high frequency of droplet impact, the disturbances to the film can be averaged out by using a longer laser pulse. The laser was synchronized to the camera using the hot-shoe flash output. The signal from the hot-shoe was cleaned using an electronic filter and sent to a digital delay generator (Berkeley Nucleonics Corp. Model 555-4). The digital delay generator was set to generate a signal for 80 ms after the signal was received from the camera. The aperture of the camera was set to f-4.3, the lowest f-stop setting possible for the lens system used, and the shutter speed was set to 60. The camera used for testing was a Nikon D100 6 megapixel camera with

a 60 mm fixed focal length Nikon MicroNikor lens. The laser was mounted with a collar into a 1" motorized mirror mount, pictured in Figure 3.21. A New Focus Intelligent Picomotor system was used. Picomotor actuators were used to control 2 axes of the optical mount. The mirror mount allowed computer control of the laser spot location for precise positioning and enabled a fully automated testing process. The actuators on the mirror mount were controlled through a New Focus Model 8753 motor controller that was connected to a New Focus Model 8750 network controller. This allowed for communication with the CPU via the serial port. A picture of the camera, test cap, and laser is shown in Figure 3.22.

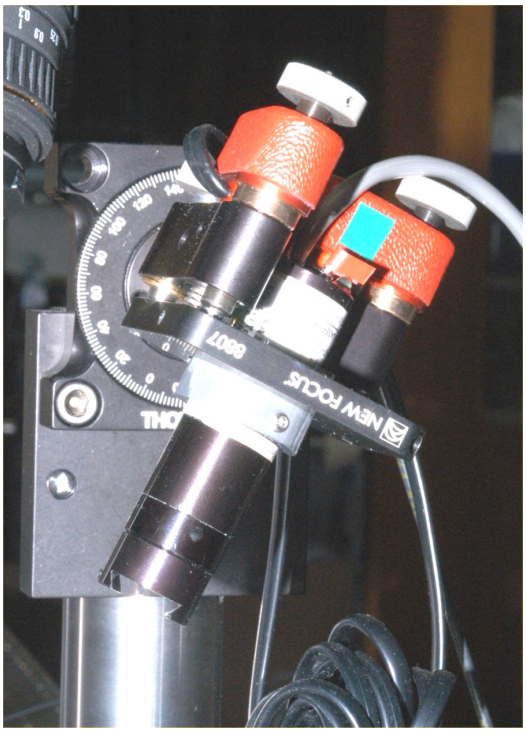

Figure 3.21: Picture of the motorized mirror mount used to control laser positioning and laser used for testing

Figure 3.22: Picture of film thickness stand showing the camera, laser, and spray cap

3.2 Experimental Procedure

3.2.1 Heat Transfer Stand

The desired pressure difference across the spray cap was set by adjusting the speed of the pump. The power supplies were then adjusted such that the desired starting power level was set. The fluid was heated from room temperature to $26^o\ C$. A fluid testing temperature of $26^o\ C$ was chosen so that at 1 atm system absolute pressure (P_{res}) there would be approximately 30 degrees of subcooling. The speeds of the heat exchanger fans were adjusted to maintain the fluid temperature. The dies were held at the starting power level for 30 seconds to ensure that critical heat flux had not been reached. It was found by observation that if the system was at steady state with respect to mass flow rate, system absolute pressure and fluid temperature then any transition to liquid film boiling would occur within 20 seconds. It was also noted by observation that it took 1 second for the die temperatures to reflect a

change in power and 3 to 5 seconds for the temperatures to stabilize. After a data point was recorded, the die power would be increased by 5 Watts. When transition to liquid film boiling occurred, the power level was lowered by 10 Watts and the testing was resumed using a 1 Watt power increments to give a more accurate indication of the critical heat flux. Critical heat flux was defined as the highest heat flux that could be maintained with a stable surface temperature. When CHF is reached, the surface temperature will rise quickly as the system transitions to liquid film boiling. Testing was done at pressure differentials between 5 and 45 psid. These test pressures correspond to a volumetric flow rate range of 1.75 mL/s to 4.80 mL/s per test die for nozzle design 0B and 0.35 mL/s to 1.06 mL/s per test die for design 0A. Testing pressures were limited by the working range of the pressure transducer at the upper end and by the performance characteristics of the spray nozzles at the lower end. For the pressure-swirl atomizers to work properly and create an evenly distributed flow pattern, there had to be at least a 5 psid pressure differential across them. A complete guide to running a test is given in the appendix.

3.2.2 Spray Visualization Stand

Measurements of the film thickness were taken using the spray visualization stand. The visual MCM used was coated with the diffusing paint. The nozzle design being investigated was mounted in the spray cap and the spray cap was mounted to the MCM. The camera was positioned over the die of interest and focused on the diffuse paint. The adjustment screws of the motorized mirror mount were centered, and the laser was pointed to the center of the die, location 3 in Figure 3.23. The mirror mount screws were centered to minimize the non-linear movement at when the adjustment screws are not near the centered position.

It was determined experimentally that images of the light ring could not easily be obtained when the camera was mounted perpendicular to the test dies. The glare from the laser spot

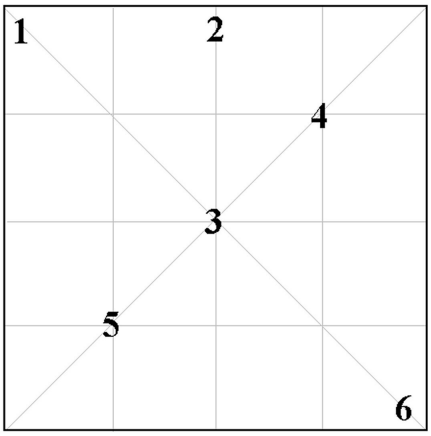

Figure 3.23: Locations of the measurements for film thickness

and the amount of light reflected directly back into the camera degraded image quality. By mounting the camera at an angle with respect to the perpendicular plane of the die, better images of the ring could be observed. However, the non-perpendicular viewing angle generated images with a slight trapezoidal distortion. Thus, the images do not have a uniform scaling factor at all points. Because of this, two scaling measurements are needed to calibrate the image. A scaling reticle was placed near the top of the camera's field of view and a picture was taken. Another picture was taken with the reticle at the bottom of the picture. These two images were analyzed to find a scaling factor for each. Then, a linear regression was performed between the two to give a scaling equation that applied to the entire image as a function of the position of the light ring in the y-plane of the image.

The pump was turned on at a low speed and adjusted to obtain the desired test pressure. Two pressures were used, 15 and 25 psi. The flow rate and test pressure were measured with the instruments described in Section 3.1.2. The program Nikon Control 3.5.0 was used to acquire images in a batch process. The laser was synchronized with the camera, and the length of the laser pulse was adjusted to obtain a good exposure. Film thickness measurements were attempted at 6 locations per die, as indicated in Figure 3.23. These

locations were combined into 4 groups: center, inside, edge and corner. At each test location, measurements of the resulting light ring radius were attempted in 8 angular directions. The directional names were designated N, E, S, W, NE, SE, SW, and NE, based on compass directions, with N representing the top of the image. Due to the size of the ring and the sampling locations, not all measurements could be made at every location. For example, NW, N, and NE measurements could not be made at location 2 due to its proximity to the top of the die.

The images taken during testing were post-processed. Post processing was done with Nikon Capture Editor 3.5, a software program that allows for histogram curve adjustments for each of the three color planes: red, green, and blue. In the images, the blue plane was eliminated. The green plane was unaltered at high intensities but attenuated at lower intensities. For the red plane, the higher intensities were removed in order to eliminate the glare related to the laser spot. With the blue plane and higher intensities of red filtered out of the image, a green spot remains at the location of the incident laser light that could be used to determine the center point from which to measure the light ring radius. The lower level intensities of red were also filtered out to make the red light ring, which came across at a medium intensity, more obvious. The radii were measured in pixels between the center of the laser spot and the center of the light ring. The location of the laser point was also recorded and used to find the scaling factor needed to convert the radii from pixel values to millimeters.

Chapter 4

Experimental Results

Results presented in this document are from tests conducted between October of 2002 and January of 2004. All experiments were performed at the University of Wisconsin-Madison in the Multiphase Flow Visualization and Analysis Laboratory (MFVAL) by the author or by an undergraduate research assistant under the supervision of the author.

In this section, test results are often presented as a function of the test pressure (ΔP_{cap}) instead of the flow rate. The test pressure was easier to measure, and it was decided to use it as a standard instead of the flow rate per die because of large differences in the flow rates of some of the nozzle designs. The flow rate of each nozzle design per die is given in Table 4.1.

The test pressure differentials chosen were 15, 25, 35, and 45 psi (103, 172, 241, and 310 kPa). 15 psi was chosen as the lower limit of testing pressures because it was possible that pressures below this would not create a high-quality spray. The nozzles used for testing were pressure swirl atomizers, and a certain amount of driving pressure is required to form a full solid cone. The high end of the test pressure was chosen to be 45 psi based on the limits of the system. The pressure transducer used to measure ΔP_{cap} was only capable of measuring 50 psid. Also, the quick disconnects used in the test stand were designed to double as pressure relief values. At pressures greater than 60 psig, they would uncouple. Finally, at high flow rates for some nozzle designs, the Vicor power supplies reached their maximum power levels. Testing at higher flow rates in these cases would not have allowed critical heat flux to be reached. Table 4.1 shows that the flow rates per die ranged from 0.12 to 4.83 mL/s.

Flow rate per die $[mL/s]$				
Nozzle design	Test pressure $[psid]$			
	15	25	35	45
0A	0.67	0.86	1.01	1.13
0B	2.87	3.65	4.32	4.83
1A	0.38	0.48	0.55	0.60
1B	2.13	2.69	3.12	3.40
10A	0.45	0.54	0.65	0.73
10B	2.09	2.54	3.06	3.43
11A	0.12	0.15	0.17	0.19
11B	1.09	1.31	1.54	1.69
13A	0.39	0.48	0.56	0.63
13B	2.32	2.85	3.35	3.75

Table 4.1: Flow rates per die in mL/s for nozzle designs at different test pressures

4.1 Heat Transfer

4.1.1 Critical Heat Flux

A commonly cited performance characteristic of a nozzle design is the critical heat flux. This was found experimentally by raising the power levels of the thermal dies slowly until a temperature instability developed in the film. This instability is indicated by a rapid rise in the surface temperature corresponding to the transition to the liquid film boiling regime. Measurements of the CHF were made at four test pressure differences corresponding to four flow rates for each of the ten nozzle array designs. These values are given in Table 4.2. Values of CHF as high as 77.8 W/cm^2 were measured.

Critical heat flux is not necessarily the best standard on which to compare nozzle designs; some designs are not intended to remove large amounts of heat, they are designed to match the amount of fluid used to the heat load. Figure 4.1 relates the CHF of nozzle designs 0A and 0B to the flow rate that was applied per die. Recall that 0A is a single nozzle design whereas 0B is a four-nozzle array, as discussed in Section 3.1.1. Nozzle 0A was not able to

CHF $[W/cm^2]$				
	Test pressure $[psid]$			
Nozzle design	15	25	35	45
0A	20.0	23.7	27.4	30.0
0B	55.8	66.2	73.4	77.8
1A	14.0	15.9	15.9	17.4
1B	33.7	40.9	44.8	49.0
10A	15.3	20.4	25.2	29.4
10B	33.0	37.0	47.1	45.9
11A	8.6	9.7	10.8	11.9
11B	27.3	30.3	32.6	34.0
13A	15.9	17.0	17.8	18.1
13B	44.2	52.1	57.2	61.0

Table 4.2: Critical heat flux values for nozzle designs

remove as high of a heat load, but it used far less fluid than design 0B does. If the trend shown by design 0A were to continue to higher power levels then the same amount of fluid would remove significantly more heat than design 0B. For design 0B the derivative of CHF with respect to flow rate is lower than design 0A and appears to be decreasing at increased flow rates. This implies that this design is reaching its limits in cooling capacity. Adding more fluid, beyond a certain point, will not increase the CHF due to flow stagnation at the center of the die. An explanation for this is given in Chapter 5.

4.1.2 Cooling Effectiveness

An unbiased parameter that accounts for the varying amounts of flow used for each nozzle design is the cooling effectiveness (ε) given in Equation 4.1, where A is the die surface area, Q is the volumetric flow rate, and q'' is the heat flux. The units of the parameter simplify to J/ml. Knowing this characteristic value for a set of possible nozzles allows for selection of a design with the correct cooling capacity for a specific application. The maximum cooling effectiveness occurs when the design operates at the CHF and therefor this was used as the

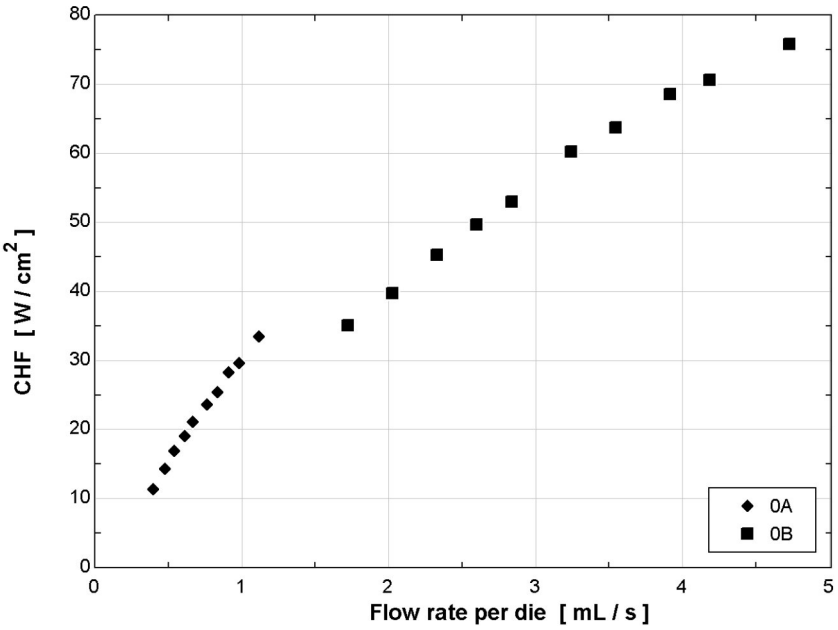

Figure 4.1: Critical heat flux versus flow rate

heat flux (q'') when calculating ε. Because of this, a factor of safety should be included to allow the die's surface temperature to remain at a safe operating level when selecting a nozzle design for an application. Values of ε for the nozzle array designs tested are given in Table 4.3.

$$\varepsilon = \frac{q''A}{Q} \qquad \left[\frac{J}{ml}\right] \tag{4.1}$$

Select information from Table 4.3 is shown graphically in Figure 4.2; the squares are data points from design 0B, and the diamonds are data points from design 0A. The trend for 0B is a constantly decreasing ε with increasing flow rates. There is no optimum point where the heat removed per milliliter of fluid added is at a maximum. Lower flow rates perform better by this standard, but lower flow rates give lower CHF than high flow designs. The CHF

ε $[J/ml]$ at CHF				
	Test pressure $[psid]$			
Nozzle design	15	25	35	45
0A	66.8	62.4	60.8	59.74
0B	43.7	41.2	38.9	36.8
1A	84.3	75.4	65.2	65.2
1B	35.7	33.3	32.3	33.1
10A	76.7	84.7	87.0	90.1
10B	36.0	32.3	31.1	30.4
11A	159.4	149.7	142.5	142.5
11B	56.5	50.6	47.8	45.3
13A	91.5	79.9	70.9	64.6
13B	42.9	41.0	38.8	36.7

Table 4.3: Fluid effectiveness values at CHF for nozzle designs

does not increase linearly with increased flow rate. If this were true, than the data points would lie on a horizontal line in Figure 4.2. Additional fluid does still remove additional heat, but it also causes CHF to occur relatively sooner. This is likely due to interactions of the multiple nozzles in the center region of the die, as discussed in Chapter 5.

The single nozzle exhibits a different behavior. In Figure 4.2, nozzle design 0A is shown by the diamonds. The figure shows that this design has an optimum operating flow rate. There is a maximum point where the fluid is able to remove more heat per unit area of flow rate than other flow rates can. After this maximum point, the curve decreases, so additional fluid does not remove heat as effectively. This figure is a useful way to match the nozzle performance to a specific intended heat load. When designing system components, such as pump size, reservoir size, and tube diameter, this figure provides a quick reference to estimate the flow rate that will be required for a given heat load.

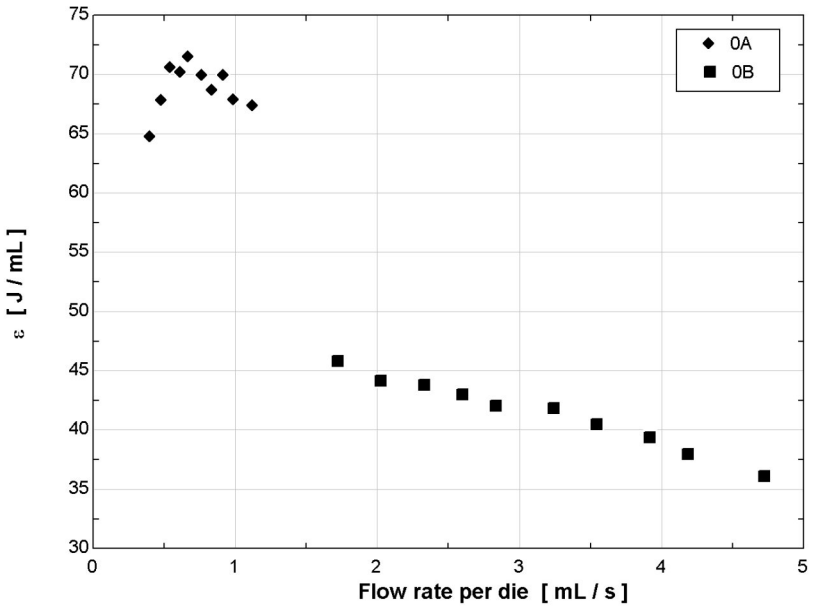

Figure 4.2: Cooling effectiveness at CHF versus flow rate

4.1.3 Cooling Efficiency

The effects of subcooling the fluid on the system performance is not well understood. Also, the amount of evaporation that takes place in the film during spray cooling is largely unknown or misunderstood. To take into effect these two parameters, a dimensionless efficiency value was developed to characterize nozzle designs. The efficiency, shown in Equation 4.2, is a ratio of the heat load removed to the total heat capacity of the fluid, including warming the fluid from a sub-cooled state to saturation and to fully vaporize it. In the equation, c_p is the liquid specific heat, ΔT_{sat} is the level of subcooling, and h_{fg} is the heat of vaporization. A value of $\eta = 1$ corresponds to a fluid packet completely evaporating from the surface, the theoretical upper bound of η assuming that all heat is removed from the surface by the fluid. This inclusively assumes that conduction through the die and radiative heat transfer are negligible compared to the rate of heat removal by the fluid.

$$\eta = \frac{q'' \ A}{Q \ \rho_f \ (c_p \ \Delta T_{sat} + h_{fg})} \tag{4.2}$$

The values of η obtained at CHF (η_{max}) in the experiments are shown in Table 4.4. The values range from 0.209 to 0.755. Nozzle design 11A had significantly higher values of η than any of the other designs, meaning that much more of the fluid delivered to the surface underwent a phase change. All of the tests run in this study attempted to maintain the same level of subcooling ΔT_{sat}. The fluid could not undergo a phase change until this subcooling was overcome. The value of η required for this to occur ($\eta_{1\phi}$) is given in Equation 4.3, the efficiency of a single-phase system.

$$\eta_{1\phi} = \frac{Q \ \rho_f \ c_p \ \Delta T_{sat}}{Q \ \rho_f \ (c_p \ \Delta T_{sat} + h_{fg})} \tag{4.3}$$

For the tests run, it was found that $\eta_{1\phi} \approx 0.20 - 0.28$. A plot of the efficiency at critical heat flux versus the critical heat flux is given in Figure 4.3. The gray band represents the approximate range of η at which the single phase ends. Nozzle designs that rely less on

η at CHF				
	Test pressure $[psid]$			
Nozzle design	15	25	35	45
0A	0.324	0.305	0.297	0.291
0B	0.198	0.188	0.176	0.168
1A	0.401	0.359	0.311	0.306
1B	0.169	0.158	0.154	0.155
10A	0.361	0.400	0.414	0.426
10B	0.170	0.153	0.148	0.145
11A	0.755	0.707	0.680	0.683
11B	0.267	0.239	0.228	0.216
13A	0.439	0.384	0.340	0.309
13B	0.206	0.198	0.185	0.175

Table 4.4: Cooling efficiency values at CHF for nozzle designs

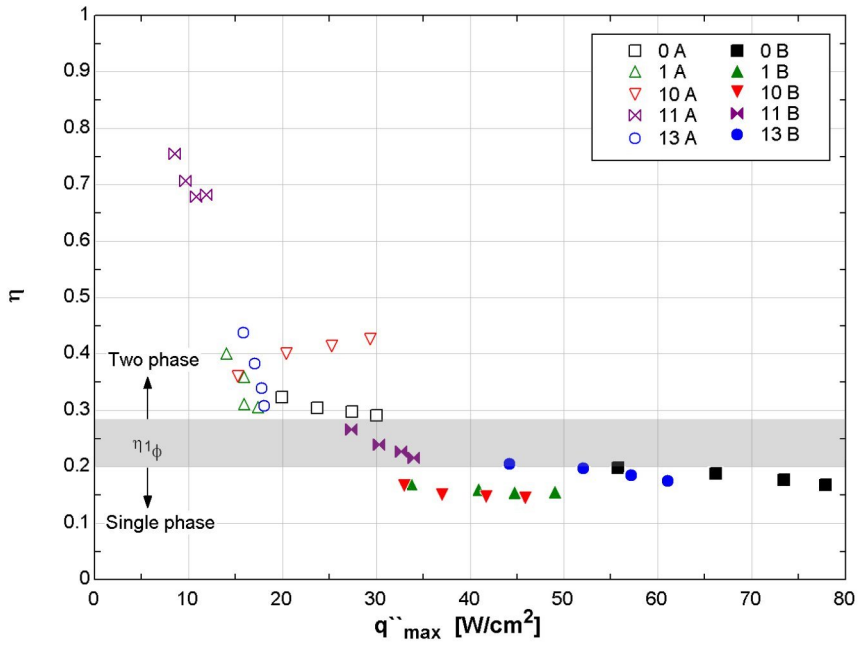

Figure 4.3: Efficiency versus CHF for all nozzle designs

multi-phase heat transfer are seen to obtain higher values of CHF. Some of the B nozzle designs in fact do not reach $\eta = \eta_{1\phi}$ before reaching CHF. This is likely because η is based on an average of the entire die and not local values. In the multi-nozzle arrays, as all of the B nozzles designs are, there could exist a stagnation region in the film where the interaction of the flows from different nozzles traps the fluid in the center of the die. As the fluid outside of these stagnation regions is pushed off by incoming droplets, the fluid in the stagnation region locally undergoes a significant amount of phase change and reaches critical heat flux. If this is what is occurring, then a lower local heat transfer coefficient should be seen in the center locations of the B nozzle designs. The heat transfer coefficients are discussed in Section 4.1.4.

4.1.4 Heat Transfer Coefficient

Because temperature measurements were taken at 8 locations on the thermal test dies, a heat transfer coefficient distribution can be estimated spatially over the surface. These values were calculated using Equation 4.4.

$$h_i = \frac{q''}{T_i - T_{in}} \qquad \left[\frac{W}{cm^2 - K}\right] \tag{4.4}$$

This gives values of the overall heat transfer coefficient. A heat transfer coefficient for the thermal boundary layer of the film cannot be calculated at this time because the local film temperature is not yet known. Instead, the temperature of the incoming fluid droplets is used in the temperature difference [22]. To simplify the data analysis, the eight heat transfer coefficients were averaged into three groups: center, corner, and other. The locations of the temperature measurements on the die are given in Figure 4.4. The value for the center was calculated from location 8, the value for the corner was an average of locations 5,6, and 7, and the value for the other region was an average of locations 1, 2, 3, and 4. Each nozzle array was repeated four times per spray plate, so four of the eight test dies were cooled by each nozzle design. Therefore, the values of heat transfer coefficient were not only an average of the locations on the die but also an average of the four dies. The larger number of samples increases the statistical reliability of the calculations.

When the data for the heat transfer coefficients was analyzed, it was discovered that for the B nozzle designs, the highest heat transfer coefficients were always found at the corners of the dies. Since the B nozzle designs have a wider distribution of nozzles, there is a greater coverage of the entire die surface. This will be shown in Chapter 5. The fluid that is being pushed through the film does not heat up as much before it reaches the edge of the die as it would for a single nozzle array such as 0A. The B nozzle designs create a theoretical stagnation point in the inner area of die due to spray interactions. Evidence for

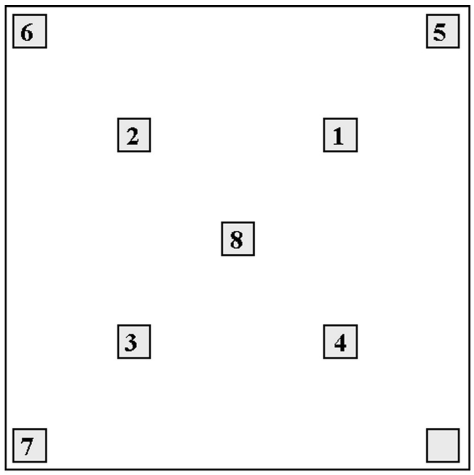

Figure 4.4: Locations of the temperature sensors of the thermal test die

this stagnation point is seen in Figure 4.5. Nozzle designs 0B and 13B fall on the right side of the graph, with CHF values greater than 50 W/cm^2. These designs consistently exhibit the lowest heat transfer coefficients in the center of the die. The remaining designs have the lowest heat transfer coefficients in the other region of the dies. In all cases, the heat transfer coefficient is the highest in the corners.

This trend is not seen in the A nozzle designs which show very little spatial distribution for some designs and more of a random patterning for others. Figure 4.6 shows that the center of the die often has the highest heat transfer coefficient, but it is not universally the best. The other regions tend to more often than not be the area of the die with the lowest heat transfer coefficient. This area is approximately inside the spray cone, when the highest droplet mass flux is reaching the surface, as will be discussed in Chapter 5. One area of interest on Figure 4.6 is nozzle design 11A, which appears on the left side of the figure. For this nozzle design, there is almost no spatial variation in the heat transfer coefficient, the entire die performs equally well. Figure 4.6 also shows that the heat transfer coefficient increases and the CHF increases, with a larger distribution of values found at higher critical heat fluxes.

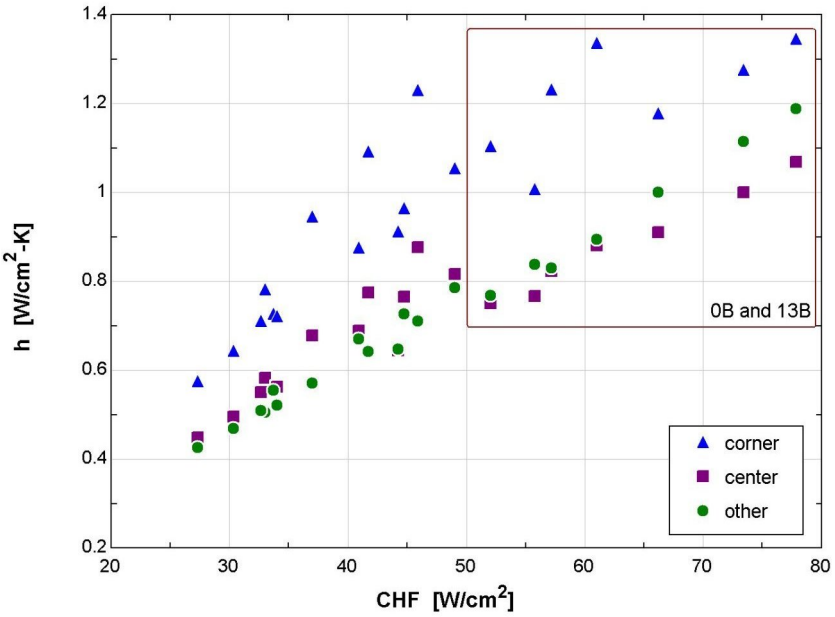

Figure 4.5: Heat transfer coefficient versus critical heat flux for B nozzle designs

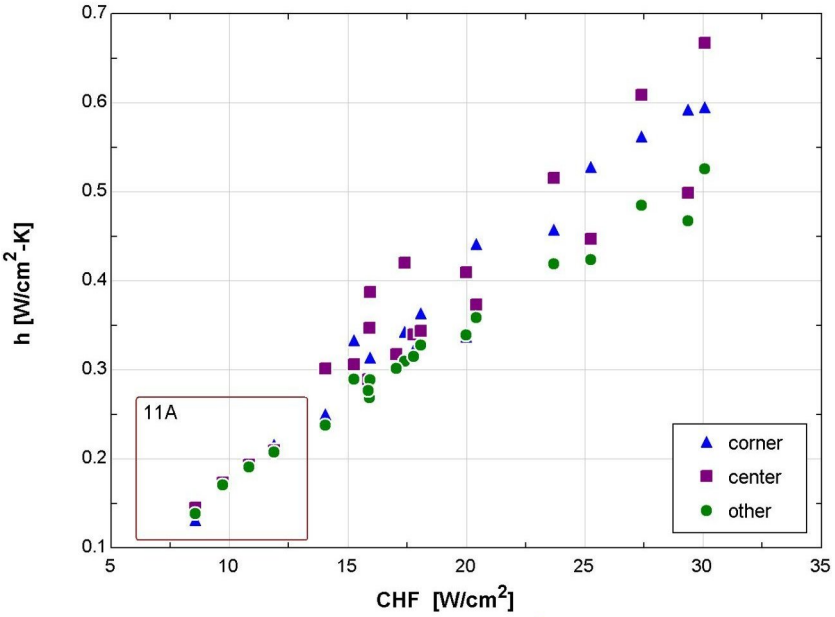

Figure 4.6: Heat transfer coefficient versus critical heat flux for A nozzle designs

To gain a better understanding of the role that the heat transfer coefficient plays on CHF, a plot of the local heat transfer coefficient versus efficiency is presented at the critical heat flux in Figure 4.7. The figure shows that, for B nozzle designs, the heat transfer coefficient sharply drops at a value of approximately $\eta = 0.2$. It was stated earlier that the efficiency value corresponding to the end of the single-phase regime ($\eta_{1\phi}$), was calculated by Equation 4.3 to be ≈ 0.25. Figure 4.7 demonstrates the differences in performance characteristics between nozzle designs that primarily use single-phase cooling versus those that rely on two-phase heat removal. There is clearly a difference in the behavior of the film for these two regions.

When the A nozzle designs were analyzed, a trend similar to that found in the B nozzle designs was discovered. Figure 4.8 is a graphical representation of the findings. It is seen that

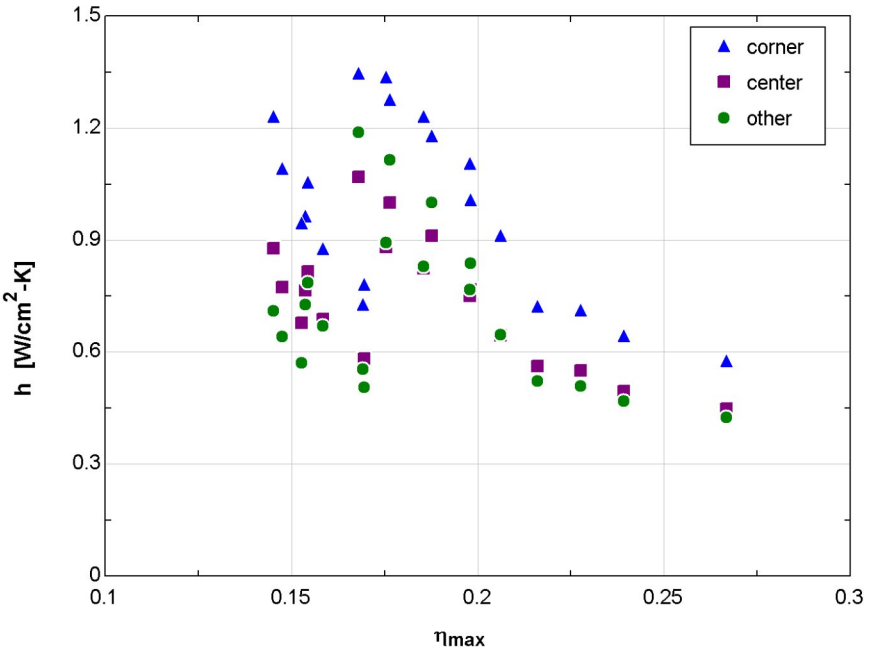

Figure 4.7: Heat transfer coefficient versus efficiency for B nozzle designs at critical heat flux

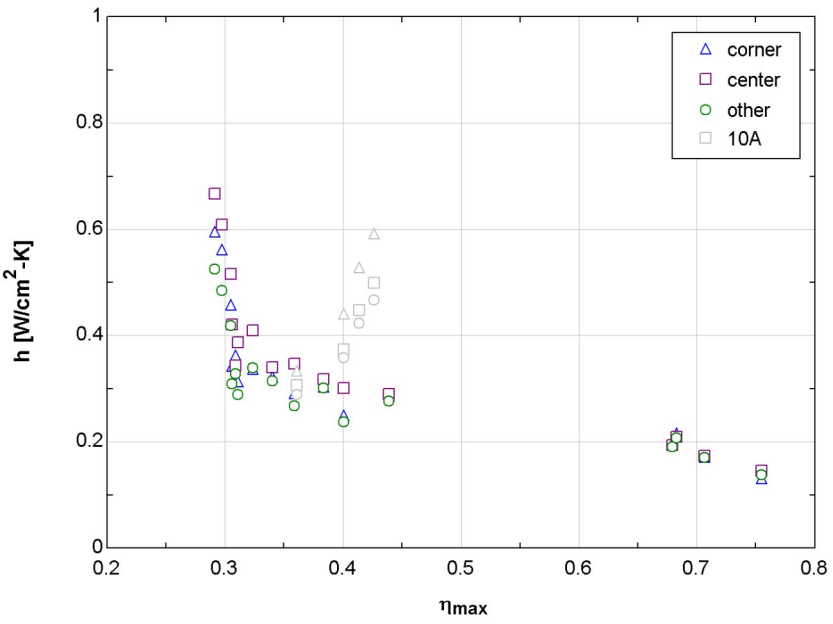

Figure 4.8: Heat transfer coefficient versus efficiency for A nozzle designs at critical heat flux

the heat transfer coefficient drops off sharply at $\eta = 0.3$. As the efficiency increases, the heat transfer coefficient continues to decrease. The anomaly in this data set is nozzle array design 10A (a 5-nozzle array). The same effect can be seen in Figure 4.3. All other designs have a decreasing trend but design 10A increases. These results show that the cooling mechanism for this design is again different than the other nozzle designs. This nozzle design is worthy of further investigation. If the trend continues, it shows great promise for removing very high heat loads because adding more fluid to it allows it to remove more heat from the surface where in other designs, less heat is removed.

Previous figures in this section have only shown the heat transfer coefficient at critical heat flux. In understanding the methods and reasons for CHF to occur, the heat transfer coefficient was studied at heat loads leading up to CHF. An example of this is shown in Figure 4.9. This figure shown the heat transfer coefficient versus heat flux for nozzle 0A

at a test pressure of 15 psid. In the figure, the heat transfer coefficient at the center is represented by the squares, at the corners by the triangles, and in the other regions by the circles. The figure clearly shows that the heat transfer coefficient for this designs was the highest at the center of the die. At the center and in the other region, the heat transfer coefficient increased as the heat load increases. This occurred initially for the corner regions, until approximately 17.5 W/cm^2. At this point, the heat transfer coefficient at the corner began to decrease. At the critical heat flux, it overtook the other regions as the poorest performance area with respect to the heat transfer coefficient. Experimentally, it was found that for nozzle 0A, CHF occurred at the corner of the die, the area that corresponds to the lowest heat transfer coefficient. The cause of this is the onset of nucleate boiling at the corners of the dies. Eventually, critical heat flux is reached in the corner. Since these values are averaged over three of the four corners on four thermal dies, the value does not drop

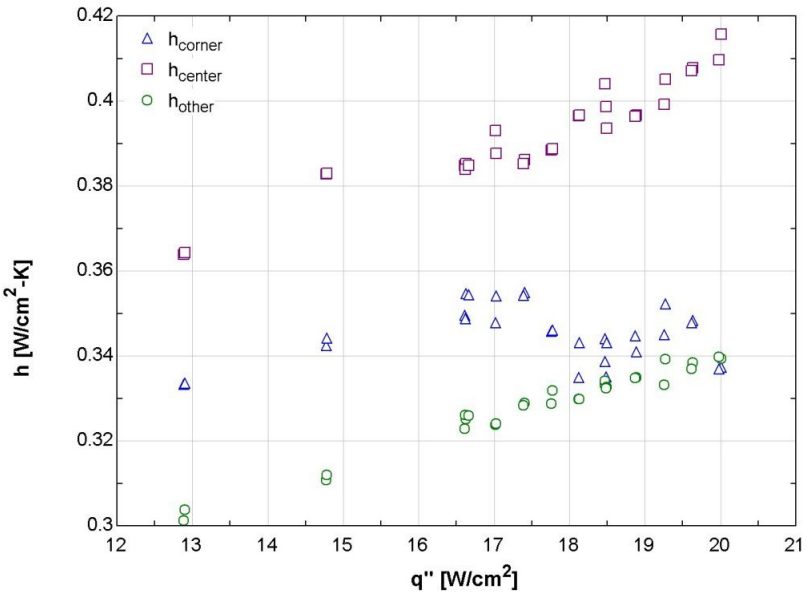

Figure 4.9: Heat transfer coefficient versus heat flux for nozzle design 0A at 15 psid

dramatically. If the individual corner at which CHF occurred was isolated and plotted alone, then the heat transfer coefficient would be even lower than the averaged value. As the test pressure is increased, the flow rate increases and the effect of CHF at the corner goes away.

A similar phenomena is seen in the center of the die when nozzle design 0B is run at 35 psid, as shown in Figure 4.10. The center has the lowest heat transfer characteristic throughout testing. All of the curves are slowly increasing with increasing heat flux until 70 W/cm^2 . At this heat load, the heat transfer coefficient at the center of the dies begins to decrease until CHF is reached. The change in the trend of the heat transfer coefficient is much more subtle for this design, and this trend is not seen in all of the test runs. Experimentally, it was found that the dies would reach CHF at the center with nozzle 0B. The reason for the poor performance at the center of the die may be due to the interaction of the nozzles in this region. This will be further discussed in Chapter 5.

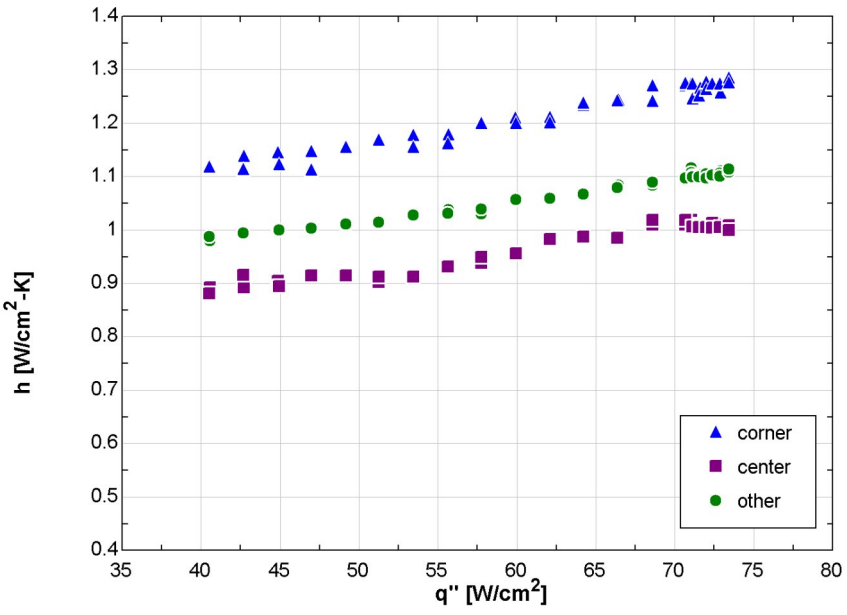

Figure 4.10: Heat transfer coefficient versus heat flux for nozzle design 0B at 35 psid

Figures 4.11 and 4.12 show the heat transfer coefficient versus the heat flux for all of the flow rates tested using nozzles 0A and 0B. In these figures, the average heat transfer coefficient is plotted instead of the three spatially averaged values. The average heat transfer coefficient is simply the average of the local heat transfer coefficient at the eight locations on the die. Two additional lines are shown on the figures as well. The black line with the solid squares is CHF for all tests at different flow rates. The black line with the solid diamonds is the point at which the average temperature of the die was measured to be $80^o\ C$. This temperature is the industry standard for the maximum junction temperature at which computer dies should be operated at while retaining reliability, as will be discussed in Section 4.1.5.

Figure 4.11 shows the results for nozzle design 0A. The figure shows that the average heat transfer coefficient for each test run has approximately the same trend with respect to CHF as the other test runs. The slope of all the lines are very nearly the same. The line representing CHF is also very linear for all test runs, as well as the $80^o\ C$ line. This makes the CHF very easy to model and predict for any given test pressure. Also, it is interesting that the distance between the $80^o\ C$ line and the CHF line remains the same for all tests. The two lines are parallel. This could be interpreted to mean that very little is changing in the behavior of the film as the heat load is increased.

Figure 4.12, which is a plot of the average heat transfer coefficient versus the heat flux for nozzle 0B, shows the same linearity for the CHF line and for the $80^o\ C$ line as the previous figure. However, the two lines are not parallel for this nozzle design. As the flow rate is increased, the CHF is increased faster than the $80^o\ C$ point in increased, and the distance between the two curves grows. It would seem that the behavior of the film that leads to CHF is suppressed at higher flow rates, demonstrated by the larger distance between the two curves. At higher flow rates, the surface temperature is able to be maintained without reaching CHF to a higher temperature. This may be due to the fact that the very high

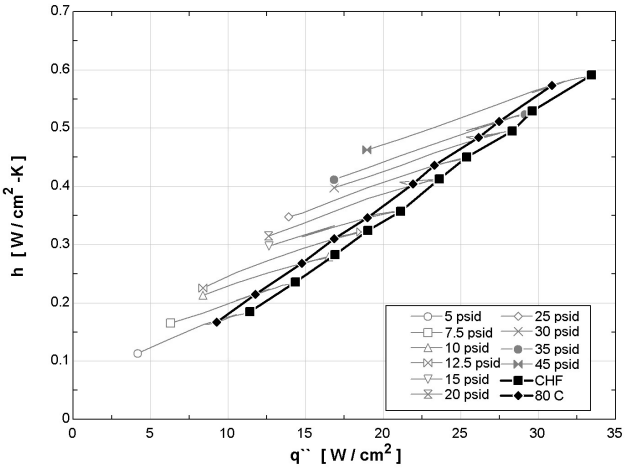

Figure 4.11: Heat transfer coefficient versus heat flux for 0A

number of droplets are impacting the film with a velocity and frequency high enough to suppress the surface nucleation or to remove nucleate bubbles that form before they are allowed to fully grow, thereby prolonging the onset of critical heat flux.

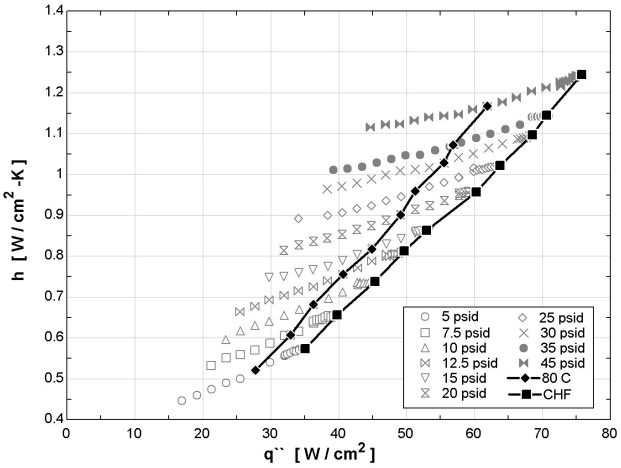

Figure 4.12: Heat heat transfer versus heat flux for 0B

4.1.5 Temperature Variation

The recommended maximum junction temperature for computer dies is $85^o\ C$ [51]. Above this temperature, the reliability of the dies will decrease significantly. In order to maintain signal integrity, the variation of temperature across the die must (ΔT_{die}) also be small though. If the die is hotter in one region than another, the signals and calculations will go at different speeds, which could lead to system crashes. Computer dies cannot be designed to disperse heat evenly across the entire surface, which will lead to some areas being hotter than others. Some spray cooling systems are designed to be able to predict which areas of the dies will be hotter than others and adjust the amount of fluid delivered to that area [30]. These designs are much more complex. The temperature variation across the die is an important consideration that must be made when designing a spray cooling system.

For the ten nozzle designs that were tested, the average temperature difference across the dies (ΔT_{die}) is plotted versus the CHF in Figures 4.13 and 4.14. Figure 4.13 represents the A nozzle designs. Four different flow rates are plotted for each of the five nozzle designs. The figure shows a wide range of ΔT_{die}'s for the different designs. It also shows a difference in behavior. For example, design 0A had a decreasing temperature variance across the die with increasing flow rates. The more fluid that was used for cooling, the more uniform the die temperature became. Design 1A shows the opposite effect.

Figure 4.14 represents the B nozzle designs. Again, four different flow rates are plotted for each of the five nozzle designs. For these designs, all of the curves are increasing with increasing flow rates. Additional fluid added to the film causes a larger temperature difference across the die. This occurs because the corners of the die, as discussed in Section 4.1.4, have high heat transfer coefficients than the center does. Additional fluid allows the corners to convect heat more efficiently, but the flow interference region at the center of the die performs worse. The center heats up to a critical temperature corresponding to critical heat flux while

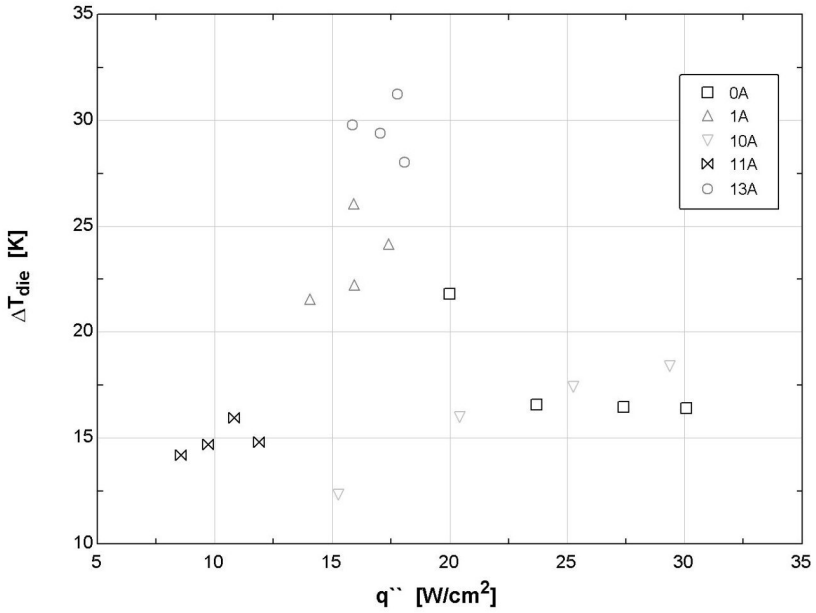

Figure 4.13: The average temperature difference across the dies versus critical heat flux for A nozzle designs

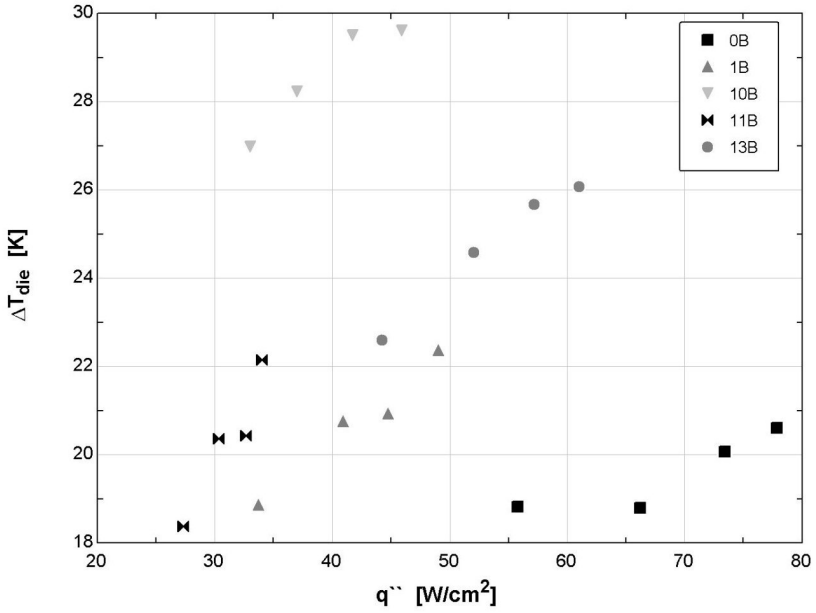

Figure 4.14: The average temperature difference across the dies versus critical heat flux for B nozzle designs

the corners remain well cooled, leading to a sometimes very large ΔT_{die}.

Since most designs will never reach critical heat flux, the temperature variation across the die was also studied at power levels less than critical. The results of this study for nozzle 0A is shown in Figure 4.15. This figure again shows that increasing the flow rate for the single nozzle design decreases the temperature variation across the die for a given heat load. The slope of the lines also changes drastically between the test cases at 15 psi test pressure and 45 psi test pressure. This indicates a difference in the behavior of the film, and a transition from a spray regime leading to large temperature variations across the surface to one with much smaller temperature variances. The figure shows that in order to reduce the temperature variation across the die, higher flow rates should be used for this nozzle design. This will lead to both a more uniform temperature and high available heat loads.

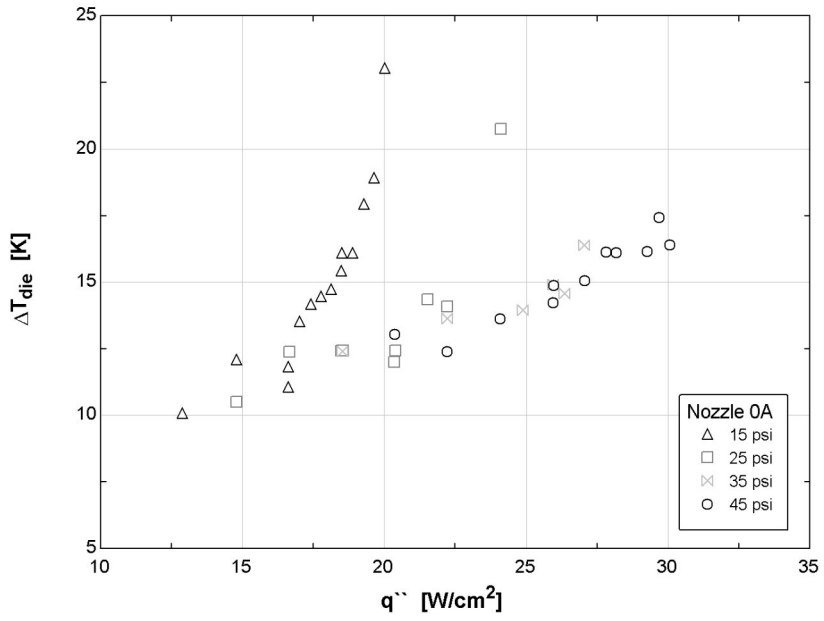

Figure 4.15: The average temperature difference across the dies versus heat flux for nozzle design 0A

Figure 4.16 is a plot of the temperature variation across the die versus the heat load for nozzle 0B at different test pressures. For this nozzle design, the slope of the trend lines remains the same for all four test cases. This indicates that the behavior of the film remains for the most part independent of the flow rate. The corners of the dies continue to be well cooled and maintain a low junction temperature while the center of the dies, in the spray interaction region, do not cool as well. However, with more droplets impacting the surface, critical heat flux is suppressed for a longer time in the center region and higher and higher junction temperatures can be achieved. It is seen that a higher flow rate will again lead to less of a temperature variance for this design. Increasing the heat load leads to very high ΔT_{die}'s.

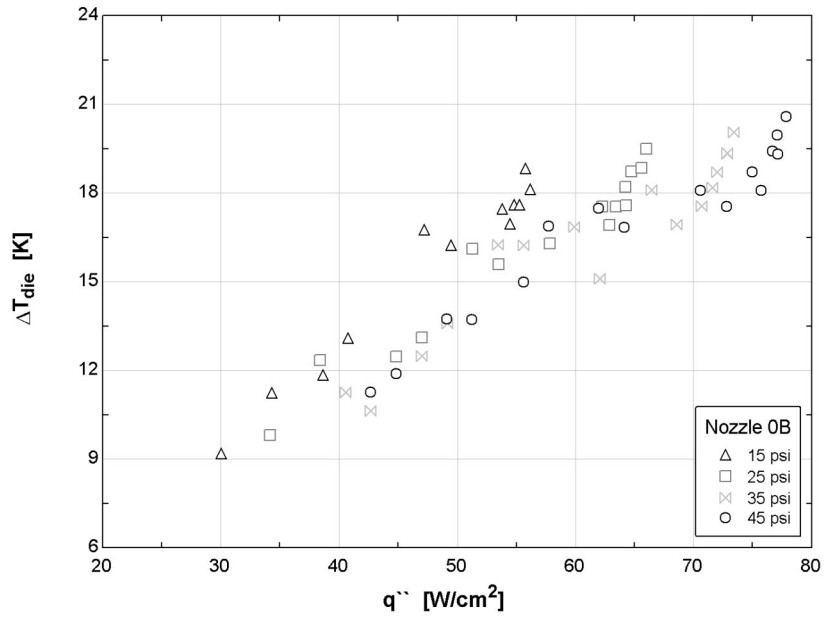

Figure 4.16: The average temperature difference across the dies versus heat flux for nozzle design 0B

4.2 Film Thickness

Measurements of the film thickness were taken at the six locations shown in Figure 3.23. These six locations were divided into four categories as follows: Corner = locations 1 and 6, Edge = location 2, Center = location 3, and Other = locations 4 and 5. For each of the two flow rates tested, 20 pictures were taken at each location. These images were input to a imaging script that adjusted the color planes and histogram plots to make the light ring more visible. The center of the light ring was found by finding the center of the dot were the incident laser light hit. This dot is very bright in all pictures and easy to locate. The center of this dot was assumed to be the center of the ring. An attempt was made to measure in pixels the radius of the ring in each of the 8 directions. The location of the center of the image was used to determine the scaling factor for the light ring. The radius of the light ring in pixels was multiplied by the scaling factor of μm per pixel to convert the radius to μm . The radii were averaged for each picture to find a mean radius assuming that the film is flat ($\phi = 0$). This mean radius was input to a program to find the film thickness based on input parameters, including the index of refraction of the glass, the liquid in the film, and thickness of the glass. The equations for this model are included in the appendix. This model is capable of taking the slope of the film into consideration.

Film thickness measurements were attempted for four of the nozzle designs, 0A, 0B, 10A, and 10B. A total of 406 light rings were measured for nozzle design 0A. An additional 111 light rings were measured for nozzle design 10A. Measurements of 82 light rings were made with nozzle design 10B. Measurements could not be made on design 0B. This may have been due to the high level of surface disturbances associated with this spray pattern, or it may have been due to improper set-up. Of the 599 total light ring images obtained, 454 of them were at locations 1, 2, and 4. Only 11 light rings were measured at location 3, but all 11 of these were found with design 10B. This may have been due to the high frequency of

droplet impact directly underneath the spray area is so high that the surface of the film is not smooth enough for the light ring to form. The fact that less light rings were found at locations 5 and 6 theoretically should correspond to locations 4 and 1 respectively. Since far fewer light rings could be located at these two points, it is assumed that the geometry of the test set-up was not as accommodating for measurements at these locations.

The number of images obtained (pics) and the calculated film thickness (δ) at each location for the nozzle designs 0A and 10A are given in Table 4.5. These film thickness values assume no slope to the film. The results are shown for the two test pressures. Film thicknesses could not be measured for locations where no images were obtained. Nozzle 0A was tested with two different visualization dies, die 3 and die 4. Each of the dies tested has a separate results column in the table. Table 4.5 shows that the film is the thickest at the corners of the dies and becomes thinner towards the center.

A contributing factor to the high values of film thickness calculated at the corners may be that the slope of the film is too great to be neglected. If the film thickens as it approaches the edge of the die, the angle ϕ will positively increase. This will result in an large radius of the light ring. When the slope is assumed to be flat and a large radius is input to the program, the model will output a film thickness that is too large. For Nozzle 0A with test

Location	Nozzle 0A-3				Nozzle 0A-4				Nozzle 10A			
	Test Pressure				Test Pressure				Test Pressure			
	15 psi		25 psi		15 psi		25 psi		15 psi		25 psi	
	pics	δ	pics	δ	pics	δ	pics	δ	pics	δ	pics	δ
1	20	918	20	712	29	367	24	307	7	386	6	154
2	22	279	22	230	32	173	27	65	29	156	27	104
3	0	–	0	–	0	–	0	–	0	–	0	–
4	40	67	40	42	10	47	14	46	7	46	7	54
5	33	93	21	64	0	–	0	–	3	118	0	–
6	28	207	24	155	0	–	0	–	3	466	22	335

Table 4.5: Film Thickness of 0A and 10A Nozzle designs in μm

die 3 (0A-3) at 15 psi test pressure and location 1, the light ring radius was measured to be 2864 μm . With a no-slope assumption, this gives a film thickness of 918 μm , as shown in Table 4.5. If the slope is assumed to be a positive value, such as 30^o, the film thickness is calculated to be 381 μm . This film thickness value, which corresponds to an assumption of a very large slope angle ϕ, is still thicker than the internal areas of the die. This implies that the die is becoming thicker as the fluid travels outward on the die. These values for film thickness measurements also assume that the effects of surface disturbance waves have been averaged out. As the droplets impact the film, small waves will propagate outward, changing the position of the light ring. The camera shutter and laser were set to capture a time-averaged image to account for this.

Table 4.6 shows the film thicknesses measured for nozzle design 10B. Far fewer images were obtained for this nozzle design. Possible reasons for the difficulty in finding measurable light rings in the images taken are the geometry of the set-up and the length of the laser pulse. The increase in the number of nozzles means a much higher frequency of droplet impacts, making it more difficult to capture light ring images. From the data that could be collected, it was found that the average film thickness of this nozzle design was much thinner than the other nozzle designs tested. Film thicknesses as small as 4 μm were measured at the corner and the center of the die at a test pressure of 15 psi. It is also shown in Table

Location	Nozzle 10B			
	Test Pressure			
	15 psi		25 psi	
	pics	δ	pics	δ
1	2	4	8	38
2	16	175	9	132
3	10	4	1	18
4	17	43	19	40.5
5	0	–	0	–
6	0	–	0	–

Table 4.6: Film Thickness of 10B Nozzle designs in μm

4.6 that the film is not always thinned as the flow rate increases for this nozzle design, as was true for the other two nozzle designs tested. The film was found to thicken in the two regions that had been the thinnest before and to thin in the areas were it had been thicker before.

It is challenging to determine the uncertainty of these film thickness measurements. Since the camera used had a resolution of 6 megapixels, there is little uncertainty introduced through the image capture. Picking the radius of the light ring from the image will introduce an uncertainty of approximately 5 pixels. The primary source of uncertainty comes from the waviness of the film. The non-uniformity of the surface due to droplet impact waves requires that the images be time averaged. With more images taken and the longer the exposure time, the confidence of the measurements increases. There is a substantial degree of uncertainty in these measurements since a limited number of images were obtained. Uncertainties in the measurements due to changes in the index of refraction in the glass and the film are small. The indexes of refraction are very well known and change very little over the temperature ranges that would be expected in spray cooling conditions.

Chapter 5

First-Order Film Thickness Modeling

In order to model the heat transfer characteristics of spray cooling, it is important to understand the behavior of the film. Experimental data is difficult to obtain, especially when nozzle flow rates and droplet coverages are changed. A computer model would allow for rapid evaluations of new nozzle designs. The first step in generating a working model is to verify its ability to predict the film thickness and film velocities in an adiabatic case. Although the behavior of the film present in spray cooling is governed by many complex factors, such as droplet impacts, boiling, shear at the wall, and turbulent mixing, it was hoped that a simple model could be used to obtain reasonable estimations for the film thickness. The simple model used is based on mass continuity, with the fluid in the film being driven by the momentum of the droplets impacting the surface and inhibited by the counter-acting force of the wall shear.

The inputs required by the model are the axial droplet velocity ($v_{d,z}$), the droplet volume flux distribution (Q''), and the geometry of the die and nozzles. Parker Hannifin Corp, the nozzle manufacturer, supplied a droplet size distribution, axial droplet velocity distribution, and the volumetric flow flux distribution for nozzle designs 0A and 0B. The data was taken with a Phase Doppler Particle Analyzer (PDPA). Spray characteristics were taken by the PDPA at distances of 6, 10, and 20 mm axially from the nozzle orifice. The results at 6 mm were used, since this is approximately the distance from the nozzle orifice to the test die that was used for testing. Using the 6 mm data, equations were developed to approximate the droplet diameter, volumetric flux, and velocity as a function of radius. Mass flow flux ($\dot{m}''$)

was found by multiplying the volumetric flow flux (Q") by the liquid density (ρ_f), assuming that the density remained constant. The equations generated for nozzle 0A are given in Eqn. 5.1, 5.2, and 5.3, where rad is the radial distance from the center of the die.

$$v_{d,z} = 10.2584 - 1.08929\ rad + 0.0275716\ rad^2 \quad for \quad rad < 14 \tag{5.1}$$

$$\dot{m}'' = \left[\frac{rad^2}{1.4}\ (rad - 5.8)\ (3 - rad)\right] /800 + 0.096 \quad for \quad rad < 5.652 \tag{5.2}$$

$$\dot{m}'' = \frac{1}{(rad - 2.8)^2} - 0.010628 \quad for \quad rad < 5.652 \tag{5.3}$$

The model was set-up assuming 1/4 symmetry. This assumption is valid for all of the nozzle designs except 11A and 13A. Using a 1/4 symmetry model greatly reduces the computational time, and it was determined that it was not worth expanding the model to accommodate two additional nozzle designs. The model was divided into 2500 nodes of equal size. A nodal mass balance is shown in Figure 5.1. At each of these nodes, a dynamic pressure (Δp_d) representing the momentum associated with the incoming droplets was calculated based on the mass flow flux and the droplet axial velocity, as shown in Equation 5.4. The term K_1 is a momentum conversion factor used to take into account that not all momentum in the droplet is transferred to the film. The momentum of the droplets should balance the shear force exerted by the wall onto the film. The shear from the wall is given by Equation 5.5, where τ is the shear force, μ is the liquid dynamic viscosity, and u is the velocity of the film in the x direction. A velocity distribution across the flow was assumed initially to calculate the shear. These equations were substituted into the mass continuity equation, Equation 5.6. In this equation, $\dot{m}''$ is the droplet mass flow flux, δ is the film thickness, and v is the velocity of the film in the y direction. This was simplified to an equation that could

be solved iteratively using linear matrix algebra, which is shown in Equation 5.7, where V is defined in Equation 5.8.

$$\Delta p_d = K_1 \ \dot{m}'' \ v_{d,z} \tag{5.4}$$

$$\tau = -\mu \frac{du}{dx} \tag{5.5}$$

$$\dot{m}'' = \rho_f \left[\frac{d}{dx}(u \ \delta) + \frac{d}{dy}(v \ \delta) \right] \tag{5.6}$$

$$-K_1 \frac{\dot{m}''}{\rho} \frac{du}{dz} = 2\delta \frac{d\delta}{dx} \frac{dV}{dx} + \delta^2 \frac{d^2V}{dx^2} + 2\delta \frac{d\delta}{dy} \frac{dV}{dy} + \delta^2 \frac{d^2V}{dy^2} \tag{5.7}$$

$$V = \Delta p_d \delta \tag{5.8}$$

The model requires values of density (ρ) and dynamic viscosity (μ) to calculate the mass droplet flux ($\dot{m}''$) and the shear at the wall (τ). In order to match the experimental results, which used 200 proof ethyl alcohol as the test fluid, the properties of ethyl alcohol were used

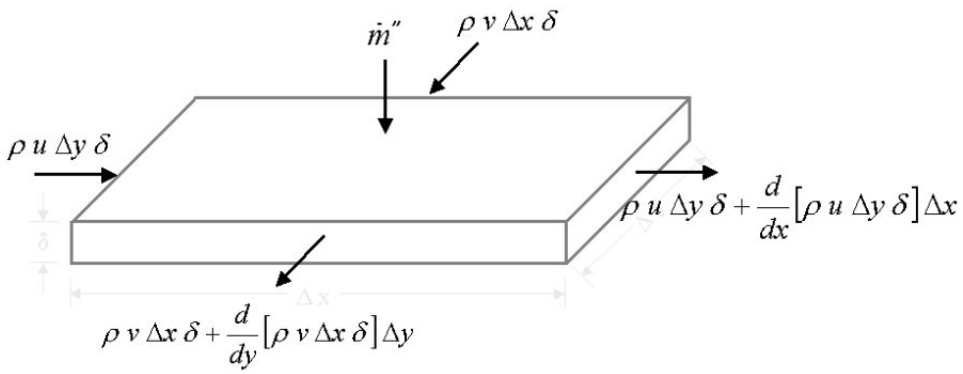

Figure 5.1: Differential control volume for film thickness model showing mass continuity relations

Property	*Ethyl Alcohol*
Appearance	Clear, colorless
Chemical formula	C_2H_6O
Average molecular weight	46.07
Boiling point $[^o\ C]$	78.5
Pour point $[^o\ C]$	-114.1
Liquid density $[kg/m^3]$	799
Dynamic viscosity $[kg/m-s]$	0.248×10^{-3}
Surface tension $[N/m]$	0.022

Table 5.1: Properties of ethyl alcohol at standard temperature and pressure

in the model. The properties that were assumed are given in Table 5.1. The assumption was made that the volumetric spray distribution was the same for both perfluorohexane and ethyl alcohol. The mass flux distribution was different based on the liquid density.

The results of the droplet mass flux distribution for nozzle designs 0A and 0B is shown in Figure 5.2. The image on the left depicts design 0A, a single solid cone spray, and clearly shows that the highest amount of fluid is carried at the outside radius of the spray cone. Inside in the center region, there is less mass delivered to the die. Outside the radius of the cone, there is very little flow at all. No additional cool fluid is added to the film, causing the film to raise in temperature as it reaches the edge of the die. The image on the right shows design 0B, a four-nozzle array. These are also full spray cone designs, but they cover a much larger area of the die due to their locations. A four-petal design appears resulting from the interactions of the droplets from neighboring nozzles. In these areas, which appear white in the image, droplets are colliding head-on with other droplets, losing some of their momentum. In the center of the die, all four nozzles are interacting. It is likely that a stagnation region would form in the center of the die due to the momentum carried by the droplets all colliding in the same area in different directions and cancelling out. The fluid trapped will have a large amount of heat transferred to it due to the very high heat loads. Nucleate bubbles are likely to form, which eventually lead to critical heat flux.

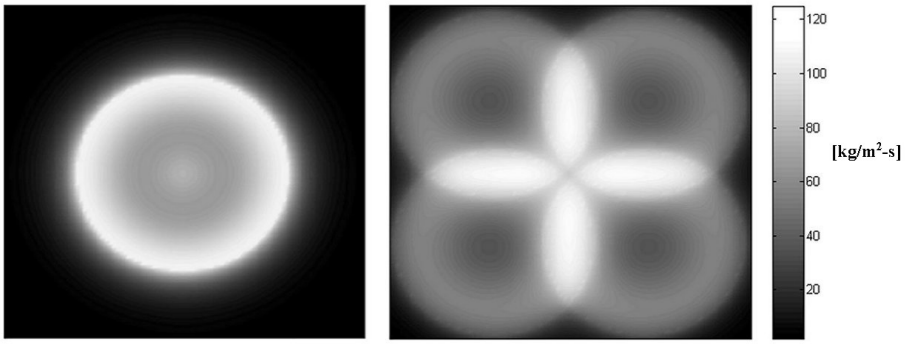

Figure 5.2: Spray distribution of nozzle designs 0A and 0B. 0A is on the left and 0B is on the right

When Equation 5.7 was solved using MatLab, calculations of the film thickness and velocity were made. Film thickness predictions ranged from 55 to 280 microns. The film was predicted to be thickest and the corners and thinnest at the radius of the spray cone. The center of the die had a film thickness less than regions outside the spray cone radius. Film velocities were predicted to range from between 0 and 9 m/s. Modeling was only done for design 0A and 0B as these were the only designs the nozzle manufacturer had data for. The model predicts an average film thickness measurement of 125.8 μm for a flow rate of 0.583 ml/s. The film was calculated to be the thinnest, 72.3 μm , in the region under the spray and the thickest, 280.0 μm , at the die corner. A contour plot of the film thickness from the model is shown in Fig. 5.3. The values of film thickness are in μm .

The predicted film thicknesses are compared to the experimentally measured film thicknesses for design 0A in Figure 5.4. The numerical results are the values in brackets, and all values are in μm. The figure shows fairly good agreement between the two. The trends seen in the model can be experimentally verified: the film is thinner in the center regions and becomes thicker as it approaches the edge of the die. The absolute numerical values are also in relatively close agreement. The figure shows that this relatively simple spray model was able to describe the behavior of the film.

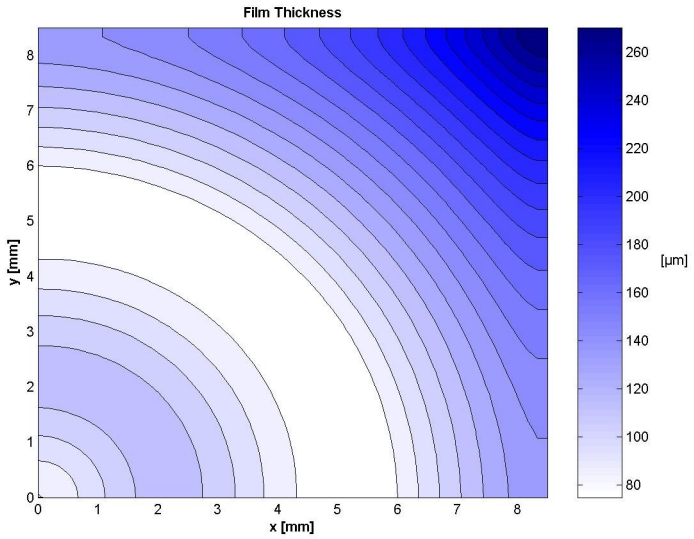

Figure 5.3: Thicknesses of the liquid film predicted by the computer model for nozzle 0A

The model was also able to predict the velocity of the film. The results of this is shown in Figure 5.5. The model predicts the highest film velocity in the region under the radius of the spray cone, as seen in Figure 5.2. Inside of the cone radius, there are less droplets impacting the surface of the film, therefore less dynamic pressure driving the fluid out. After

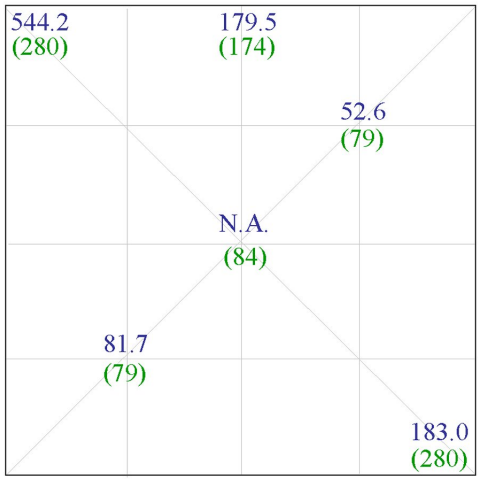

Figure 5.4: A comparison of the measured film thicknesses to the values predicted by the computer model for nozzle 0A. Model results are shown in brackets. Thicknesses are in μm

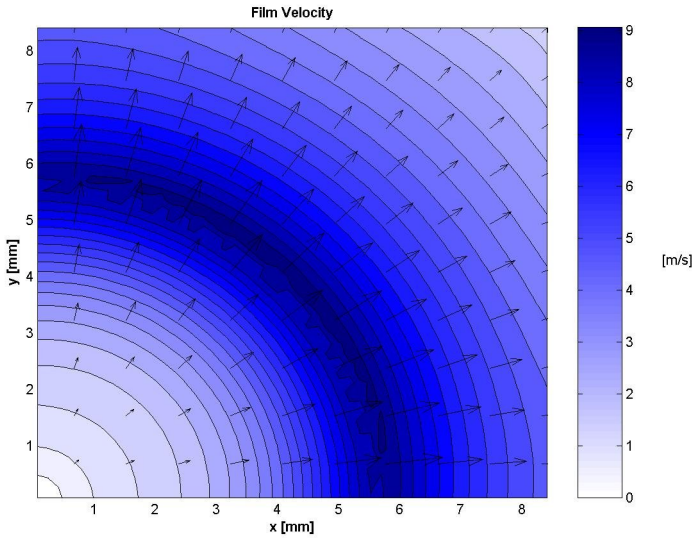

Figure 5.5: Velocities of the liquid film predicted by the computer model for nozzle 0A

the spray cone radius, no additional mass is being added by incoming droplets, so the film slows down as it expands outward towards the edge.

Models of the film thickness and film velocity were also run for nozzle design 0B. This model differed slightly from the previous model in that the effects of four nozzles had to be considered. The governing equations given above remained the same, however the spray characteristics that were input to these equations were different. The model's predictions for the film thickness for nozzle 0B is shown in Figure 5.6. The model predicts that the thickest region of the film will be in the corner of the die, with an additional thick region underneath the spray cones. Areas of high spray interaction are shown to have small film thicknesses as seen by the white ovals. No experimental results were available for comparison with this model.

The film velocity for nozzle 0B was also modeled, and the result is shown in Figure 5.7. The average film velocity of this nozzle design is higher than nozzle 0A. There is a small region at the center where an area of low velocity is predicted resulting from a small number of droplets impacting the film to create a dynamic pressure and due to the influence of the

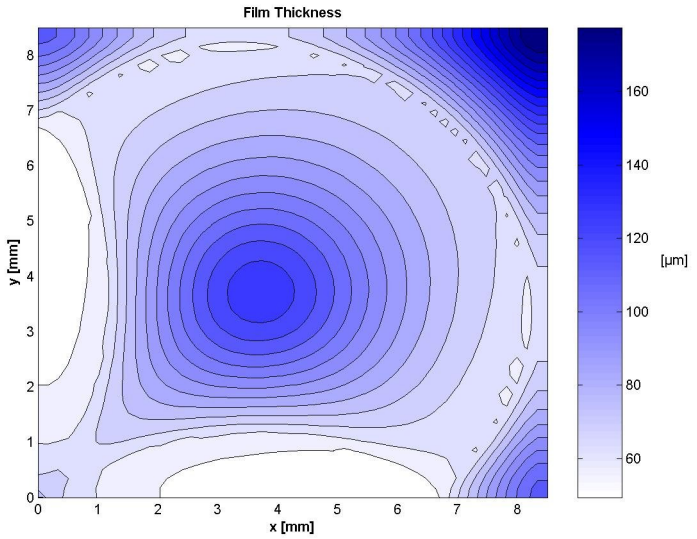

Figure 5.6: Thicknesses of the liquid film predicted by the computer model for nozzle 0B

neighboring nozzles. The film accelerates as it approaches the radius of the spray cone and leaves the die at a high velocity.

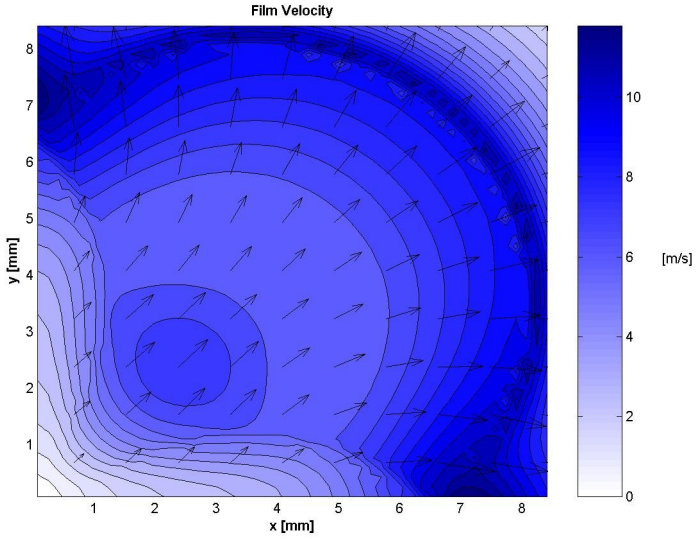

Figure 5.7: Velocities of the liquid film predicted by the computer model for nozzle 0B

Chapter 6

Discussion

Evidence has been given through-out this thesis supporting the fact that the spray cooling system tested in this experiment performs well due to the single-phase component of the system. Critical heat flux is reached when part of the die enters into the nucleate boiling regime. Suppression of this regime leads to higher critical heat fluxes. In general, higher heat transfer coefficients result when the die operates in single phase modes. Spray cooling designs that do not rely on nucleate boiling as the primary mechanism of heat removal have been called Spray Cooling with Phase Change instead of Spray Evaporative Cooling, which implies a heavy dependance on nucleate boiling.

Figure 6.1 shows nozzle 0A spraying onto a visualization die. The left half of the figure is an adiabatic test case. It shows the liquid film and the spray effected region. Droplet impact regions can be seen. Also, bubbles are seen in the film. Since this is an adiabatic case, the source of these bubbles must have been entrainment. The image on the right is the same nozzle and die, but with an applied heat flux of 28 W/cm^2. This corresponds to a heat load near critical heat flux for this nozzle design. There is a definite increase in the number of nucleate bubbles present in the film, especially at the corners and edges of the die. Large bubbles can be seen growing and separating from the surface. The area in the center of the die looks similar in both the adiabatic and powered tests. The heat transfer coefficient was measured to be higher in the center of the die for this nozzle design, where there is no evidence of surface nucleate boiling. Critical heat flux is reached at the corners, where nucleate boiling is occurring.

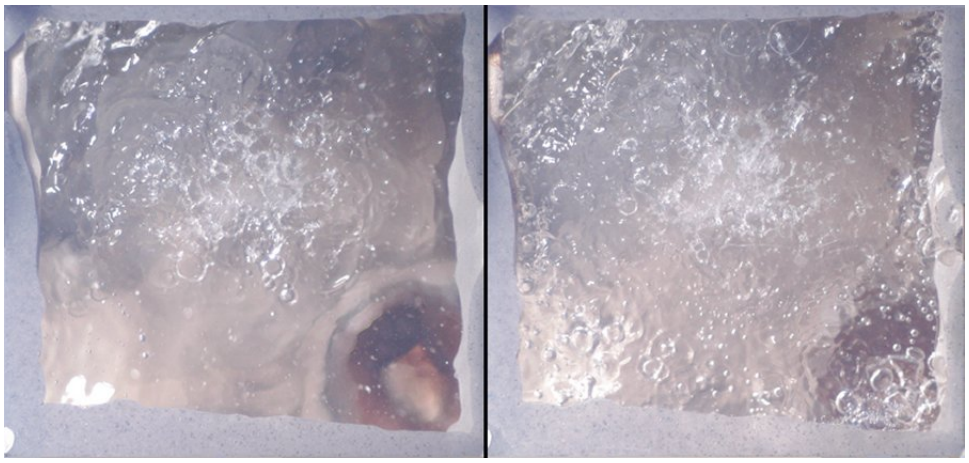

Figure 6.1: A visualization of spray nozzle 0A. The left picture is the adiabatic case. The right picture is with an applied heat flux of 28 W/cm^2

To illustrate the impact region of the spray, the computer model of the volumetric flow flux distribution was overlayed on an image of a visualization die at a heat load of 28 W/cm^2. This image is shown in Figure 6.2. In the figure, a large number of fairly large nucleate bubbles can be seen. Most of these occur outside of the spray region.

Images of nozzle design 0B cooling a powered visualization die were also taken. One set of images is shown in Figure 6.3. Both of these images exhibit the cross-shaped region of spray interaction that was predicted by the numerical model. This region appears as a highly turbulent stream. In the image on the left, the adiabatic image, a much higher level of entrainment is seen than was in nozzle design 0A. Also, because of the four nozzle design, the spray impact region covers nearly the entire die. The image on the right in Figure 6.3 is the same die and nozzle design, but with the die at a heat flux of 18 W/cm^2 (53 W). This is still far below the critical heat flux for this nozzle design but was the highest level reached in testing with this die. Little difference can be distinguished between the two images. In both images though, there is a build-up of fluid in the center of the die where the fluid from different nozzles collide. As was shown in Section 4.1.4, this was the area of the die that had the worst heat transfer characteristics.

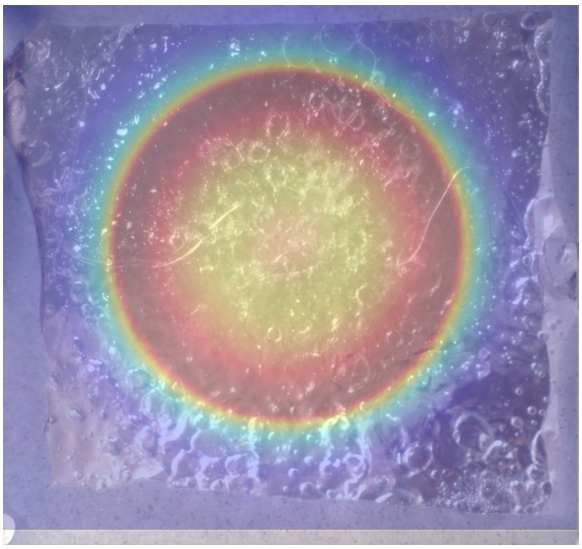

Figure 6.2: Spray distribution model overlayed on 28 W/cm^2 (80 W) nozzle 0A spray test

In Section 4.1.3, evidence was presented to show that spray designs that do not rely on nucleate boiling were able to reach higher critical heat fluxes. This is intuitive; critical heat flux will not be reached if there are no nucleate bubbles growing on the die surface. The primary function of nucleate boiling in pool boiling is not to remove latent heat but to mix the fluid near the surface and deliver cooler fluid. They serve the same purpose here. The

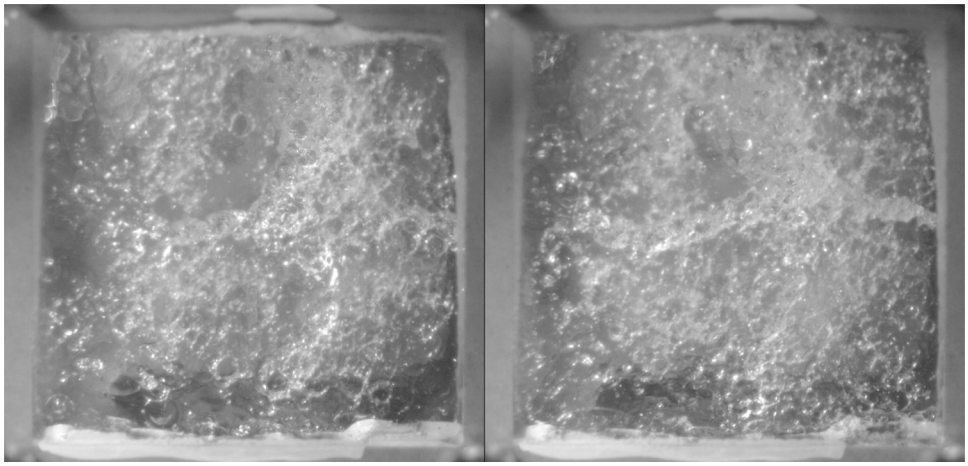

Figure 6.3: A visualization of spray nozzle 0B. The left picture is the adiabatic case. The right picture is with an applied heat flux of 18 W/cm^2

importance of these bubbles is not to remove latent heat but to serve as mixers for the thin film. Some nozzle designs are more likely to entrain bubbles as they impact the film. These bubbles also serve as mixers, enhancing the turbulence of the film. Designs that have more bubble entrainment have a well-mixed film and nucleate boiling is not necessary. These are the designs that show higher heat transfer coefficients and critical heat flux values.

Film thickness measurements presented in Section 4.2 and modeling results in Chapter 5 also help to explain critical heat flux for the single nozzle designs, such as 0A. The film is predicted and measured to be thinner in the center region of the die. At the corners, where critical heat flux occurs, the film thickens. Any bubbles being carried by the film would be relatively smaller with respect to the film thickness in the center of the die than they would at the corners. In the thin regions, they would be able to mix more of the fluid than they would in the thicker regions. Because of the loss of turbulent mixing near the surface from entrained bubbles, nucleate bubbles begin to form to enhance the mixing.

Spray cooling has been shown to have the capability of removing very large amounts of heat from very compact areas. An understanding of how this process works is being gained that leads to the ability of designing new spray cooling systems that take advantage of these processes. Using this knowledge, higher levels of heat removal will be available from the next generation of spray cooling systems.

Bibliography

[1] G. E. Moore. Cramming more components onto integrated circuits. *Electronics*, 8(38):1–4, 1965.

[2] B. Siegel. Reliability and the electronic engineer. Application note, 1998.

[3] J. D. Parry, J. Rantala, and J.M. Lasance. Enhanced electronic system reliability-challanges for temperature prediction. *IEEE transactions on compenents and packaging technologies*, 25:533–538, 2002.

[4] G. Pautsch. An overview on the system packaging of the CRAY SV2 supercomputer. In *Proceedings of IPACK'01, The Pacific Rim/ASME International Electronic Packaging Technical Conference and Exhibition*, pages 617–624. ASME, 2001.

[5] C. G. Malone, C. E. Bash, and C. D. Patel. Passive spray coolant pump. U.S. Patent Number 6,708,515, March 2004.

[6] G. Pautsch. Spray evaporative cooling system and method. U.S. Patent Number 6,646,879, November 2003.

[7] E. J. Morrow, S. M. Sellers, and G. D. Knudsen. Modular spray cooling system for electronic components. U.S. Patent Number 6,625,023, September 2003.

[8] C. D. Patel and C. E. Bash. Spray cooling with local control of nozzles. U.S. Patent Number 6,616,120, September 2003.

[9] G. W. Pautsch. Method and apparatus for cooling electronic components. U.S. Patent Number 6,580,690, 2003.

[10] D. P. Rini, H. R. Anderson, J. S. Kapat, and L. Chow. Method and apparatus for high heat flux heat transfer. U.S. Patent Number 6,571,569, 2003.

[11] H. C. Miller, K. M. Dinndorf, and B. D. Stewart. Liquid spray phase-change cooling of laser devices. U.S. Patent Number 6,354,370, March 2002.

[12] P. J. Fitzgerald, S. G. Buczek, F. C. Rupp, and G. M. Christopher. Liquid spray cooled module. U.S. Patent Number 6,292,364, September 2001.

[13] D. E. Tilton and C. L. Tilton. High heat flux evaporative spray cooling. U.S. Patent Number 5,220,804, June 1993.

[14] K. A. Estes and I. Mudawar. Correlation of Sauter mean diameter and critical heat flux for spray cooling of small surfaces. *International Journal of Heat and Mass Transfer*, 38(16):2985–2996, 1995.

[15] S. Toda. A study of mist cooling (1st report: investigation of mist cooling). *Heat Transfer: Japanese Research*, 1:39–50, 1972.

[16] D. P. Rini. *Pool boiling and spray cooling with FC-72*. PhD thesis, University of Central Florida, May 2000.

[17] J. Walker. Boiling and the leidenfrost effect. Technical report, Clevelent State University, 1997.

[18] M. J. Morgan, W. S. Chang, M. R. Pais, and L. C. Chow. Comparison of high heat-flux cooling applications. In A. M. Khounsary, editor, *High Heat Flux Engineering*, volume 1739 of *Proceedings of SPIE – The International Society for Optical Engineering*, pages 17–28, San Diego, CA, July 1992.

[19] A. G. Pautsch and T. A. Shedd. The effects of nozzle configuration and coolant flow rate on spray evaporative cooling in a multi-chip module using FC-72. In *Proceedings of IPACK03: The International Electronic Packaging Technical Conference and Exhibition*, Maui, Hawaii, July 2003.

[20] L. Yan. *Dropwise evaporative cooling of solid surfaces.* PhD thesis, The University of Maryland, College Park, Maryland, December 1992.

[21] G. Pautsch and A. Bar-Cohen. Thermal management of multichip modules with evaporative spray cooling. In *Advances in Electronic Packaging*, volume EEP-Vol. 26-2, pages 1453–1461. ASME, New York, 1999.

[22] I. Mudawar and W. S. Valentine. Determination of the local quench curve for spray-cooled metallic surfaces. *Journal of Heat Treatment*, 7:107–121, 1989.

[23] S. Toda. A study of mist cooling (2nd report: Theory of mist cooling and its fundamental experiments. *Heat Transfer: Japanese Research*, 3:1–44, 1974.

[24] V.I. Tolubinskii, V.A. Antonenko, A.A. Kriveshko, and Yu.N. Ostrovskii. Supression of nucleate boiling in a stationary liquid film. *High Temp*, 15(4):693–697, Jul-Aug 1977.

[25] D. B. Jordan and G. Leppert. Pressure drop and vaper volume with subcooled nucleat boiling. *International Journal of Heat and Mass Transfer*, 5:751–761, 1962.

[26] K. Nishikawa and K. Yamagata. On the correlation of nucleat boiling heat transfer. *International Journal of Heat and Mass Transfer*, 1:219–235, 1960.

[27] J. H. Kim, K. N. Rainey, S. M. You, and J. Y. Pak. Mechanism of nucleate boiling heat transfer enhancement from microporous surfaces in saturated FC-72. *Journal of Heat Transfer*, 124(3):500–506, June 2002.

[28] H. Zhang, I. Mudawar, and M. M. Hasan. Experimental assessment of the effects of body force, surface tension force, and inertia on flow boiling CHF. *International Journal of Heat and Mass Transfer*, 45:4079–4095, 2002.

[29] C. E. Bash, C. D. Patel, and R. K. Sharma. Inkjet assisted spray cooling of electronics. In *Proceedings of IPACK03: The International Electronic Packaging Technical Conference and Exhibition*, Maui, Hawaii, July 2003.

[30] C. D. Patel. A vision of energy aware computing from chips to data centers. In *Proceedings of ISMME2003: The International Symposium on Micro-Mechanical Engineering*, December 2003.

[31] S.-W. Tan. *Computer simulation of a spray cooling system with FC-72*. PhD thesis, University of Central Florida, Orlando, Florida, 2001.

[32] T. Bergman and R. Mesler. Bubble nucleation studies Part I: formation of bubble nuclei in superheated water by bursting bubbles. *AIChE Journal*, 27(5):851–853, September 1981.

[33] K. Carroll and R. Mesler. Bubble nucleation studies Part II: bubble entrainment by dro-formed vortex rings. *AIChE Journal*, 27(5):853–856, September 1981.

[34] H. C. Pumphrey and P. A. Elmore. The entrainment of bubbles by drop impacts. *Journal of Fluid Mechanics*, 220:539–567, 1990.

[35] B. Horacek, J. Kim, and K. T. Kiger. Effects of noncondensable gas and subcooling on the spray cooling of an isothermal surface. In *Proceedings of the ASME IMECE 2003*, pages Paper IMECE2003–41680, Washington, D.C., November 2003. American Society of Mechanical Engineers.

[36] H. Kubo, H. Takamatsu, and H. Honda. Effects of size and number density of micro-reentrant cavities on boiling heat transfer from a silicon chip immersed in degassed and gas-dissolved FC-72. *Journal of Enhanced Heat Transfer*, 6:151–160, 1999.

[37] K. N. Rainey, S. M. You, and S. Lee. Effect of pressure, subcooling, and dissolved gas on pool boiling heat transfer from microporous, square pin-finned surfaces in FC-72. *International Journal of Heat and Mass Transfer*, 46:23–35, 2003.

[38] R. H. Pereira, S. L Braga, and J. A. R. Parise. Comparing single phase heat transfer to arrays of impinging jets and sprays. *Proceedings of IMECE2002*, 2002.

[39] L. Lin and R. Ponnappan. Heat transfer characteristics of evaporative spray cooling in a closed loop. In *Proceedings of the SAE Power Systems Conference*, pages SAE Paper No. 2002–01–3198, Coral Springs, FL, October 2002. Society of Automotive Engineers.

[40] L. Lin and R. Ponnappan. Heat transfer characteristics of spray cooling in a closed loop. *International Journal of Heat and Mass Transfer*, 46(20):3737–3746, September 2003.

[41] J. Yang, L. C. Chow, M. R. Pais, and A. Ito. Liquid film thickness and topography determination using Fresnel difraction and holography. *Experimental Heat Transfer*, 5(4):239–252, 1992.

[42] D. E. Tilton. *Spray cooling*. PhD thesis, University of Kentucky, Lexington, Kentucky, Dec 1989.

[43] W. S. Mathews, C. F. Lee, and J. E. Peters. Experimental investigations of spray/wall impingement. *Atomization and Sprays*, 13(2&3):223–242, 2003.

[44] J. Li. Spray evaporative cooling in high heat flux electronics. Master's thesis, University of Minnesota, August 2000.

[45] Fluorinert electronic liquid FC-72. Product information, 2000.

[46] T. A. Shedd. An automated optical liquid film thickness measurement method. Master's thesis, University of Illinois at Urbana-Champaign, Urbana, IL, 1998.

[47] E. Hecht. *Optics*. Addison-Wesley, Reading, Massachussetts, third edition, 1998.

[48] T. A. Shedd and T. A. Newell. Automated optical liquid film thickness measurement method. *Review of Scientific Instruments*, 69(12):4205–4213, 1998.

[49] H Ohta. Experiments on microgravity boiling heat transfer by using transparent heaters. *Nuclear Engineering and Design*, 175:167–180, 1997.

[50] J. L. Hay and D. K. Hollingsworth. Calibration of micro-encapsulated liquid crystals using hue angle and a dimensionless temperature. *Experimental Thermal and Fluid Science*, 18:251–257, 1998.

[51] I. Mudawar. Assessment of high-heat-flux thermal management schemes. *IEEE Transactions on Components and Packaging Technologies*, 24(2):122–141, 2001.

Procedure for Spray Plate Replacement

Adam Pautsch
VOSEC Project
Solar Energy Lab, MFVAL
UW-Madison

1. Use the program to stop the system
2. Turn off power to Main Power Supply
    a. Push the power switch to the Off (0) position
    b. Wait for the fans to stop and the lights to go off
3. Turn off the DAQ unit
4. Disconnect all electrical connections
    a. Carefully use the camming rod to open the edge connectors
    b. Disconnect the two white MOLEX power connections (A&B and C&D)
5. Disconnect all fluid connections
    a. Uncouple the Inlet Parker fitting, then the Outlet Parker fitting
    b. Uncouple the two pressure transducer connections
6. Open the two red latches holding the node in place and slide the node out of the rail and set on the table with the cap up as shown in Figure 1
7. Remove the manifold cover as shown in Figure 2. Turn screws only a few turns at a time so as not to jam or kink the fittings or the O-ring seals
    a. Remove the screws holding manifold to manifold stand-offs (Screw set 1)
    b. Remove the screws holding manifold to big adapter (Screw set 2)
    c. Remove the screws holding manifold to small adapter (screw set 3)
8. Remove the spray cap as shown in Figure 3
    a. The numbers indicate the sequence for turning the load nut in order to keep the forces balanced on the MCM
    b. Turn each load nut no more than two revolutions before moving to the next screw in the sequence
    c. When all load nuts are loose, remove them, their washers, and the springs
    d. Carefully remove the cap from the screws
        i. If the MCM is stuck, hold the yellow interconnect frame and gently pull apart
        ii. If the MCM is still stuck to the O-ring, gently pry it off
    e. Turn the cap over away from the node and catch the washers
9. Replace the spray plate with the desired test plate
    a. Check to see that the O-ring seal between the plate and cap is in place
    b. Use a sequence with the screws to insure that the plate is properly aligned
10. Make sure that the MCM and interconnect are back in their proper place
11. Check the O-ring seal on the bottom of the spray cap to insure that it is in place and not twisted or kinked
12. Place the spray cap over the MCM
    a. Place the washers in the eight locations on the cap
    b. Inspect the eight springs for defects and place them over the screws
    c. Put the washers back on the load nuts and place the load nuts over the screws

13. Tighten down the spray cap using the numbered sequence
    a. Start the threads of each load nut by hand
    b. Turn each load nut no more than two revolutions before moving to the next screw in the sequence shown in Figure 3
    c. It will take approximately twelve revolutions to tighten all load nuts
    d. DO NOT over-tighten the load nuts as it will damage the MCM and screws
14. Replace the manifold
    a. Gently press the manifold cover down to seed the large and small adapters into the spray cap
    b. Use the number sequence from Figure 2 to attach the manifold to the node and the adapters
15. Use the vacuum recovery system to evacuate the node card to a full vacuum
16. Slide the node card back into the side rails
17. Reattach the fluid connections – fluid outlet side first (in case of pressure build-up)
18. Close the two red latches holding the node in place
19. Use the camming rod to re-connect the edge connectors
20. Plug the two white power connectors back in
21. Turn on the DAQ
22. Turn on the Main Power supply
23. Use the computer program to continue testing

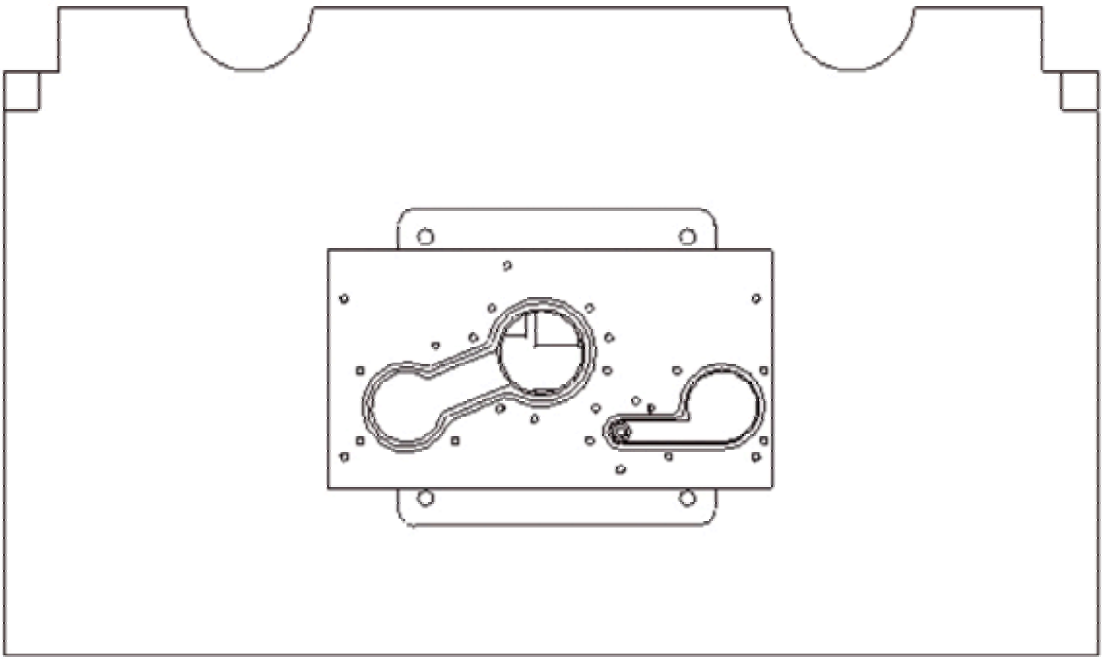

Figure 1: Node card

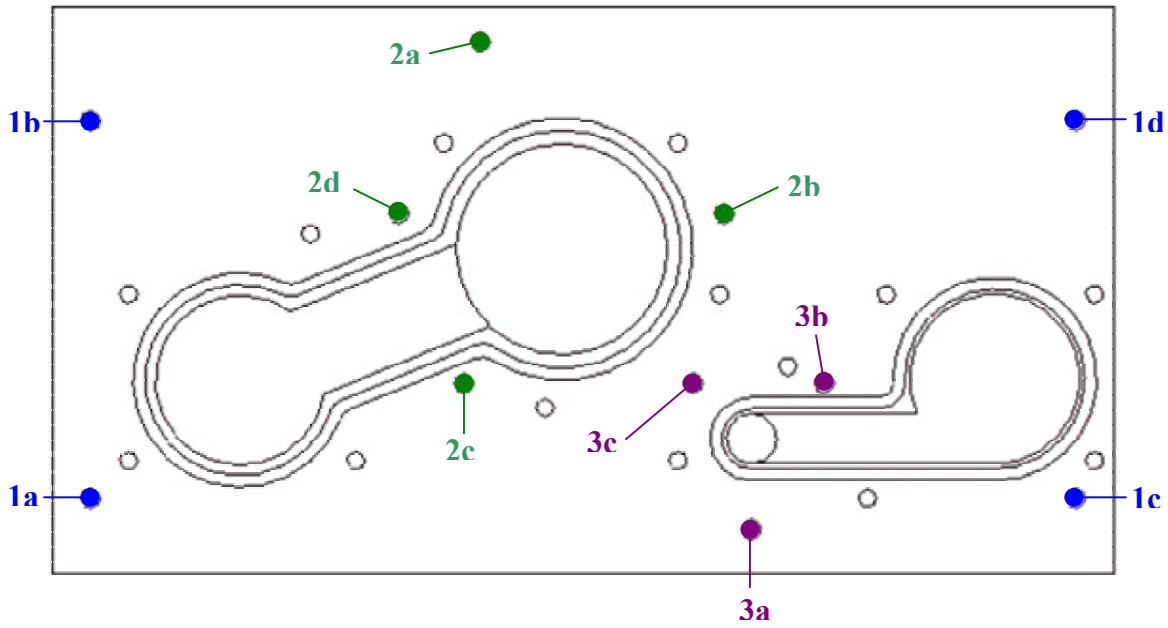

Figure 2: Manifold cover

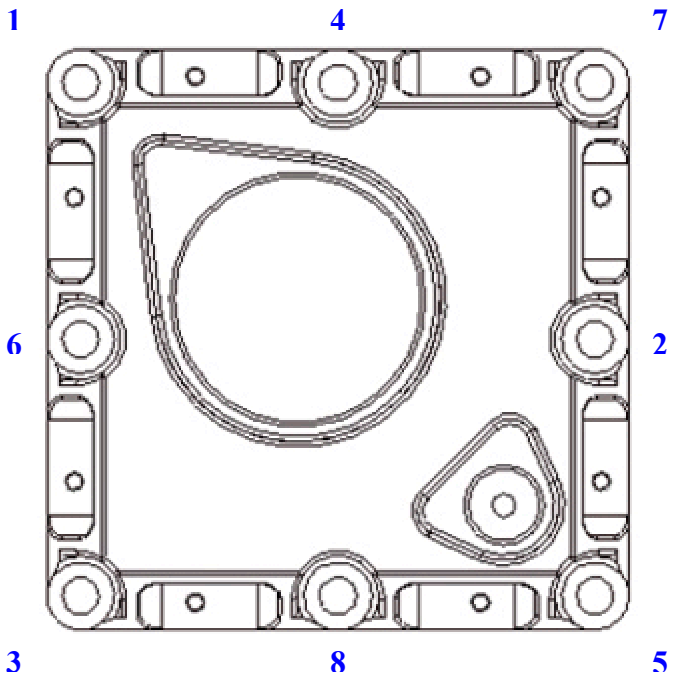

Figure 3: Spray cap

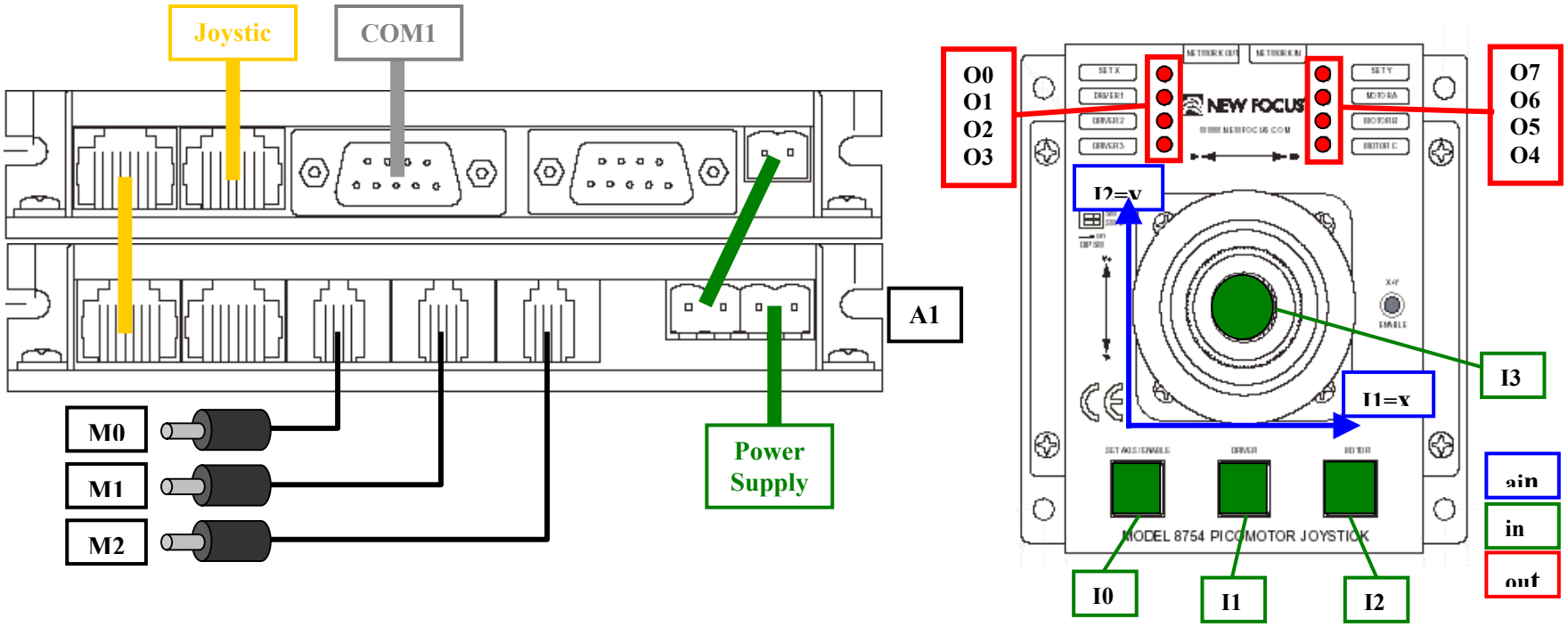

<driver> = A1-A31	We only have A1
<motor> = 0,1,2	0 is A, 1 is B, 2 is C
<type>	0 is Standard, 1 is Tiny
<axis>	1 is I1 is x, 2 is I2 is y
<button>	0-3, see the diagram
<led>	0-7, see the diagram
<state>	0 is Off, 1 is On
<a#>	Accelerations from 16-32,000
<v#>	Velocities from 1-2,000
<mv#>	Minimum velocities must be less than velocities
<#>	Number of steps to take (no limit)

Syntax	Command	Example
def	Load default parameters	
ini	Initializes devices	
sav	Saves the currently set parameters	
ver	Displays the firmware version	
acc [<driver>] [<motor>]	Query motor acceleration	acc a1 1 (acceleration of motor 1 on driver A1)
acc <driver> <motor>=<a#>	Sets the acceleration of the specified motor	acc a1 0=10000 (acceleration of motor 0 on diver A1 is set to 10,000)
chl [<driver>]	Returns the active motor channel for the driver	chl a1 (tells which motor is active on driver A1)
chl <driver>=<motor>	Sets the active motor for a driver	chl a1=0 (makes motor 0 active on driver A1)
for <driver> [=<v#>]	Sets the driver to move forward at a velocity	for a1=1500 (A1 is set to move forward at 1500 Hz)
go [<driver>]	Starts the motor	go (Starts the active motor on each driver)
hal [<driver>]	Smoothly stops motors with preset acceleration	hal (Stops active motor on each driver at the set acceleration)
mof [<driver>]	Turns off the motors of the specified driver	mof a1 (turns off driver A1)
mon [<driver>]	Enables the drivers. Drivers must be enabled before their motors can be run	mon a1 (enables driver A1)
mpv [<driver>[<motor>]]	Query Minimum Profile Velocity	mpv a1 1 (displays minimum velocity for motor 1 on driver A1)
mpv <driver> <motor>=<mv#>	Sets the Minimum Velocity Profile	mpv a1 0=50 (sets mpv for motor 0 on driver A1 to 50)
pos [<driver>]	Displays the number of pulses sent to motor	pos (displays the pulse sent to all motors)
rel <driver>=<#>	Set the number of steps to move	rel a1=2500 (Sets active motor on A1 to move 2500 steps)
rev <driver> [=<value>]	Sets the driver to move in reverse at a velocity	rev a1=1500 (A1 is set to move backwards at 1500 Hz)
sta [<driver>]	Returns the status of the drivers	sta (Returns the status of all modules)
sto [<driver>]	Stops the motors	sto a1 (Stops the active motor on driver A1)
typ [<driver>] [<motor>]	Displays the motor type	typ a1 0 (Displays the type of motor for Motor 0 of driver A1)
typ <driver> <motor>=<type>	Set the motor type	typ a1 0=0 (Sets motor 0 of driver A1 to Standard)
vel [<driver>] [<motor>]	Returns the velocity	vel a1 1 (Displays the velocity of motor 1 of driver A1)
vel <driver> <motor>=<v#>	Sets the velocity	vel a1 1=1500 (Sets the velocity of motor 1 of driver A1 to 1500 Hz)
ain [<axis>]	Returns values for the position of the joystick	ain (Displays the x and y position of the joystick)
in [<button>]	Returns the state of the button of the joystick	in 2 (Displays the state of button 2 on the joystick)
jof	Turns off the joystick	jof (Turns the joystick off)
jon	Turns on the joystick	jon (Turns the joystick on)
out [<led>]	Returns the states of the LEDs on the joystick	out 7 (Returns the state of LED 7 from the joystick)
out <led>=<state>	Sets the state of the LEDs on the joystick	out 7=0 (Turns LED 7 on the joystick off)

Procedure for Pulling a Vacuum

Adam Pautsch
UW-Madison
6-4-03

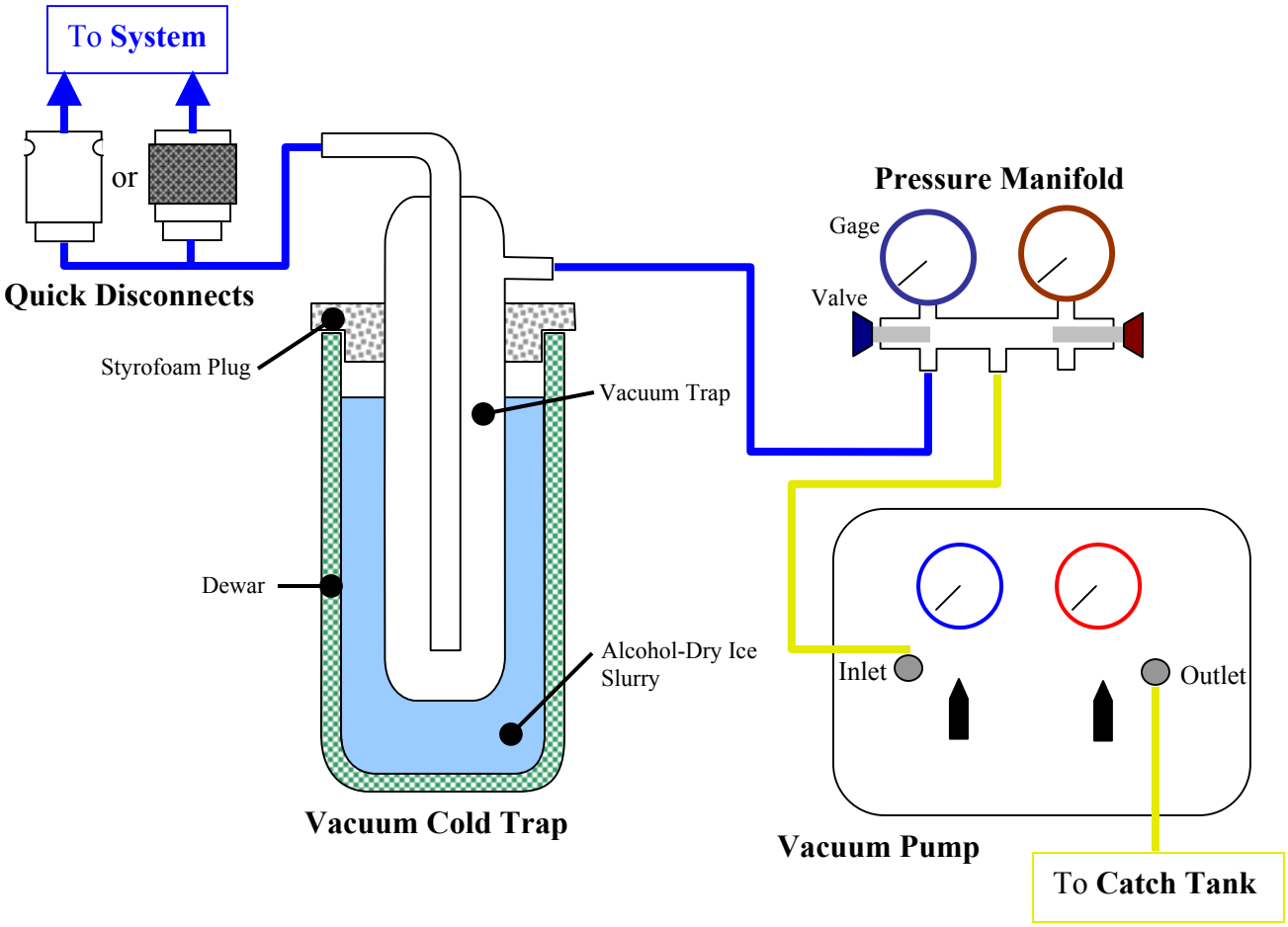

Pulling a Vacuum

1. If the **Vacuum Cold Trap** is being used, follow the instructions in Cold Trap Preparation
2. Make all hose connections as shown in the figure
3. Make sure that the blue and red valves on the **Pressure Manifold** are closed
4. Set **Inlet Valve** to **Self Evac** and the **Outlet Valve** to **Liquid/Purge**
5. Plug the **Vacuum Pump** into an extension cord
6. Switch the **Tank Bypass** to **On** and turn the **Power Switch** to **On**
7. Wait for the system to achieve a vacuum as indicated on the blue inlet vacuum gage
8. Turn the **Inlet Valve** to **Recover**
9. Turn the **Outlet Valve** to **Vapor**
10. Open the blue valve on the **Pressure Manifold**
11. Wait for thesystem to achieve a vacuum, then wait 3-5 minutes or more depending on how full of a vacuum is required
12. Undo the **Quick Disconnect** to the system
13. Turn the **Outlet Valve** to **Liquid/Purge**

14. Turn the **Inlet Valve** to **Self Evac**
15. Close the blue valve on the **Pressure Manifold**
16. Switch the **Power Switch** of the **Vacuum Pump** to **Off**

Cold Trap Preparation

1. Temper the **Dewar** with cold tap water or ice water and wipe clean with lint-free cloth
2. Fill the **Dewar** approximately ½ full of 200 proof alcohol

   ! Never fill the Dewar with cold (sub-freezing) alcohol, it will cause it to crack!

3. Insert a thermocouple into the **Dewar** to monitor the temperature
4. Slowly add 1-1.5 lbs of dry ice or until the temperature in the **Dewar** is less than –70 C
5. Insert the **Vacuum Trap** into the hole in the **Styrofoam Plug**
6. Slowly insert the **Vacuum Trap** into the **Dewar** until the **Styrofoam Plug** stops

   ! When emptying the dewar, NEVER pour cold liquid over the lip of the dewar, it will cause it to crack!

Ring model

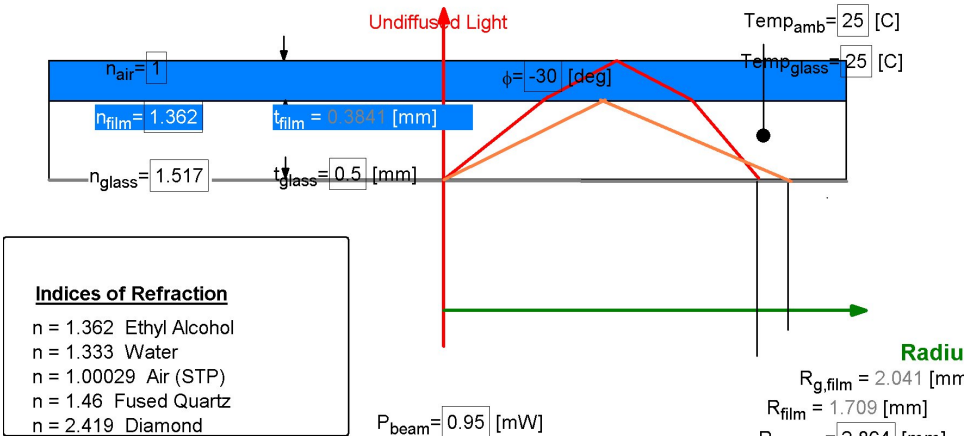

Equations

Adam Pautsch 4-13-03

Critical Angle between two mediums

function CritAngle$(N_1,\ N_2,\ \theta_i)$ (1)

If $(N_1 > N_2)$ then $angle := \arcsin(N_2/N_1)$ else $angle := 90$ (2)

$CritAngle := angle$ (3)

end (4)

Transmitance Angle between to mediums

function TransAngle$(N_1,\ N_2,\ \theta_i,\ \theta_c)$ (5)

If $(\theta_i < \theta_c)$ then $\theta_t := \arcsin(N_1/N_2 \cdot sin(\theta_i))$ else $\theta_t := 90$ (6)

$TransAngle := \theta_t$ (7)

end (8)

Reflection of Perpendicular Polarization

function RPerp$(N_1,\ N_2,\ \theta_i,\ \theta_t,\ \theta_c)$ (9)

If $(\theta_i < \theta_c)$ then $Rs := \left(\frac{(n_1 \cdot \cos(\theta_i) - n_2 \cdot \cos(\theta_t))}{(n_1 \cdot \cos(\theta_i) + n_2 \cdot \cos(\theta_t))}\right)^2$ else $Rs := 1$ (10)

$RPerp := Rs$ (11)

end (12)

Reflection of Parallel Polarization

function RPara(N_1, N_2, θ_i, θ_t, θ_c) (13)

If $(\theta_i < \theta_c)$ then $Rp := \left(\frac{(N_2 \cdot \cos(\theta_i) - N_1 \cdot \cos(\theta_t))}{(N_1 \cdot \cos(\theta_t) + N_2 \cdot \cos(\theta_i))}\right)^2$ else $Rp := 1$ (14)

$RPara := Rp$ (15)

end (16)

Laser Beam Properties

$\lambda_{HeNe} = 632.8$ [nm] (17)

$Power_{beam} = 0.95$ [milliW] (18)

$d_{beam} = 0.48$ [mm] (19)

$\theta_{div,rad} = 1.7$ [mrad] (20)

$\theta_{div} = \theta_{div,rad} \cdot \left|0.057296 \frac{deg}{mrad}\right|$ (21)

Longitudinal mode spacing = 1090 MHz

$d_{beam,x} = d_{beam} + 2 \cdot \tan(\theta_{div}) \cdot x$ (22)

$z_r = \pi \cdot \frac{d_{beam}^2}{\lambda_{HeNe} \cdot \left|1 \times 10^{-6} \frac{mm}{nm}\right|}$ (23)

$d_r = \sqrt{(2)} \cdot d_{beam}$ (24)

Photo Detector

$Area_{PD,active} = l_{PD} \cdot w_{PD}$ (25)

$l_{PD} = 3.6$ [mm] (26)

$w_{PD} = 3.6$ [mm] (27)

Gain = 0 dB

Wavelength = 633 nm

$Gain_{experimental} = 1.375$ [V] (28)

$Power_T = Power_{beam} \cdot (T_s / Gain_{experimental})$ (29)

$Power_R = Power_{beam} \cdot (R_s / Gain_{experimental})$ (30)

$Power_S = Power_{beam} - (Power_T + Power_R)$ (31)

Calculate Required Angles

$$\theta_{c,film,air} = \arcsin\left(n_{air}/n_{film}\right) \tag{32}$$

$$\theta_{c,glass,air} = \arcsin\left(n_{air}/n_{glass}\right) \tag{33}$$

$$\theta_{c,glass,film} = \arcsin\left(n_{film}/n_{glass}\right) \tag{34}$$

$$\theta_{i,glass,film,c} = \arcsin\left(n_{film}/n_{glass} \cdot \mathit{sin}\left(\theta_{c,film,air}\right)\right) \tag{35}$$

$$\theta_{t1} = \theta_{c,film,air} - \phi \tag{36}$$

$$\theta_{t2} = \theta_{c,film,air} + \phi \tag{37}$$

$$\theta_{i1} = \arcsin\left(n_{film} \cdot \frac{\mathit{sin}\left(\theta_{t1}\right)}{n_{glass}}\right) \tag{38}$$

$$\theta_{i2} = \arcsin\left(n_{film} \cdot \frac{\mathit{sin}\left(\theta_{t2}\right)}{n_{glass}}\right) \tag{39}$$

Ring Radius Relations

$$R_{g,no,film} = 2 \cdot t_{glass,T} \cdot \tan\left(\theta_{c,glass,air}\right) \tag{40}$$

When there is no water film

$$R_{g,film} = 2 \cdot t_{glass,T} \cdot \tan\left(\theta_{c,glass,film}\right) \tag{41}$$

When there is a water film

$$R_{film} = 2 \cdot \left(t_{glass,T} \cdot \tan\left(\theta_{i,glass,film,c}\right) + t_{film} \cdot \tan\left(\theta_{c,film,air}\right)\right) \tag{42}$$

$$R_{film,\phi} = t_{glass,T} \cdot \tan\left(\theta_{i1}\right) + t_{film} \cdot \tan\left(\theta_{t1}\right) + t_{film} \cdot \tan\left(\theta_{t2}\right) + t_{glass,T} \cdot \tan\left(\theta_{i2}\right) \tag{43}$$

$$t_{glass,T} = T_{glass} + t_{glass} \cdot \beta_{thermo} \cdot \Delta T \tag{44}$$

corrected for thermal expantion

$$\Delta T = \mathit{Temp}_{glass} - \mathit{Temp}_{amb} \tag{45}$$

Reflectance from Fresnel's Equations

$$R_{perp} = \mathrm{RPerp}(n_i,\ n_t,\ \theta_i,\ \theta_t,\ \theta_c) \tag{46}$$

$$R_{para} = \mathrm{RPara}(n_i,\ n_t,\ \theta_i,\ \theta_t,\ \theta_c) \tag{47}$$

$$R = \frac{\left(\sqrt{\left(R_{perp}\right)}\right)^2 + \left(\sqrt{\left(R_{para}\right)}^2\right)}{2} \tag{48}$$

$$\theta_c = \mathrm{CritAngle}(n_i,\ n_t,\ \theta_i) \tag{49}$$

$$\theta_t = \mathrm{TransAngle}(n_i,\ n_t,\ \theta_i,\ \theta_c) \tag{50}$$

$$n_i = 1.5 \tag{51}$$

$$n_t = 1.0 \tag{52}$$

Reflection for Glass to Film

$$R_{perp,gf} = \mathrm{RPerp}(n_{glass},\ n_{film},\ \theta_i,\ \theta_{t,gf},\ \theta_{c,gf}) \tag{53}$$

$$R_{para,gf} = \text{RPara}(n_{glass},\ n_{film},\ \theta_i,\ \theta_{t,gf},\ \theta_{c,gf}) \tag{54}$$

$$R_{gf} = \frac{\left(\sqrt{(R_{perp,gf})}\right)^2 + \left(\sqrt{(R_{para,gf})}^2\right)}{2} \tag{55}$$

$$\theta_{c,gf} = \text{CritAngle}(n_{glass},\ n_{film},\ \theta_i) \tag{56}$$

$$\theta_{t,gf} = \text{TransAngle}(n_{glass},\ n_{film},\ \theta_i,\ \theta_{c,gf}) \tag{57}$$

Reflection for Film to Air

$$R_{perp,fa} = \text{RPerp}(n_{film},\ n_{air},\ \theta_i,\ \theta_{t,fa},\ \theta_{c,fa}) \tag{58}$$

$$R_{para,fa} = \text{RPara}(n_{film},\ n_{air},\ \theta_i,\ \theta_{t,fa},\ \theta_{c,fa}) \tag{59}$$

$$R_{fa} = \frac{\left(\sqrt{(R_{perp,fa})}\right)^2 + \left(\sqrt{(R_{para,fa})}^2\right)}{2} \tag{60}$$

$$\theta_{c,fa} = \text{CritAngle}(n_{film},\ n_{air},\ \theta_i) \tag{61}$$

$$\theta_{t,fa} = \text{TransAngle}(n_{film},\ n_{air},\ \theta_i,\ \theta_{c,fa}) \tag{62}$$

```
$IfNot ParametricTable = 'Beam Diameter (X)'
```

$$d_{beam,x} = 3.6 \tag{63}$$

```
$EndIf
$IfNot ParametricTable = 'Fresnel Reflectance'
```

$$\theta_i = 45 \tag{64}$$

```
$EndIf
$IfNot ParametricTable = 'Diode Sensor'
```

$$T_s = 1 \tag{65}$$

$$R_s = 1 \tag{66}$$

$$\textit{Test}_{case\$} = \text{‘none’} \tag{67}$$

```
$EndIf
```

Index of Refraction of Corning 1737 glass (ITO base glass)

6th order polynomial fit

$$\lambda_6 = \lambda_{HeNe} \tag{68}$$

$$n_{\lambda,6} = C_{l,0} + C_{l,1} \cdot \lambda_6 + C_{l,2} \cdot \lambda_6^2 + C_{l,3} \cdot \lambda_6^3 + C_{l,4} \cdot \lambda_6^4 + C_{l,5} \cdot \lambda_6^5 + C_{l,6} \cdot \lambda_6^6 \tag{69}$$

$$C_{l,0} = 1.71004306 \tag{70}$$

$$C_{l,1} = -0.000944355196 \tag{71}$$

$$C_{l,2} = 0.00000187250589 \tag{72}$$

$$C_{l,3} = -1.89492536 \times 10^{-9} \tag{73}$$

$$C_{l,4} = 9.70709813 \times 10^{-13} \tag{74}$$

$$C_{l,5} = -2.14180328 \times 10^{-16} \tag{75}$$

$$C_{l,6} = 9.14206313 \times 10^{-21} \tag{76}$$

Linear fit from 3 closet points

$$\lambda_1 = \lambda_{HeNe} \tag{77}$$

$$n_{\lambda,1} = C_{\lambda,7} + C_{\lambda,8} \cdot \lambda_1 \tag{78}$$

$$C_{\lambda,7} = 1.53956311 \tag{79}$$

$$C_{\lambda,8} = -0.0000361433918 \tag{80}$$

$$n_{Corning,633} = n_{\lambda,1} \tag{81}$$

Thermal Expansion of Corning 1737 glass

$$\beta_{thermo} = 37.6 \times 10^{-7} \ [1/\mathrm{C}] \tag{82}$$

Thermal Conductivity of Corning 1737 glass

$$k_{Corning} = C_{k,0} + C_{k,1} \cdot Temp + C_{k,2} \cdot Temp^2 + C_{k,3} \cdot Temp^3 + C_{k,4} \cdot Temp^4 + C_{k,5} \cdot Temp^5 + C_{k,6} \cdot Temp^6 \tag{83}$$

$$C_{k,0} = 0.00245211296 \tag{84}$$

$$C_{k,1} = -0.0000057117494 \tag{85}$$

$$C_{k,2} = 3.19428475 \times 10^{-8} \tag{86}$$

$$C_{k,3} = -6.16649759 \times 10^{-11} \tag{87}$$

$$C_{k,4} = 8.50248527 \times 10^{-14} \tag{88}$$

$$C_{k,5} = -1.17375866 \times 10^{-16} \tag{89}$$

$$C_{k,6} = 8.12982361 \times 10^{-20} \tag{90}$$

$$Temp = Temp_{glass} \tag{91}$$

Density of Corning 1737 glass

$$\rho = 2540 \ \left[\mathrm{kg/m^3}\right] \tag{92}$$

Specific Heat of Corning 1737 glass

$$C_{p,Corning,eq} = 0.176 \ [\mathrm{cal/g \cdot K}] \tag{93}$$

$$C_{p,Corning} = C_{p,Corning,eq} \cdot \left| 4186.8 \ \frac{J/kg\text{-}K}{cal/g\text{-}K} \right| \tag{94}$$

Index of Refraction of VWR Scientific Microslides plain

n_{glass} = 1.52 $\pm$0.01

1. Inspect the system to insure that all connections (fluid and electrical) are made
2. Turn on the DAQ
3. Turn on the Main Power supply
4. Run the program Spray_Tester-UW Madison-prototype.vi
5. If the pointer is not a hand  , press the Tab key on the keyboard until the pointer is a hand
6. Press the 'Program Start' button
7. Press the 'Run' button  so that the arrow turns black 
8. Wait for the temperature of the chips to appear as colored squares
9. Use the mouse to turn on the Pump
10. Click on the 'Fluid Props' tab to see the flow rate and pressure differential of the fluid across the cap. Use the arrow keys on the pump controller box to adjust the pressure drop to the desired level. Note: The pump controller box is on the test stand
11. Use the mouse click back to the 'Controls' tab
12. Turn on the Main Power supply by clicking the Main Power Supply button
13. Make sure that the Temperature Monitor button is set to 'Both Chips' (Purple)
14. Make sure that the chip power select button is set to 'Chip' (Orange)
15. Use the mouse to click the 'Vicor Enable' button
16. Set the P chip and E chip to a safe power level
17. Use the mouse to click the 'Vicor Update' button
18. If the temperatures on the chips are not less than 60 C, repeat steps 16 and 17
19. Use the mouse to turn on the 'Heat Exchanger' fan if necessary
20. Enter a name for the data file in the 'File Name' field
21. Use the mouse to click the 'Make EES file' button
22. Use the mouse to select 'Entire Chip' (Red) with the Temperature Monitor button
23. Select either the 'P-chips' or 'E-chips' to test
24. Record a data point by using the mouse to click the 'Record Once' button
25. Adjust the power level of the chips with the 'Power Level' control
26. Use the mouse to press the 'Vicor Update' button to apply changes
27. Record data points by either manually pressing the 'Record Once' or use the timer and the 'Record in __ Second Intervals' button to automatically record data points. Intervals should not be less than 20 seconds
28. After a data point has been recorded as shown by the reset of the timer, the blinking of the 'Data recorded' light or a beep (if enabled) set a new power level and update the power level by clicking the 'Vicor Update' button.
29. Continue until an Over-temperature state is reached
30. Click the Reset button with the mouse to clear it and reset the vicors to continue testing

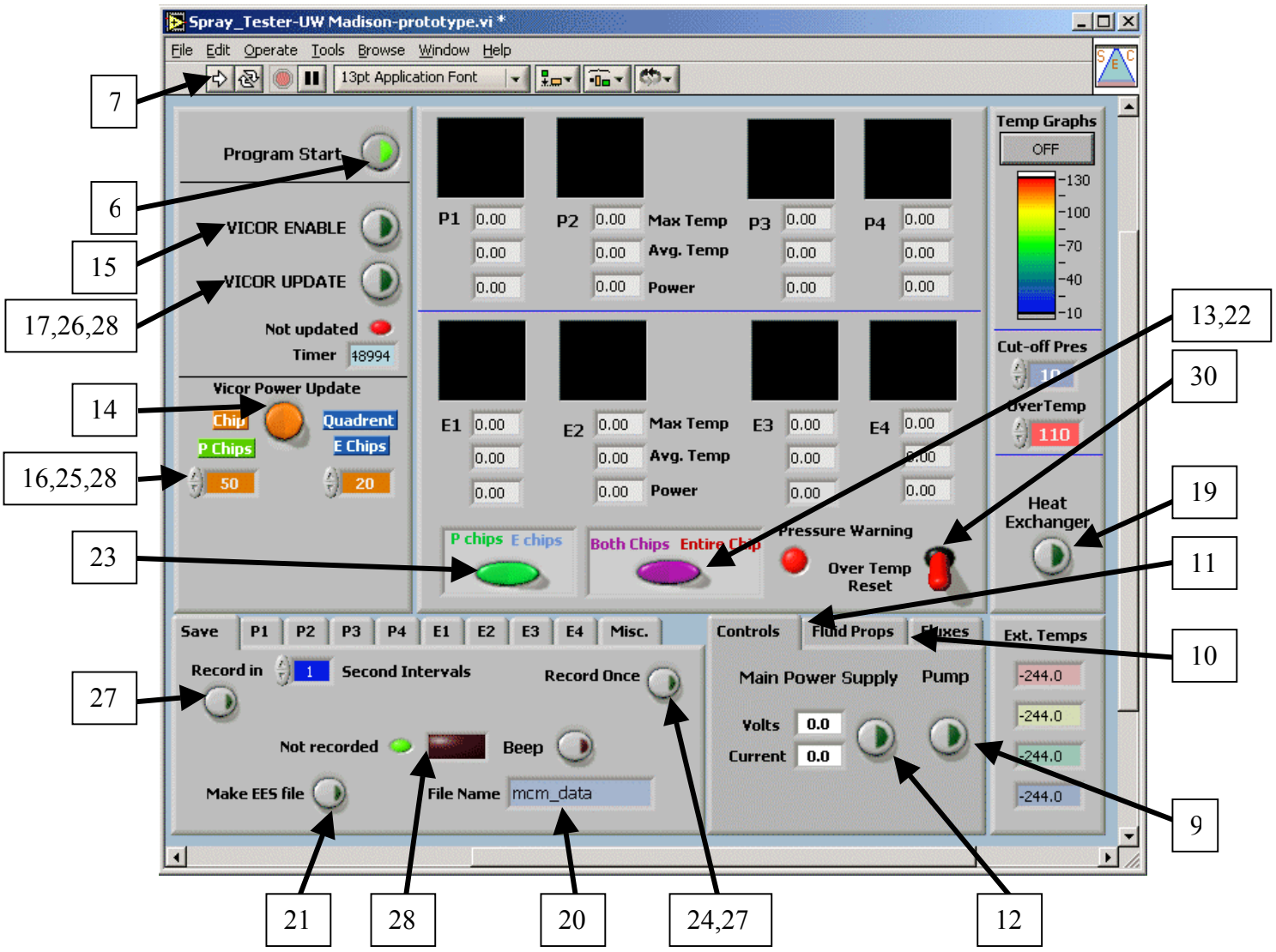
Spray_Tester-UW Madison-prototype.vi *
File Edit Operate Tools Browse Window Help
13pt Application Font
Program Start
VICOR ENABLE
VICOR UPDATE
Not updated
Timer 48994
Vicor Power Update
Chip
Quadrent
P Chips
E Chips
50
20
P1 P2 P3 P4
Max Temp
Avg. Temp
Power
E1 E2 E3 E4
P chips E chips
Both Chips Entire Chip
Pressure Warning
Over Temp Reset
Temp Graphs
OFF
Cut-off Pres
OverTemp
110
Heat Exchanger
Save P1 P2 P3 P4 E1 E2 E3 E4 Misc.
Record in 1 Second Intervals
Record Once
Not recorded
Beep
Make EES file
File Name mcm_data
Controls Fluid Props Fluxes
Main Power Supply
Pump
Volts 0.0
Current 0.0
Ext. Temps
-244.0
7
6
15
17,26,28
14
16,25,28
23
27
21
28
20
24,27
12
9
10
11
19
30
13,22